

**Study of opto-electrical properties of excitonic  
heterostructures and measurement of spatio-  
temporal coherence using a single  
interferometer**

A thesis

Submitted in partial fulfillment of the requirements

Of the degree of

**Doctor of Philosophy**

By

**Mohit Kumar Singh**

**20142029**



**INDIAN INSTITUTE OF SCIENCE EDUCATION AND RESEARCH PUNE, INDIA**

2022

Dedicated to my family

# CERTIFICATE

Certified that the work incorporated in this thesis entitled **Study of opto-electrical properties of excitonic heterostructures and measurement of spatio-temporal coherence using a single interferometer** submitted by **Mohit Kumar Singh** was carried out by the candidate, under my supervision. The work presented here or any part of it has not been included in any other thesis submitted previously for the award of any degree or diploma from any other University or institution.

Date: 26/04/2022



**Dr. Shouvik Datta**

Supervisor

# DECLARATION

I declare that this written submission represents my ideas in my own words and where others' ideas have been included, I have adequately cited and referenced the original sources. I also declare that I have adhered to all principles of academic honesty and integrity and have not misrepresented or fabricated or falsified any idea/ data/ fact/ source in my submission. I understand that violation of the above will be cause for disciplinary action by the Institute and can also evoke penal action from the sources which have thus not been properly cited or from whom proper permission has not been taken when needed.



**Date: 26-04-2022**

**Mohit Kumar Singh**

**Roll No. 20142029**

# Acknowledgement

In the words of the great physicist Isaac Newton, we can only see further by standing on the shoulders of giants. In completion of this thesis, I am grateful for the contributions of many giants, and to their stature, I will always be small.

First and foremost, I would like to thank my PhD supervisor Dr. Shouvik Datta for his continuous guidance and support throughout this long arduous journey. I especially thank him for providing me with an encouraging and independent environment for research where I learned that attitude of ‘solving a problem’ is more important than the problem itself. And, I realized the meaning of his belief that perseverance and a consistent scientific approach do reach a conclusion. I am grateful for his valuable scientific input during my PhD work.

I thank my review committee members, Dr. Sunil Nair and Dr. Shivprasad Patil, IISER-Pune for their timely evaluation of my work and for providing me with helpful suggestions. I express my gratitude to the former and present director IISER Pune, Prof. Ganesh and Prof. Udgaonkar, respectively for providing advanced research labs. I am thankful to former chairs, department of Physics, Prof. Mukhi and Prof. Santhanam, and present chair, department of physics, Prof. Souradeep for funding my local instrumental purchase, meetings and conferences, which helped me a lot and gave me good exposure and opportunities. I am thankful to Prof. Henini, University of Nottingham, United Kingdom for providing me with good quality quantum dot samples which I have used in my research. I would like to thank Dr. Ashish Arora for sharing his invaluable knowledge of optics with me.

I thank my present and past lab members, Dr. Amit, Dipti, Anweshi, Dr. Gautam, Saurabh, Mayur, Deepak, Sumit, Arindam, Debesh and Yuvraj for keeping my spirit high through this journey. Special thanks to Dr. Amit who shared his valuable experimental and theoretical knowledge with me. I thank the technical team of Department of Physics, IISER Pune for their timely assistance during any technical difficulty in the lab. I thank Nilesh, Santosh, Anil and Prashant for helping me and teaching me technical skills. I am grateful to the housekeeping staff of h-cross, Kishore, Rohit and Prashant for helping me and keeping the lab clean.

I wish to thank my seniors, colleagues and friends in IISER who made this journey happening. I would like to thank, Dr. Jitendra, Dr. Rakesh, Dr. Rohit for their valuable advice.

I am grateful to my friends Satish, Rishabh, Dheeraj, Manu, Dr. Sachin, Abraham, Dr. Deepak, Shubham, Mayur with whom I have spent a wonderful time in IISER. I am thankful to all the members of IISER cricket group with whom I have enjoyed a lot. A special thanks to my friend Borish who left a forever void in our hearts.

I would like to express my gratitude towards my family and friends. With their unconditional support, my parents always encouraged me to make my own way and face new challenges. It would not be possible to summarize my brother's contribution in words here. His absolute faith in me has kept me energized and inspired me throughout my academic life. I am grateful to my cousin sisters and brothers for their encouragement.

**April 2022**

**Mohit Kumar Singh**

# Content

Abstract	10
List of symbols and fundamental constant	13
<b>1. Introduction</b>	<b>14-30</b>
1.1 Motivation	14
1.2 Semiconductor Basics	15
1.2.1 Band structure: Direct and Indirect bandgap semiconductors	16
1.2.2 Recombination process: Radiative and non-radiative	19
I Non-radiative Auger recombination	20
1.2.3 Excitons	21
1.2.4 Heterostructure: Quantum well, quantum dots, 2D electron/hole gas	22
I Types of Band alignments at the interface of a heterostructure	23
II Quantum well	24
III Triangular Quantum well	25
IV Quantum wire/rods	26
V Quantum dots	26
VI Formation of spatially indirect excitons in heterostructure	27
1.3 Why is it important to study light emission of semiconductors?	28
1.4 Conclusion and thesis outline	29
<b>2. Basics of optical coherence and its role in light emitting materials and devices</b>	<b>31-47</b>
2.1 Introduction	31
2.2 Motivation to study optical coherence	32
2.3 Observation of optical coherence and how it manifests in terms of interference	33
2.3.1 Temporal coherence	35
2.3.2 Spatial coherence	38
2.4 Methods of measurement	39
2.4.1 Temporal coherence measurement	39
I Mach-Zehnder interferometer	40
II Michelson interferometer	41
III Fringe pattern	41

2.4.2	Spatial coherence measurement	43
	I    Visibility	45
2.5	Role of coherence in light emitting devices	46
2.6	Conclusion	47
<b>3.</b>	<b>Investigation of the effect of interface potential barrier and Auger recombination over the Electroluminescence and its temporal coherence in <math>\text{In}_{0.5}\text{Ga}_{0.5}\text{As}/\text{GaAs}/\text{Al}_{0.3}\text{Ga}_{0.7}\text{As}</math> Quantum dot-Quantum well p-i-n heterostructure</b>	<b>48-69</b>
3.1	Introduction	48
3.2	Experimental details	49
	3.2.1    Sample Details	49
	3.2.2    Experimental setup and methods	51
3.3	Experimental Results of sample A	53
	3.3.1    Bias dependence of electroluminescence at 8.8 K under low current regime (< 2.2 mA)	53
	3.3.2    Temperature dependence of electroluminescence at constant bias	61
	3.3.3    Temporal Coherence of QD and QW-WL emission at higher bias (1 mA – 16 mA) and various temperatures	65
3.4	Experimental Results of sample B	67
3.5	Conclusion	68
<b>4.</b>	<b>Dual measurement of temporal as well as spatial coherence of light using a single experimental setup</b>	<b>70-91</b>
4.1	Introduction	70
4.2	Experimental setup	71
	4.2.1    LabVIEW controlled CCD Camera	73
	4.2.2    Beam blocker	74
	4.2.3    Piezo driver	74
4.3	Data acquisition	77
4.4	Data Analysis Method	79
4.5	Temporal coherence measurement	81
4.6	Spatial coherence measurement	85



4.7	Conclusion	90
<b>5.</b>	<b>Experimental Evidence of Macroscopically Large Quantum Coherent State of Bose-Einstein Condensate of Indirect Excitons</b>	<b>92-107</b>
5.1	Introduction	92
5.2	Experimental details	94
5.2.1	Sample Details	94
5.2.2	Experimental setup and methods	95
5.3	Background research and earlier results	97
5.4	Temperature dependent measurement of Photocapacitance and Photoconductance	97
5.5	Experimental evidence of BEC	100
5.5.1	Interference of two macroscopic groups of excitons	101
5.5.2	Rabi Oscillation of excitonic BEC state	104
5.6	Conclusion	106
<b>6.</b>	<b>Summary and Future direction</b>	<b>108-113</b>
6.1	Summary and Conclusion	108
6.2	Future direction	111
	<b>References</b>	<b>114-129</b>

# Abstract

This thesis presents opto-electrical studies of III-V based quantum heterostructures to understand the underlying many-body physics of excitons or electron-hole pairs. With the progress of advanced fabrication techniques over the years, high quality samples with cleaner interfaces are realized. That provides greater control over the dynamics of these excitons and offers an opportunity to explore the fundamental physics and utilize these for various applications. Experimental investigations of quantum correlations of optical and electrical properties of these excitons can also be intriguing. In this thesis, we also developed a modified optical interferometer that can measure such quantum correlations of excitons through optical emissions.

First, we probed an III-V quantum dot (QD)-quantum well (QW) heterostructure based light emitting p-i-n diode using electroluminescence measurements under a wide range of carrier injections and at different temperatures. The initial lower current bias at  $\sim 8$  Kelvin shows luminescence originates only from the QW even in the presence of QDs having lower energy levels. However, above some threshold levels of carrier injections, light emissions from QDs start. Further increase in current contributes to the exponential increase in QD emission while QW emission remains saturated. This behaviour points toward a potential barrier between QW and QD, which, we argue, can form by diffusion of the electrons from the conduction band of QW to the conduction band of QDs due to their energy difference. With the help of the study of electroluminescence vs bias current and voltage, we approximated an empirical formula that quantified the role of this barrier in QD emission. Furthermore, we separately analysed the emission from QD and QW for temporal coherence with respect to bias current and temperature. The observed decline in optical coherence of QDs with increasing bias is attributed to the non-radiative Auger recombination process, while the same reason explains the unanticipated increase of optical coherence with increasing temperatures. This study shows the importance of optical coherence measurements not only from the point of view of basic physics but also from the perspective of how these measurements can help one to achieve the desired level in applications involving light emitting devices.

Realising the usefulness of optical coherence measurement in condensed matter physics of light emission, we developed a modified Michelson interferometer to measure first order spatial and temporal coherence in a single setup as our second project. We modified the

standard Michelson interferometer to design a compact setup on a single platform. In this project, we tackled some of the fundamental issues of optical coherence measurement using a single optical setup which can have multiple usages. Time delays in optical coherence measurement are often provided by two independent instruments making fine and coarse delays. With our ‘curve overlap’ technique, we are able to combine the results of two instruments while keeping the fine precision over to the range coarse measurements. The instrumental issues of mixing of optical coherence, which was usually overlooked in dual coherence measurements, are worked out with our ‘temporal filtering’ method, where the temporal delay is filtered out during spatial coherence results. Moreover, this setup can be placed outside at room temperature to measure spatio-temporal optical coherence of samples placed inside a cryostat.

Third, we proceeded with the study of a 0D-2D system where InAs QDs are physically separated by AlAs layer from GaAs triangular quantum well (TQW). QDs are fairly uniformly spread over the investigated area of  $\sim 200 \mu\text{m}^2$ . Under the reverse bias, holes present within these QDs form spatially indirect excitons with electrons of the TQW when photoexcited with light having photon energies  $>$  GaAs bandgap. This system of millions of dipolar indirect excitons responded coherently to applied bias and showed collective oscillations of average electrical polarization of these excitonic dipoles measured using photocapacitance. The oscillations are related with coherent resonant tunneling (CRT) of electron between TQW to QD. Moreover, the energy matching condition required for resonant CRT restricts the momentum distribution of electrons for direct photoexcitation of indirect excitons. This results in narrow range of momentum of electrons participating in resonant CRT. As a result, these momentum selective electrons of TQW, in parallel with resonant CRT drive these excitons to spontaneously orientate their dipoles along the direction of applied bias. This coherent collective behaviour of millions of excitons is possible if such a phase coherent macroscopic quantum states of excitons are already present due to excitonic Bose-Einstein Condensation (BEC). In this thesis, we further investigated the behaviour of excitonic condensation under varying photoexcitation intensity and we notice collective oscillations of excitonic polarization like Rabi oscillation of a two level quantum system. We eliminated the possibility of laser coherence influencing the coherent behaviour of excitons by repeating the same experiments with two independent lasers and also with a completely incoherent white light. These experiments showed polarization interference which suggest the presence of spatially correlated coherent state of excitons. We investigated the sample at different temperatures and

observed such quantum coherent behaviour below 100 Kelvin. All these experimental evidences repeatedly indicate the presence of Bose-Einstein condensate formed by these millions of 0D-2D indirect excitons.

In conclusion, we studied fundamental properties of direct bandgap, quantum heterostructures with opto-electronic techniques to understand the many-body physics of excitons and further improve the targeted applications using optical coherence measurements. We surveyed the basics of optical coherence measurements and offered a new instrumentation as well.

## List of symbols and fundamental constant

Symbol	Name	Value
$\mathcal{F}$	Fourier transform operator	
$\lambda$	Wavelength	
$f$	Focal length	
$c$	Speed of light	$2.9979 \times 10^8 \text{ ms}^{-1}$
$k_b$	Boltzmann constant	$1.3807 \times 10^{-23} \text{ JK}^{-1}$
$h$	Planck's constant	$6.626 \times 10^{-34} \text{ Js}$
$\hbar$	Reduced Planck's constant	$1.0546 \times 10^{-34} \text{ Js}$
$\epsilon_0$	Permittivity of free space	$8.854 \times 10^{-12} \text{ Fm}^{-1}$
$e$	Charge of an electron	$1.6022 \times 10^{-19} \text{ C}$

# Chapter 1

## Introduction

### 1.1 Motivation

Semiconductor based technological solutions are integral part of modern life and these are used in almost every optical and electronic device. The tunable nature of optical and electronic properties has made semiconductors suitable for various applications. From simple light emitting diodes (LED) in flashlights to advanced mobile devices, all are majorly based on semiconducting materials. To realize new applications and improve the existing technology, newer semiconducting materials are being explored regularly. With novel material engineering, growth techniques and device level structural modifications, electronic devices are getting more compact and smaller<sup>1</sup>. Progress of major challenges such as space explorations, nanoscale medical technology, quantum computing and communication, high efficiency electronic and LEDs, high power lasers, solar energy generation using solar cells etc. require deep understanding of semiconductor physics. Quantum phenomena, which were only expected at cryogenic temperatures, are now being observed even at room temperatures in novel semiconducting heterostructures. Therefore, it is important to understand the underlying physics of semiconductors to further improve the required knowledge for future explorations. For example, power efficient and low threshold quantum dot lasers can be improved using the study of underlying excitonic recombination. Recently, even more efficient, low threshold laser like coherent emission is reported in vertical cavity quantum well diodes where the cause of coherent light emission is recombination in a excitonic/polaritonic condensates<sup>2-9</sup>. These polaritons are quantum coupled quasi-particle of excitons and photons formed within an optical cavity. Therefore, probing new devices for better understanding of the physics of light-matter interactions is paramount in the field of condensed matter.

Moreover, many of these semiconducting devices require precise electrical and optical controls for real-life practical applications. In the proposed low dimensional photonic integrated circuits, the device level manipulation is optical as well as electrical. This also highlights the need for optical, electrical as well as opto-electrical studies. For example, in light emitting materials, the conventional method of investigation is the study of optical emission. Sometimes, only optical study is sufficient for conclusive understandings, but in some physical

phenomena like excitonic/polaritonic Bose Einstein condensate (BEC), where optical signature of condensation is somewhat debatable, the electrical or mixed opto-electrical investigations can work as better alternatives to reveal the underlying physics. Therefore, both optical as well as electrical instrumentation(s) are essential for the field of light-matter interaction.

Considering the importance of different types of experimentations, in this thesis, a substantial portion is devoted to optical coherence studies of light emitting III-V heterostructures. We also developed a new technique for measuring temporal and spatial optical coherence of light emitting devices using a single experimental setup. In this chapter, we will discuss some of the fundamentals of semiconductor physics to help the reader to grasp the following chapters. Second chapter is specifically dedicated to the fundamentals of optical coherence and details of its measurement techniques.

## 1.2 Semiconductor Basics

As the name suggests, semiconductors were initially categorized as materials which were between conductors and insulators. This categorization was based on their electrical conductivity where semiconductors has typical conductivity between  $\sim 10^4$  to  $\sim 10^{-6}$  S/m. Materials are also categorized in terms of their highest occupied band in 0 Kelvin approximation as well. If the highest occupied band is completely filled and it is separated by the next empty band with bandgap energy above 0 to  $\sim 3$  eV, then these materials are specified as semiconductors. If the same bandgap is more than 3 eV, materials become an insulator. On the other hand, metals have partially filled highest occupied band, leading to a higher conductivity ( $>10^4$  S/m).

Material	Si	Ge	GaAs	CdSe	InGaAs
Bandgap (eV)	1.12 eV	0.661	1.42	1.73	0.8
Group	IV	IV	III-V	II-VI	III-V

However, after continued research for more than 70 years, the semiconductors are no longer restricted to these simple categorizations and many new materials have been synthesized with diverse range of bandgaps and conductivity. For instance, doping impurity or defects<sup>13</sup> can

change the electrical conductivity, while bandgap energy can be varied by changing the molar fractions in compound semiconductors<sup>14</sup>.

The ‘basic’ semiconducting elements from group IV of periodic table are Silicon (Si) and Germanium (Ge) Tin (Sn) and Lead (Pb). These materials have 4 electrons in the outermost shell (mostly s and p shells), and atoms in these materials covalently bond with 4 other atoms in a diamond lattice structure. There are many compound semiconductors, which are known by the periodic table groups of their constituent atoms such as II-VI and III-V etc. These semiconductors are alloys of different elements at binary, ternary and even quaternary levels with different mole fractions. Details of some of these semiconductors are given table 1.1.

### 1.2.1 Band structure: Direct and Indirect bandgap semiconductors

Atomic energy levels are sharp and distinct when gaseous atoms are spatially far enough to have any significant mutual Coulomb interactions. However, if these atoms are forced into a smaller volume where atoms can interact with each other, these sharp energy lines are perturbed and then split into electronic bands. A representative diagram is shown in Fig. 1.1. The shaded region shows the band of energies in new compact form (solid or liquid) of the material and ‘ $a$ ’ is lattice constant (interatomic distance). At this distance, the separation between the energies of two bands is called ‘Bandgap ( $E_g$ )’. Similarly, all semiconducting material has two distinct bands of energy. The fermi level ( $E_f$ ) usually lies in the mid gap region. In the 0 Kelvin picture, the band below  $E_f$  is completely filled and called valance band, and conduction band is above the  $E_f$  which is completely empty. The complete understanding of such band structure is based on crystalline symmetry which explained by group theory. However, this is beyond the scope of this thesis. Reader may be advised to read reference 15 16 17 for more insight.

The most important thing, however, for understanding the application of material is to understand the dynamics of charge carriers. The wave function of the electron inside a semiconductor can be obtained by solving the Schrodinger equation,

$$\left( \frac{-\hbar^2}{2m} + V(r) \right) \varphi(r) = E\varphi(r) \quad (1.1)$$

where,  $m$  is mass of electron,  $V(r)$  is potential field,  $\varphi(r)$  is wave function of electron and  $E$  is the energy eigenvalue. The electrostatic potential for an electron,  $V(r)$  include the interaction



energy due to atoms and other electrons. Therefore, this potential term is complicated to construct analytically. However, due to periodic arrangement of atoms in crystal, a periodic potential is experienced by electron inside the crystal. Bloch<sup>18</sup> proposed that wave function of electron also has the same periodicity as crystal lattice and wrote a wave function called Bloch function. However, there are many approximations and perturbation methods<sup>19</sup> which solve the above Eq. (1.1) and give workable results. It is approximated that electron responds as a free electron with a particular E-k dispersion depending upon the media.

$$E(k) = \frac{\hbar^2 k^2}{2m^*} \quad (1.2)$$

where  $m^*$  is called effective mass and represented by \* sign in superscript. The above formula represents that electron in periodic crystal is behaving as a free electron but with a different effective mass. This effective mass incorporates the average effect of crystal potentials and, therefore,  $k$  is often called crystal momentum. It is evident that  $E$ - $k$  dispersion relation is required to estimate the dynamics of electron. There are many models with different approximations to estimate  $E$ - $k$  relations inside a crystal - namely tight binding model, pseudopotential method, k.p perturbation theory, density functional theory etc<sup>10</sup>. Two of the estimated E-k dispersion for Silicon and Gallium Arsenide are given in Fig. 1.2.

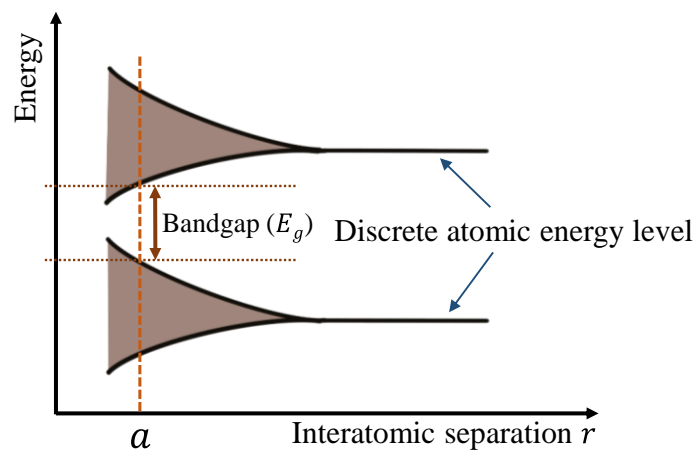


**Fig. 1.1** Splitting of energy levels to form energy bands

Electrical conduction in an intrinsic semiconductor is only possible if thermal generation of electrons from valance band to conduction band is significant. However, electrons can also be excited from valance band to conduction band by many other physical processes. Doping is another such mechanism which also contribute charge carriers from the dopant levels. Moreover, such excitations can also happen optically. The energy of an incident

photon can be absorbed by electron, and it can jump from valance band to conduction band depending upon the selection rules following the Fermi's Golden rule<sup>10,20</sup>. The probability of

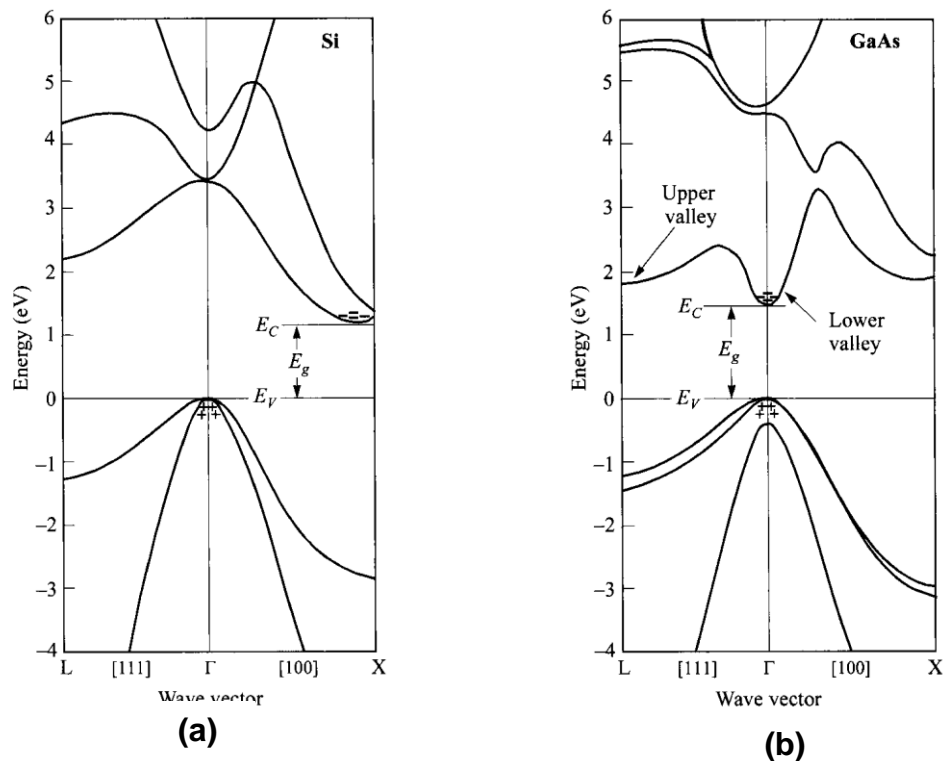


**Fig. 1.2** (a) and (b) are  $E$ - $k$  dispersion relation of Silicon (Si) and Gallium Arsenide (GaAs), respectively. (Figures are copied from reference 16<sup>52</sup>). The conduction band minima and valance band maxima are shifted in wave vector ( $k$ ), in first Brillouin zone of Si. This makes it indirect bandgap material. While, GaAs is direct bandgap material.

such photon absorption depends upon the availability of empty levels and band alignment. If conduction band minima is aligned with valance band maxima, at  $k = 0$ , the semiconductor is called direct bandgap semiconductor, and it has high photon absorption probability due to following reason. The momentum of photon is negligible in comparison with crystal momentum and phonon momentum, therefore  $\Delta k \sim 0$  in a direct optical absorption process. In semiconductor where conduction band minima and valance band maxima lie at different momentum ( $k$ ), the probability of photon absorption is less due to the involvement of phonon to fulfil the momentum conservation criteria. Silicon is an indirect bandgap material and Gallium Arsenide is direct bandgap material as shown through band diagram in Fig. 1.2(a) and (b), respectively. As a result, optical absorption is much higher in GaAs than that in Si. In this

thesis, we select heterostructures of direct bandgap materials from III-V semiconductors to study different opto-electronic properties.

### 1.2.2 Recombination process: Radiative and non-radiative

In the previous paragraph, we discussed materials having direct and indirect bandgaps, and how direct bandgap material allows photon absorption with higher probability than indirect bandgap materials. Reverse to the process of absorption is recombination where excited electron (electron in conduction band) fills the vacancy of valance band (holes), and energy is released either as photon, phonon, or transferred to third particle. If this recombination of

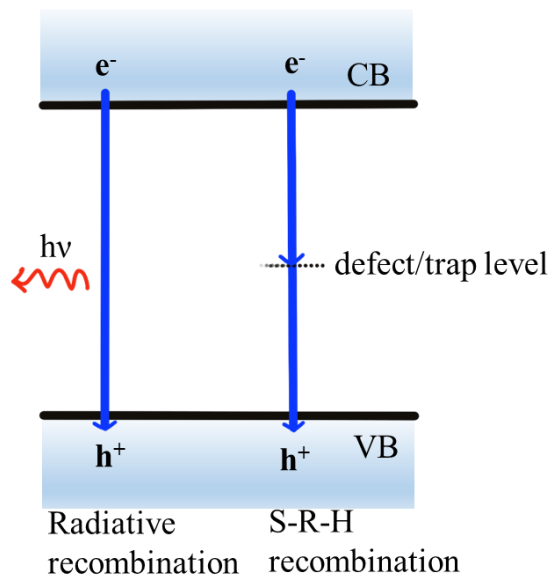


*Fig. 1.3 Transition of electron from conduction band (CB) to valance band (VB) via different recombination processes. (Left) The radiative recombination where a photon of energy  $h\nu (= E_g)$  is released. (Right) A defect assisted SRH non-radiative recombination where energy is released as phonon.*

electron-hole pair results in photon emission, the process is called radiative recombination. This process is at the base of light emitting application in LED and laser diodes. On the other hand, if electron-hole recombination does not result in photon emission, the process is called non-radiative recombination. There are multiple ways for electron to recombine non-radiatively. One such way is defect (trap) assisted non-radiative recombination where defect states inside the forbidden bandgap traps electron or hole and allow them to cross the bandgap without emitting a photon. It is known as Shockley-Read-Hall<sup>21,22</sup> recombination (SRH), and it becomes more prominent at higher temperature where carriers can jump in/out of defects state using the thermal energy. Schematics of radiative and SRH recombination are shown in Fig. 1.3.

## I. Non-radiative Auger recombination

Apart from SRH recombination, the other non-radiative recombination method is Auger recombination. It is a three particle process where one electron-hole pair recombine and energy (instead of emitting a photon) is transferred to the third particle (either to an electron or a hole). The process is termed as *eeh* or *ehh* depending upon the number of electrons and holes participating in Auger process as shown in Fig. 1.4. The Auger rate process is defined as,

$$R_{Auger} = C_{Auger}n^3 \quad (1.3)$$

where  $R_{Auger}$  is rate of Auger recombination and  $C_{Auger}$  is called Auger recombination coefficient and  $n$  is free charge carrier density. Auger recombination rate increases exponentially with increasing temperature and decreasing bandgap (Ref 10, Chapter 9). Being a non-radiative process, it is detrimental for the process of light emission, especially high intensity infrared lasers where it is still a challenge. There are many theoretical models which

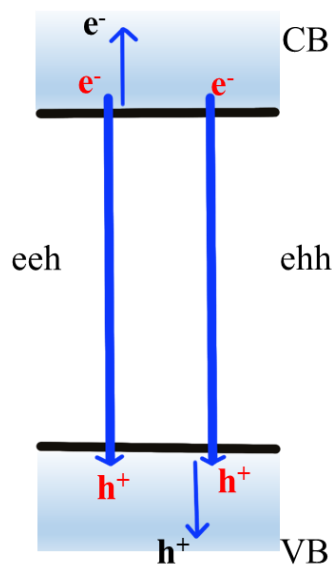


*Fig. 1.4 Two different types of Auger recombinations depending upon the number of charge particles involved in the process. (Left) eeh Auger recombination which involves recombination of one electron-hole pair and energy is given to one electron of conduction band sending it to the higher energy levels in conduction band. (Right) Similarly, ehh recombination where two holes and one electron is involved.*

has been proposed<sup>23–27</sup> to explain the Auger related effects. Some of these categorizations are direct Auger recombination, phonon-assisted indirect Auger recombination, direct/indirect inter-band and intra-band Auger recombination etc. However, there is yet to be a common consensus<sup>25,28</sup> on theoretical ground, and experimental investigations are still ongoing. Apart from emission efficiency, the impact of such Auger processes on coherence properties of emission is worth investigating. In chapter 3, we will see the impact of Auger process on temporal coherence of emission of III-V quantum dot-quantum well system.

As mentioned in the previous topic, electron-hole pair band to band transition results in radiative recombination in a direct bandgap material. However, due to the opposite charge of electron and hole, these two particles can interact through electrostatic Coulomb force and make a bound state. This bound state is called ‘exciton’.

### 1.2.3 Excitons

The electron and holes can mutually interact with each other via Coulomb attraction and make a bound state (negative energy state) like hydrogen atom. This dipolar quasi-particle is called excitons. The simple schematic diagram of exciton is shown in Fig. 1.5(a) where arrows indicate Coulomb attraction. The solution of Schrodinger equation for excitons is similar to hydrogen atom and excitons has fine energy lines<sup>20,29</sup>,

$$E_n = -\mu e^4 / 2(4\pi\epsilon_0)^2 \hbar^2 \epsilon^2 n^2 \quad (1.4)$$

or

$$-R_X / n^2 \quad (1.5)$$

where  $n=1,2,3..$ , and  $e$  is charge of electron,  $\hbar$  is reduced Plank’s constant,  $\epsilon_0$  is permittivity of free space,  $\epsilon$  is dielectric constant of medium,  $\mu$  is reduced mass of exciton,  $R_X$  is excitonic Rydberg constant ( $R_X = \mu R_H / m_e \epsilon^2$ ) and  $E_n$  is binding energy of exciton.  $R_H$  is hydrogen Rydberg constant (13.6 eV) and  $m_e$  is electronic mass. However, the total energy of exciton is given as

$$E_X = E_g - E_n + \frac{\hbar^2 K^2}{2M} \quad (1.6)$$

where  $E_g$  is bandgap,  $\vec{K} = \vec{k}_{electron} + \vec{k}_{hole}$ , and  $M = m_e^* + m_h^*$ . In direct bandgap semiconductors, exciton can be formed with direct photoexcitation ( $h\nu \geq E_g - E_n$ ). However, owing to the negligible momentum of photons, the condition of momentum conservation reads as

$$\vec{K} = \vec{k}_{electron} + \vec{k}_{hole} \sim 0 \quad (1.7)$$

The electron in an exciton can recombine with its hole in valance band to emit photon. Excitonic recombination is preferable when binding energy ( $E_n$ ) is higher than thermal energy

( $k_bT$ ), therefore, in spectral absorption measurement, excitonic transition appear as resonant peak<sup>30</sup>. Depending upon the dielectric medium of a material, the formation of excitons varies in size and binding energies. In inorganic semiconductor, the studied samples in this thesis, the high dielectric constant of medium allows larger ( $\sim$ nm) Wannier-Mott exciton with low binding energies ( $\sim$ meV) due to high screening effects<sup>20</sup>.

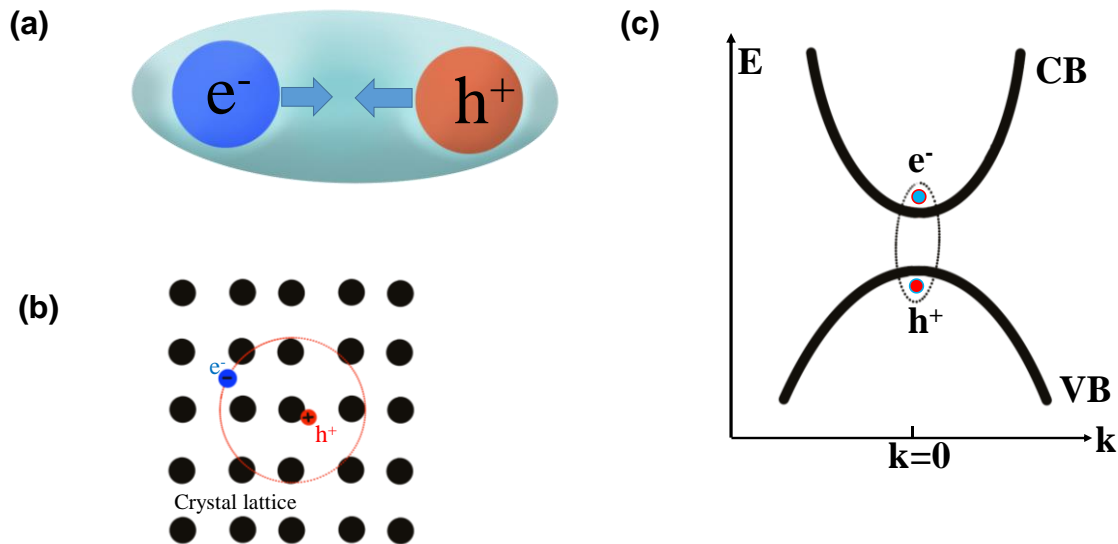


*Fig. 1.5 (a) The simplistic illustration of exciton where positively charge hole is attracted to electron to form a bound pair. (b) Wannier-Mott excitons (c) The  $E$ - $k$  representation of exciton formed in direct bandgap.*

#### 1.2.4 Heterostructure: Quantum well, quantum dots, 2D electron/hole gas

It is seen that alloys of different materials with different molar fractions can be tuned to the desired properties having certain bandgap energies in direct/indirect bandgap. Some electrical properties can also be tuned by changing the doping concentration of impurities and defects. Similarly, a range of physical properties can be achieved by combining different materials into a heterostructure. In simple words, an epitaxial heterostructure is growth of two or more materials of nearly similar lattice constants such that these materials are fabricated as one single crystal. There are many methods to make such heterostructure as chemical vapor deposition (CVD), metal oxide chemical vapor deposition (MOCVD), molecular beam epitaxy (MBE) etc. In these methods, materials are grown layer by layer with accuracy of atomic thickness. With advancement of new technologies, these growth methods are getting more accurate, making the heterostructure more controlled and clean at the interface.

## I. Types of Band alignments at the interface of a heterostructure

There are three types of band alignments (also called band lineup) at the interface of two different semiconductors, and these types are categorized as Type I, Type II and Type III. In Fig. 1.6, we show schematics of band structure of two semiconductors  $A$  and  $B$  with their respective bandgaps  $E_g^A$  and  $E_g^B$  and electron affinity  $\chi_A$  and  $\chi_B$ , respectively that are grown in heterostructure. Here,  $E_g^A > E_g^B$  and schematics of different band alignments are shown. In type I, the conduction band edge of  $B$  is lower than the conduction band edge of  $A$ , and valance

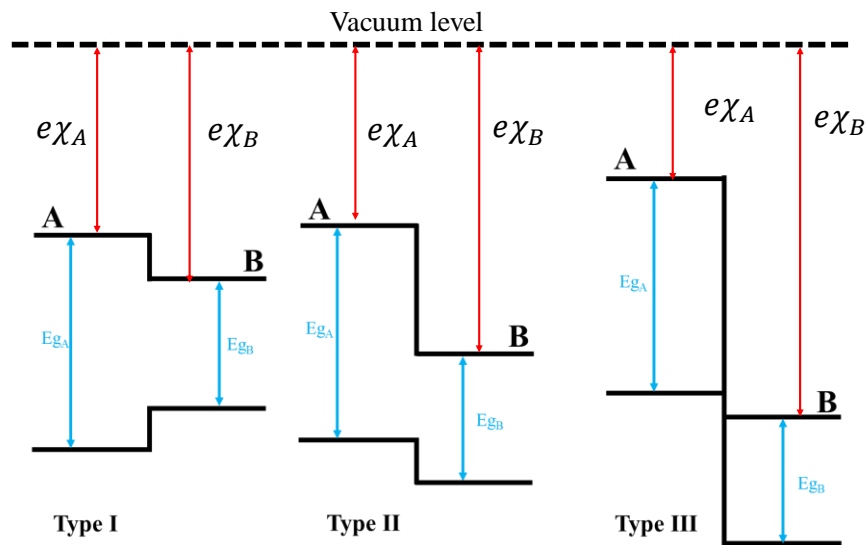


*Fig. 1.6 Different types of band alignments.*

band edge of  $B$  is higher than valance band edge of  $A$ . Type I band alignment can make quantum well (QW) structure and effective in carrier confinement of electrons as well as holes.

In type II, the conduction band edge of  $B$  is lower than conduction band edge of  $A$  but valance band edge of  $A$  is also lower than valance band edge of  $B$ . Here, the minimum energy configuration of electron and hole at the interface are spatially separated which results in low optical transition in this type of heterostructure. In type III, the conduction and valance band edge of  $B$  are lower than conduction as well as valance band edge of  $A$ .

Among these, type I has significant optoelectronic applications since its band edges are in the same spatial region and are not restricted to interface as in the case of type II. These band alignments are used in quantum heterostructures and will be discussed in the next sections. In this alignment, carrier dynamics is greatly decided by the energy differences of band edges,

particularly when thermal energy is of the order of these energies. These energy differences are called band offset and shown as double sided orange arrows in Fig. 1.7 and marked as  $\Delta E_c$  and  $\Delta E_v$  for conduction and valance band, respectively. In this thesis, we will discuss the devices with type I alignment only.

The major benefit of fabricating a quantum heterostructure is to have control over the spatial dimensions of a material where quantum phenomena can be detected (possibly even up to room temperature like excitons). We discuss the characteristics of some of these quantum structures in the following paragraphs.

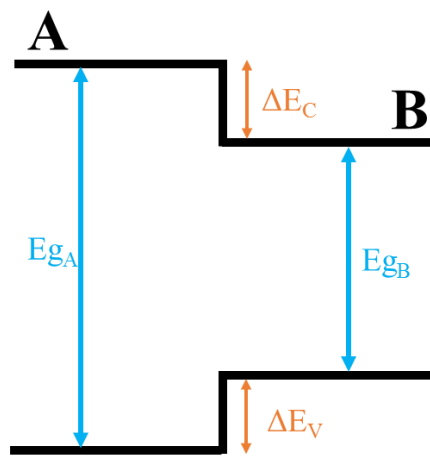


*Fig. 1.7 Band offset energies of conduction and valance band,  $\Delta E_c$  and  $\Delta E_v$ , respectively.*

## II. Quantum well

When a layer of lower bandgap material is grown between materials of higher bandgap, the resulting potential configuration is formed into quantum well. In Fig 1.8(a), the schematic of heterostructure layers and band diagram is shown. Here, the thickness of central layer should be in the order of De Broglie wavelength (of electron/hole) such that distinct quantum energy levels are created (shown as  $E_n$ ). The electron/holes have two dimensional (2D) freedom of movement in  $x$ - $y$  direction. These layers can be grown repetitively to have multi-quantum well or a super lattice configuration used in some of the devices. The lateral confinement of electron/hole raises the probability of Coulomb interaction and formation of direct excitons. These excitons in QW has two dimensional freedom of movement.



### III. Triangular Quantum well (TQW)

As shown in Fig. 1.8(b), triangular quantum well has a gradient potential formed on the one side while a sharp potential barrier on the other. This gradient potential is achieved by

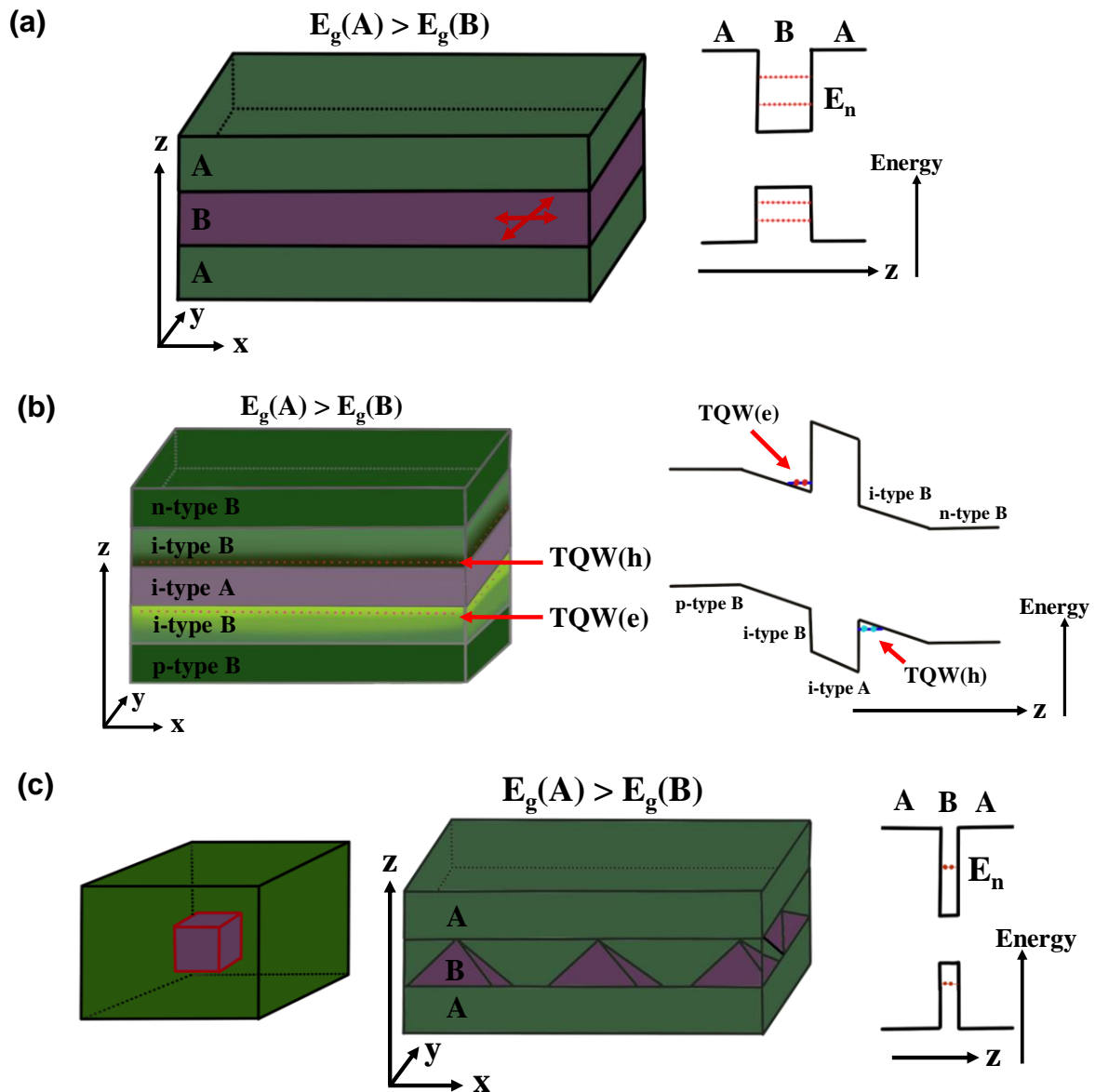


**Fig. 1.8** (a) Schematics of quantum well configuration where material B with lower bandgap is grown between two layers of material A with higher bandgap.  $z$  is growth direction. Two cross arrows in B layer shows the two dimensional degree of freedom of charge particle in the layer (left). Corresponding energy diagram is shown at the right where simple “particle in a finite box” potential profile is seen.  $E_n$  is energy levels of quantum well. (b) Similar representation and band diagram for TQW and (c) QD.

sandwiching a barrier layer between two intrinsic semiconductors. These intrinsic layers is either supplied with external bias voltage or grown between p and n-doped materials to provide the required bending of bands. In TQW, electrons (or holes) are accumulated in energy levels forming a layer of electron (or holes) in  $x$ - $y$  dimension. These layers are called two dimensional electron gas (2DEG) and two dimensional hole gas 2DHG, respectively.

#### IV. Quantum wire/rods

If one dimensional crystal is grown whose thickness is of the range De Broglie wavelength, the resulting configuration is called quantum wire/rod. Here carriers has one dimensional degree of movement.

#### V. Quantum dots

If a low bandgap material is grown in such a manner that it is embedded from all sides within a higher bandgap material, the resulting configuration is called quantum dot provided the spatial dimensions are within the order of De Broglie wavelength of electron/hole. The carrier inside has zero spatial degree of movement and therefore, QD are called zero dimensional (0D). Due to strong spatial confinement, the probability of excitons formation is even higher than QWs. The schematic diagram of heterostructure layers and band structure are shown in Fig. 1.8(c). The samples studied in this thesis are heterostructures with self-assembled QDs.

Due to different degrees of movement and spatial confinements, the energy levels and their densities are different in different configurations. The density of states of these heterostructures, ( $g(E) = dN/dE$ ) are given in Fig. 1.9.

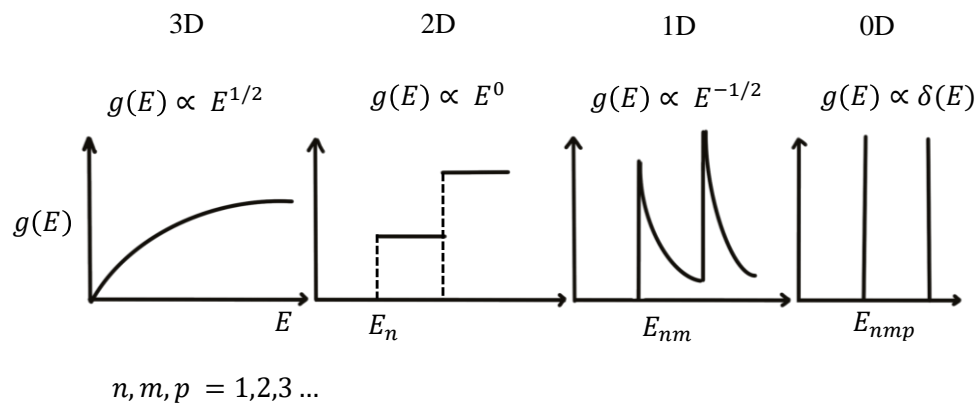


**Fig. 1.9** Density of states for quantum structures of different dimension.

In this thesis, we will discuss the study of two heterostructure configuration. QD grown inside QW to make a step-like band structure for additional carrier confinement in chapter 3. And, in chapter 5, QD grown inside a barrier layer where QD and TQW are separated by barrier layer.

## VI. Formation of spatially indirect excitons in a heterostructure

Interlayer excitons can also be formed by electrons and holes which are physically separated by a higher bandgap layer. The presence of barrier prevents electron-holes from recombining thus increasing the lifetime of excitons to microseconds. The carriers eventually

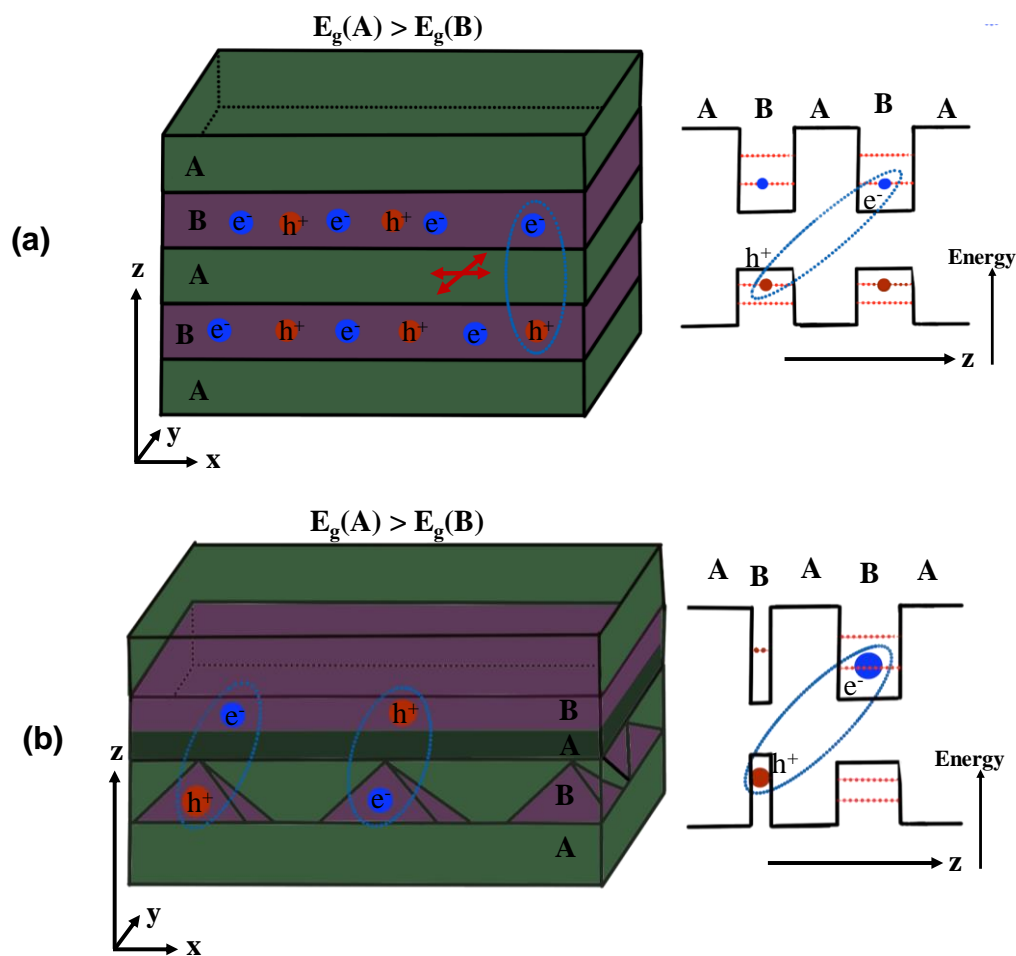


**Fig. 1.10** (a) 2D-2D indirect exciton formed in double QW configuration. (b) 0D-2D indirect excitons in QD-QW system.

tunnel through the barriers to recombine. An elaborated study is done in our group by Amit *et al.*<sup>31,32</sup> on GaAs/AlAs/GaAs heterostructure where applied bias pushed electron and holes

towards the barrier layer which increases the probability of formation of indirect excitons. In Fig. 1.10(a), an indirect exciton is shown between two QW B-layers separated by a barrier A-layer. Such 2D-2D indirect excitons can have two dimensional movement i.e.  $\vec{K}_x, \vec{K}_y \neq 0, \vec{K}_z \cong 0$  (shown as crossed arrows in Fig. 1.10(a) in x-y plane). The other type of indirect excitons shown in Fig. 1.10(b) has one QD B-layer and other QW B-layer separated by barrier A-layers. These 0D-2D indirect excitons are anchored to one QDs and  $\vec{K}_x, \vec{K}_y, \vec{K}_z \cong 0$ . These excitons are formed in 0D-2D configuration and will be discussed in chapter 5.

### 1.3 Why is it important to study light emission of semiconductors?

It is obvious that we need visible light sources in our day to day life. With the current climate crisis and global warming, we are in desperate need of power efficient, durable and safe devices. Efficient photovoltaic materials are expected to harvest solar energy and reduce the harmful effect of fossil fuels. The direct bandgap semiconducting materials are proving the solution for such problems. For the common lighting of streets and households, the LED based bulbs are more safe and energy efficient than conventional incandescent light sources or gas based compact fluorescent light (CFL). Semiconducting LEDs turns out to be better option for display devices and digital communication. These LEDs are actively being used in medical application, indoor farming and even green house agriculture etc<sup>33</sup>. Similarly, Laser diodes are used in holography, communication, medical applications, positioning systems, motion sensors, heavy industrial cutting etc. Despite the current achievements, there is still a need to find better alternatives. With advanced growth techniques, new type materials and heterostructures are being grown which can utilize the quantum effect for these common application. Excitonic laser<sup>34-37</sup> and polariton laser<sup>38-43</sup> (even at room temperature) are one such example. Lasing in polaritonic condensate<sup>44</sup> system is achieved by stimulated scattering of polaritons, and such systems also form quantum vortex<sup>2,9</sup> which are purely quantum mechanical effects. These systems are yet to be understood and emission from such system can be used in future exotic technology. We know that optical communication is the fastest method of data transfer and fiber optics are backbone of modern World Wide Web. Apart from the high intensity application, the photon level emission is being considered for quantum computation. A single photon with its polarization<sup>45</sup> state is being treated as a qubit<sup>46</sup>. Photonic integrated circuits are being built for such quantum processing<sup>47,48</sup> and communication<sup>29</sup>. All these application need an efficient and versatile light source with required properties

(quantum/classical) and this essentially requires the rigorous study of new light emitting material/devices. For example, transient spectroscopy of emission from LED to study different carrier recombination mechanics like excitonic, bi-excitonic, trionic or Auger recombination<sup>49-51</sup> etc., coherence study to verify excitonic/polaritonic condensate state, spectra study for different transition energies in a system.

## 1.4 Conclusion and thesis outline

In this chapter, we have provided some of the basic concepts of semiconductors which are going to help the reader to understand the following chapters. For detailed descriptions of these concepts, the reader is advised to go through additional references 10, 19, 20 and 52. In the second chapter, the basics of optical coherence will be discussed theoretically as well as experimentally. We explain the motivation to study optical coherence and its role in the light emitting materials and devices. The standard techniques of coherence measurement are discussed for their possible advantage(s) and disadvantage(s).

In the third chapter, we will describe the electroluminescence of a quantum dot-quantum well heterostructure and find the role of the interface potential barrier formed due to charge carrier diffusions between two layers of different bandgaps. At low carrier injections, this potential barrier prevents the carriers from entering the energetically lower QDs. As a result, only QWs with higher energy levels emit light which thereby affects the device performance. Beyond a certain threshold level of injection current, the carrier starts to jump into QDs and emission from QDs begins. This total emission from QDs and QWs are analyzed separately with respect to applied bias to build an empirical relation between emission of QDs and the role of the potential barrier. Temperature dependent study reveals the activation energies required for carrier recombination in QD and QWs. The temporal coherence of spectrally separated light emissions from QD and QW are investigated with respect to bias and temperature. This coherence study reveals that at higher carrier injections, Auger recombination reduces the optical coherence of QD emission, while coherence increases with increasing temperature. These results are explained with the effective carrier density in respective layers of QD and QW.

In chapter four, we show the detailed instrumentation of modified optical coherence measurement technique where spatial coherence can also be measured along with temporal

coherence in a single experimental setup. The use of two retroreflectors and their lateral and longitudinal movement helps to provide necessary spatial and temporal shift in Michelson interferometer design. The use of piezo is to provide not only fine temporal shift but also filter the temporal coherence from spatial coherence. This optical assembly can be kept at room temperature outside a cryostat (where sample is attached) for optical coherence study providing a major advantage over double slit based spatial coherence measurement system.

In the fifth chapter, a III-V QD-TQW heterostructure based p-i-n diode is studied to understand the opto-electrical response of photo generated excitons. A layer of InAs QDs is sandwiched between two AlAs/GaAs barrier layers forming a QD-TQW configuration. Due to photoexcitation from p-side, under reverse bias, the higher electron density in TQW results in formation of 0D-2D indirect excitons. The capacitance measurement across the diode shows the phase coherent oscillatory behavior of effective electrical polarization due to these indirect excitonic dipoles in reverse bias as well as in forward bias. However, the study in this chapter is mostly described for reverse bias. The temperature dependent study shows a spontaneous enhancement of effective polarization and appearance of oscillation below  $\sim 100$  K. The bias driven indirect excitons undergo Bose Einstein condensation at a particular resonant condition governed by the coherent resonant tunneling between QD and TQW. The condition of coherent resonant tunneling and direct photo excitation of excitons results in momentum narrowing required for Bose Einstein condensation (BEC). The capacitive interference of two optically generated BEC shows large in plane spatial correlation which will have practical implication in quantum computation.

Finally, in chapter six, we conclude the work of this thesis and discuss the future aspect of this work.

## Chapter 2

# Basics of optical coherence and its role in light emitting materials and devices

### 2.1 Introduction

In the previous chapter, we discussed about the fundamentals of light emitting semiconductors and their basic properties. Here, we elaborate optical coherence and its measurement techniques in detail as require to grasp the following chapters. Coherence is commonly used term in scientific as well as in general literatures. It usually means something closely related to a certain systematic order, rhythm, coordination and consistency. This word has a Latin origin where *co-* means ‘together’ and *haerere* means ‘to stick’ translating the word as ‘sticking together’. Obviously, by definition, two systems are required which are supposed to “stick together” or between which the ‘coherence’ is to be observed. These systems could be independent or related or the same system at different times depending upon the type of observation. In terms of physics, ‘sticking together’ means a system is maintaining its consistency in any of its parameters with respect to the known variables i.e. the parameter can be predicted at other values of variable if it is known for one value of variable. For instance, the phase of a perfectly monochromatic light can be predicted accurately at any time, if its time of origin is known. This is a theoretical example of perfectly coherent systems. However, perfectly monochromatic light do not exist due to quantum uncertainty principle (natural broadening). Also, gaseous emitters suffers from Doppler broadening and pressure broadening<sup>53</sup> while non-radiative transition provide additional broadening in solid emitters which does not allow any system to emit a perfectly monochromatic light. On the other hand, in a non-monochromatic light, the phase randomly varies after some distance and time and this distance/time is known as coherence length/time. It is not possible to predict the phase accurately after light travels a distance much more than its coherence length or after a duration much more than its coherence time. However, phase is predicted with some degree of accuracy within the coherence length/time and this degree of accuracy is essentially the quantification of optical coherence of light. The property of light to maintain its phase in time or space are

called temporal or spatial coherence, respectively. The same analysis of phase is applied to matter waves<sup>54–56</sup>.

## 2.2 Motivation to study optical coherence

Researchers has been trying to utilize the quantum properties of quantum (quasi) particles as it can offer a huge range of applications in the fields of material characterization, simulation, information processing, computing, communication etc. In semiconductor devices, the quantum phase of particle is lost due to interaction with statistically large number of particles which renders these systems unusable for quantum application. Under very sophisticated isolation conditions, response of single particle can be observed but these technologies is far from the realization of chip-based quantum devices. For instance, some people are trying with photons at individual level, successfully utilizing the quantum nature of photon for the quantum processing. However, these experiments require highly sophisticated preparation and detection protocols for identifying these single quantum state. The single photons sources use in these experiments are tested with temporal correlation function making coherence measurement as a crucial part of experiment.

In new low dimensional quantum sized heterostructures, a macroscopic phase coherent Bose Einstein Condensate (BEC) state of bosonic quasi-particle like excitons, polariton and even photon (in high quality dye filled cavity) has been achieved. These condensates in their quantum ground state can be envisioned as a single quantum state consisting of many-particles making it suitable for the above mentioned quantum application. There are many experimental and theoretical studies over these states, however, a thorough understanding of these states is required for successful utilization in given quantum applications. Most of the coherence study in these samples are for verification purpose only and we can get a greater insight by studying the optical coherence in detail. For instance, enhanced spatio-temporal coherence is one of the signatures of these quantum coherent states. Recently, quantum vortex is noticed in the spatial coherence measurements.

Apart from these quantum application, we can find interesting physics by investigating the role of coherence in different physical phenomena in light emitting semiconductors. From the research point of view, the rigorous study of optical coherence is still lacking in newly developed low dimensional materials, quantum heterostructures, meta materials<sup>57–63</sup>.



## 2.3 Observation of optical coherence and how it manifests in terms of interference

In section 2.1, we discussed the concept of coherence on the accuracy of phase prediction of light. Now we will discuss the process of experimental observation and quantification of optical coherence. Can we predict the phase of light? The optical frequency is about  $\sim 10^{15}$  Hz, and usual photodetectors are not fast enough to detect the phase variation in the time domain. However, light as an electromagnetic (EM) wave has the ability to interfere. In fact, the idea of coherence is hard to explain without invoking the idea of interference. Interference is a physical process where amplitudes of the two interfering waves undergo superposition which is governed by the amplitude's vector addition. Interference of phase related waves results in sustained pattern of interference. By investigating the interference, the phase information and coherence can be extracted. In this chapter, all analyses are done by assuming that the light is travelling in vacuum/space and simple EM wave follow vacuum dispersion relation between frequency and wavenumber,  $\omega = c|k|$ . EM wave is assumed to be linearly polarized and further treatment is done by taking EM wave as scalar wave following Helmholtz equation. In Fig. 2.1(a), we show the schematics of a sinusoidal optical wave of amplitude  $E_1$  that incidents upon the detection plane  $A$  and its intensity is  $I_1 = |E_1|^2$ . If same sinusoidal wave, either delayed in time or displaced spatially ( $E_2$ ) overlaps and superpose with  $E_1$  and their combined effect is being observed at  $A$  as shown in Fig. 2.1(b). What should be the total intensity at  $A$ ? If  $I_{total} \neq I_1 + I_2$ , then there exists a phase relation between two waves. To explain this, we consider monochromatic waves and take example of temporal coherence where the same light is inspected for phase coherence after a time delay ( $\Delta\tau$ ).

Consider a monochromatic electric fields,  $E_1(t) = E_0 e^{-i\omega_1 t}$  and same field after time  $\Delta\tau$  as  $E_2(t + \Delta\tau) = E_0 e^{-i\omega_1(t+\Delta\tau)}$ . Here  $\omega_1$  is frequency of wave and  $E_0$  is constant amplitude. If the amplitudes of these two optical fields are added/superimposed, then the resulting field will be  $E_1 + E_2$  and total intensity will be,

$$I_{total} = \langle (E_1 + E_2)^2 \rangle = \langle (E_1 + E_2)(E_1 + E_2)^* \rangle \quad (2.1)$$

here  $\langle \rangle$  are time average taken over the time  $\gg$  the oscillation period of wave

$$I_{total} = \langle E_1 E_1^* \rangle + \langle E_2 E_2^* \rangle + \langle E_1 E_2^* \rangle + \langle E_2 E_1^* \rangle \quad (2.2)$$

here  $\langle E_1 E_2^* \rangle$  is  $\frac{\lim}{T \rightarrow \infty} \int_T^0 E_1 E_2^* dt$ , last two terms are complex conjugate, and first two terms are intensities,

$$I_{total} = |E_0|^2 + |E_0|^2 + 2 \times Real\langle E_1 E_2^* \rangle \quad (2.3)$$

here  $|E_0|^2 = I_0$ , intensity of individual wave and

$$I_{total} = I_0 + I_0 + 2 \times Real\langle E_1 E_2^* \rangle \quad (2.4)$$

First two terms are simple addition of intensity while third term decides if  $I_{total} \neq I_1 + I_2$

$$Real\langle E_1 E_2^* \rangle = |E_0|^2 Real\langle e^{-i(\omega_1 \Delta \tau)} \rangle \quad (2.5)$$

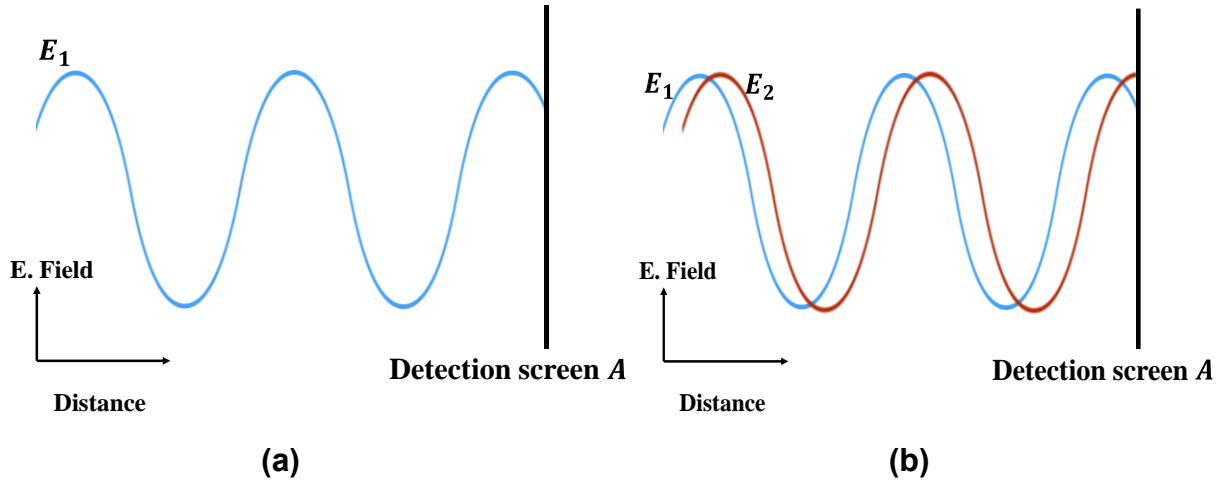


**Fig. 2.1** (a) One sinusoidal optical field wave falling on detection plane A. (b) Two phase shifted sinusoidal wave falling on detection plane A. Blue and red color are used for distinction of two waves and colors do not represent wavelength.

Since the term in angular bracket is independent of time ( $t$ ), the third term becomes,  $I_0 \cos(\omega_1 \Delta \tau)$ . This oscillatory third term produces the fringe pattern observed in interferometric experiments.

In case of two waves of different frequencies  $\omega_1 \neq \omega_2$  and  $\omega_1 - \omega_2 = \Delta \omega$

$$Real\langle e^{-i(\omega_1 - \omega_2)t} e^{-i\omega_2 \tau} \rangle = Real\{e^{-i\omega_2 \tau} \langle e^{-i\Delta \omega t} \rangle\} \rightarrow 0 \quad (2.6)$$

here quantity under the angular bracket is time dependent and its time average tends to zero. This suggest that  $I_{total} = I_1 + I_2$  and fields of different frequencies do not interfere. However,

some reports claim interference of two frequencies<sup>64,65</sup> by observing the beats which has the frequency at least two to four orders of magnitude lower than optical frequencies<sup>66,67</sup>.

Nevertheless, after getting the observational idea about coherence, we categorize the optical coherence as temporal and spatial coherence.

### 2.3.1 Temporal coherence

Temporal coherence is the measure of correlation of an optical field with itself after a given time. A simplistic schematic diagram of a wave is provided in Fig 2.2 where two instant of times ( $t_1$  and  $t_2$ ) are marked on a propagating wave. Temporal coherence is defined as,

$$g^{(1)}(t_1, t_2) = \frac{\langle E(t_1)E^*(t_2) \rangle}{\sqrt{\langle |E(t_1)|^2 \rangle \langle |E(t_2)|^2 \rangle}} \quad (2.7)$$

Some authors also write  $g^{(1)}(t_1, t_2)$  as  $\gamma(t_1, t_2)$  and call it with different names such as first order correlation function<sup>53</sup>, normalized correlation function<sup>68</sup> or complex degree of

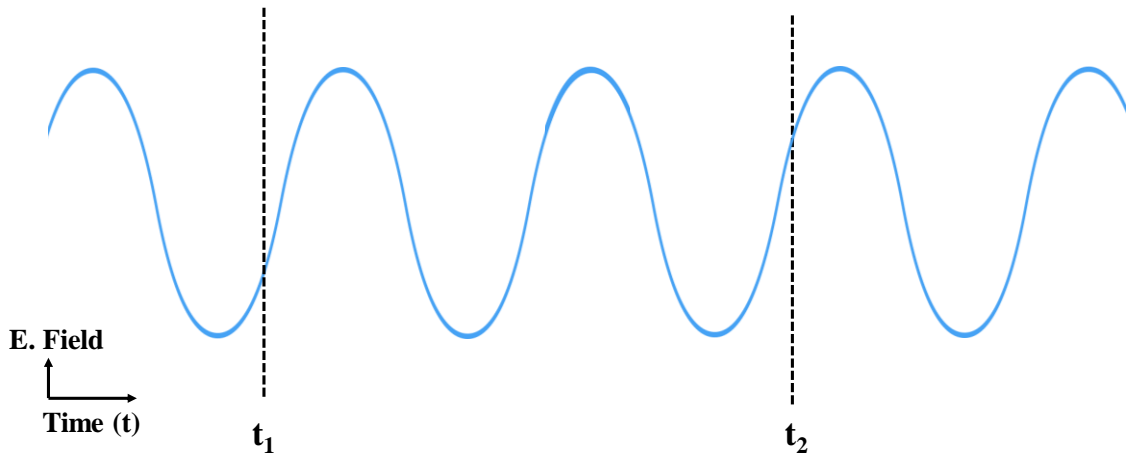


**Fig. 2.2** Schematics of a simplistic monochromatic wave where two instant of times are marked. The correlation of the same wave between these two times is called temporal correlation.

coherence<sup>69</sup>. Therefore, reader should be carefully while going through different references. The information of temporal coherence is estimated by measuring the modulus of the  $g^{(1)}(t_1, t_2)$  function which exist for  $0 \leq |g^{(1)}(t_1, t_2)| \leq 1$ . If  $|g^{(1)}(t_1, t_2)| = 0$ , the light is completely incoherent between the given two instant of times  $t_1$  and  $t_2$ . Thermal white light sources show the completely incoherent nature after the time separations of approximately

~100 fs. For  $|g^{(1)}(t_1, t_2)| = 1$ , light is perfectly coherent, however, such sources does not exist in nature. The single mode lasers are highly coherent and  $|g^{(1)}(t_1, t_2)| \rightarrow 1$ . In case of light correlating with itself at exactly the same time,  $E(t_2) = E(t_1)$ , the magnitude of correlation function  $|g^{(1)}(t_1, t_2)|$  is always 1. The values of  $|g^{(1)}(t_1, t_2)|$  between 0 and 1 indicates partial coherence. These three states of coherence are summarized in table 2.1. Time  $t_2$  can also be written as  $t_1 + \Delta\tau$  where  $\Delta\tau = t_2 - t_1$  and  $g^{(1)}(t_1, t_2)$  can be function of  $\Delta\tau$  only if the process is stationary.

It is easy to see how  $g^{(1)}(\Delta\tau)$  is related to the process of interference. In Eq. (2.3), if third term is multiplied and divided by  $\sqrt{\langle |E(t)|^2 \rangle \langle |E(t + \Delta\tau)|^2 \rangle}$ , the resulting equation is

$$I_{total} = |E_1|^2 + |E_2|^2 + 2\text{Real}\{g^{(1)}(\Delta\tau)\sqrt{\langle |E(t)|^2 \rangle \langle |E(t + \Delta\tau)|^2 \rangle}\} \quad (2.8)$$

Or

$$I_{int} = I_1 + I_2 + 2|g^{(1)}(\Delta\tau)|\sqrt{I_1 I_2}\cos(\theta) \quad (2.9)$$

here  $I_{total}$  is replace with  $I_{int}$ . And,  $\theta$  is phase difference between  $E(t)$  and  $E(t + \Delta\tau)$ . First, let us revisit the case of perfectly monochromatic wave, where third term  $I\cos(\omega_1\Delta\tau)$ , if

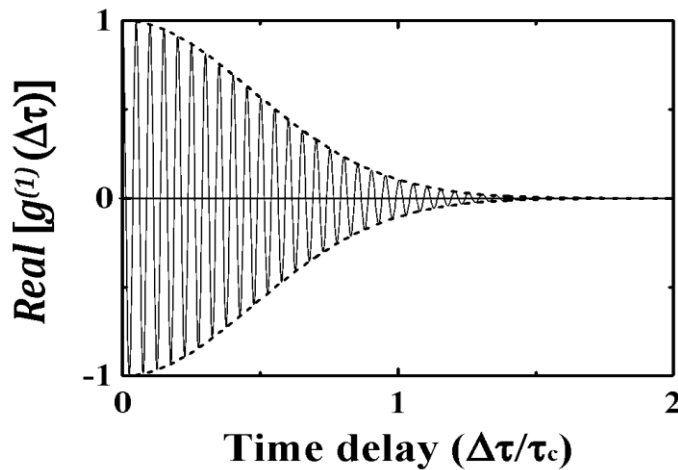


*Fig. 2.3 Typical variation of Real  $|g^{(1)}(\Delta\tau)|$  with respect to time*

compared with eq. (2.9), shows  $|g^{(1)}(\Delta\tau)| = 1$  for any  $\Delta\tau$ . Therefore, a monochromatic light is perfectly coherent and any deviation from monochromatic nature will result in reduction in coherence. For partially coherent light,  $|g^{(1)}(\Delta\tau)| < 1$  and it eventually goes to zero with

increasing  $\Delta\tau$ . The typical variation of  $|g^{(1)}(\Delta\tau)|$  with time delay is shown in Fig. 2.3. The  $\Delta\tau$  after which  $|g^{(1)}(\Delta\tau)|$  reduces significantly, is called coherence time ( $\tau_c$ ).

There are several ways to understand the concept of temporal coherence. As discussed in reference 53, the non-monochromatic field can be defined as a monochromatic field with a time dependent phase term  $\phi(t)$  such that  $E(t) = E_0 e^{-i(\omega t)} e^{i\phi(t)}$ . When this field is correlated with itself after a time delay  $\Delta\tau$ , the  $g^{(1)}(t, t + \Delta\tau)$  is

$$g^{(1)}(t, t + \Delta\tau) = e^{-i\omega\Delta\tau} \langle e^{i\phi(t+\Delta\tau)} - e^{i\phi(t)} \rangle \quad (2.10)$$

For  $\Delta\tau \ll \tau_c$ ,  $\phi(t + \Delta\tau) \sim \phi(t)$  and  $\langle e^{i\phi(t+\Delta\tau)} - e^{i\phi(t)} \rangle \rightarrow 1$ , which shows the upper limit of coherence as  $|g^{(1)}(t, t + \Delta\tau)| \rightarrow 1$ . For  $\Delta\tau \gg \tau_c$ , the  $\phi(t + \Delta\tau)$  is randomly varied and  $\langle e^{i\phi(t+\Delta\tau)} - e^{i\phi(t)} \rangle \rightarrow 0$ , which shows the lower limit of coherence. And, for  $\Delta\tau$  between these two limiting conditions,  $0 < \langle e^{i\phi(t+\Delta\tau)} - e^{i\phi(t)} \rangle < 1$  show the partial coherence.

<b>Table 2.1</b> First order correlation function values and their corresponding state of coherence	
$ g^{(1)}(t, t + \Delta\tau) $	<i>State of coherence</i>
$\rightarrow 1$	Highly coherent
0	Incoherent
Between 0 and 1	Partially coherent

To estimate the value of  $|g^{(1)}(\Delta\tau)|$ , the correct estimate of  $\theta$  is required. This is not possible to keep track of phase over a large distance ( $\gg \lambda$  of source) or know the origin time of source due to limitation of detection technique. Therefore, this problem is circumvented by using the cosine function itself i.e. cosine pattern is known to oscillate between -1 and +1. A phase difference of at least  $\pi$  is provided between  $E(t_1)$  and  $E(t_2)$  to track the cosine function. However, experimentally it take at least  $4\pi-6\pi$  to correctly estimate cosine function. Once the cosine function is known, it can be put in Eq. 2.9 with detected values of  $I_1$ ,  $I_2$  and  $I_{int}$  to estimate the value of  $|g^{(1)}(\Delta\tau)|$ .

Other way to understand the temporal coherence is through Wiener-Khintchin<sup>69</sup> theorem where temporal correlation function is related to power spectrum of source by the Fourier transform relation.

$$F\{g^{(1)}(\Delta\tau)\} = I(\omega) \quad (2.11)$$

Here  $I(\omega)$  is power spectrum. To have a physical idea, if we imagine  $I(\omega)$  to be Gaussian then its Fourier transform will also be Gaussian and their curve widths are inversely related. It shows more number of frequencies in source leads to smaller coherence length. Therefore, white light sources has smaller coherence length compared to single colour.

### 2.3.2 Spatial coherence

Spatial coherence is introduced as correlation of emitted light between two spatially separated points at the same time ( $\Delta\tau = 0$ ) from a source. Simplistic schematic is provided in

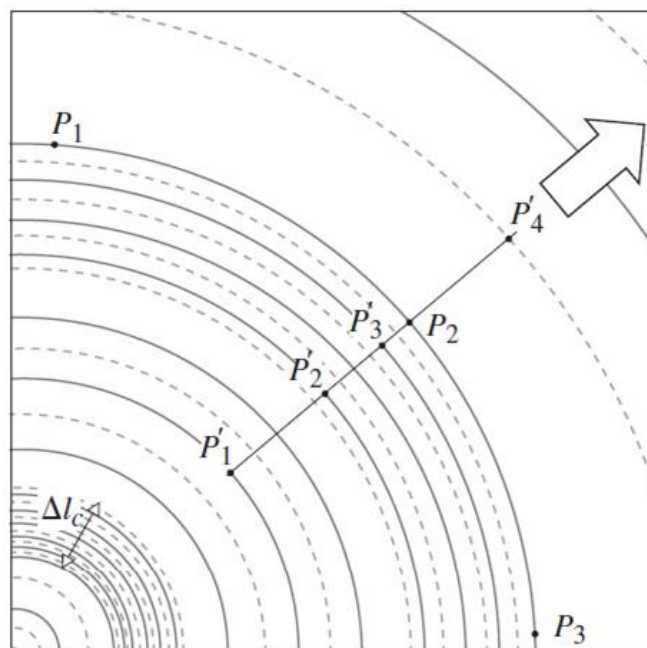


**Fig. 2.4** A quasi monochromatic point source at the bottom left corner emits light of unperturbed circular (spherical in 3D) wave front. The dashed and solid lines are maxima and minima of light wave. The point  $P_1$ ,  $P_2$  and  $P_3$  are at the same maxima of wave indicating a constant phase. Image is copied from reference 69.

reference 69 where light emitted from quasi-monochromatic point source has an unperturbed wave front at all equal distance from source. If time of origin of light is  $t = 0$  then equidistant circumference (shown as dashed and solid lines in Fig. 2.4) indicate the wave front where phase is constant.

However, practical light sources are not point sources but cluster of point sources. These individual point source may or may not be in correlated to each other. The uncorrelated

sources are referred as incoherent sources. When such source emits light and it propagates in medium, by principle of Huygens (see the lake pebble example in reference 69 ), the constant phase (as in case of point source) becomes superposition of many such wave fronts and resultant light get incoherent due to contributions from many uncorrelated points sources. As a result, spatial coherence is decreased.

The quantification of spatial coherence is defined as first order spatial correlation function,

$$g^{(1)}(P_1, P_2) = \frac{\langle E(P_1)E^*(P_2) \rangle}{\sqrt{\langle |E(P_1)|^2 \rangle \langle |E(P_2)|^2 \rangle}} \quad (2.12)$$

$E(P_1)$  and  $E(P_2)$  are optical fields at point  $P_1$  and  $P_2$ , respectively.  $\langle |E(P_1)|^2 \rangle$  and  $\langle |E(P_2)|^2 \rangle$  is their corresponding intensities. Eq. (2.12) can be rewritten as,

$$g^{(1)}(P_1, P_2) = \frac{\langle E(P_1)E^*(P_2) \rangle}{\sqrt{I(P_1)I(P_2)}} \quad (2.13)$$

This function is also measured similar to temporal correlation function, by the process of interference

$$I_{Int}(P_1, P_2) = I(P_1) + I(P_2) + 2|g^{(1)}(P_1, P_2)|\sqrt{I(P_1)I(P_2)} \cos(\theta) \quad (2.14)$$

here  $\theta$  is phase different between  $E(P_1)$  and  $E(P_2)$ , at the field at point  $P_1$  and  $P_2$ . To know the value of  $|g^{(1)}(P_1, P_2)|$ , the value of  $I_{Int}(P_1, P_2)$ ,  $I(P_1)$ ,  $I(P_2)$  and  $\cos(\theta)$  are to be known.

## 2.4 Methods of measurement

Here we discuss the conventional methods of temporal as well as spatial coherence measurement. Michelson and Mach-Zehnder interferometer is used for temporal coherence measurement while Young's double slit method is used for spatial coherence measurement. There are other alternatives/modification which are used for technical convenience or improvements which will be discussed in chapter 4.

### 2.4.1 Temporal coherence measurement

Temporal coherence measurement needs the same light to interfere with its delayed version. Therefore, two replica of the same light are required while one of these is delayed in time. There are two instrument majorly used for these measurement.

## I. Mach-Zehnder interferometer

Schematics of Mach-Zehnder is given in Fig. 2.5. The source beam falls on beam splitter  $BS_1$  where two beam replica are created which goes through path I and II. Using multiple mirrors (shown as M), the beams are guided to meet at  $BS_2$  where these two beam interfere. A simple mirror assembly shown inside blue box is to produce path different between

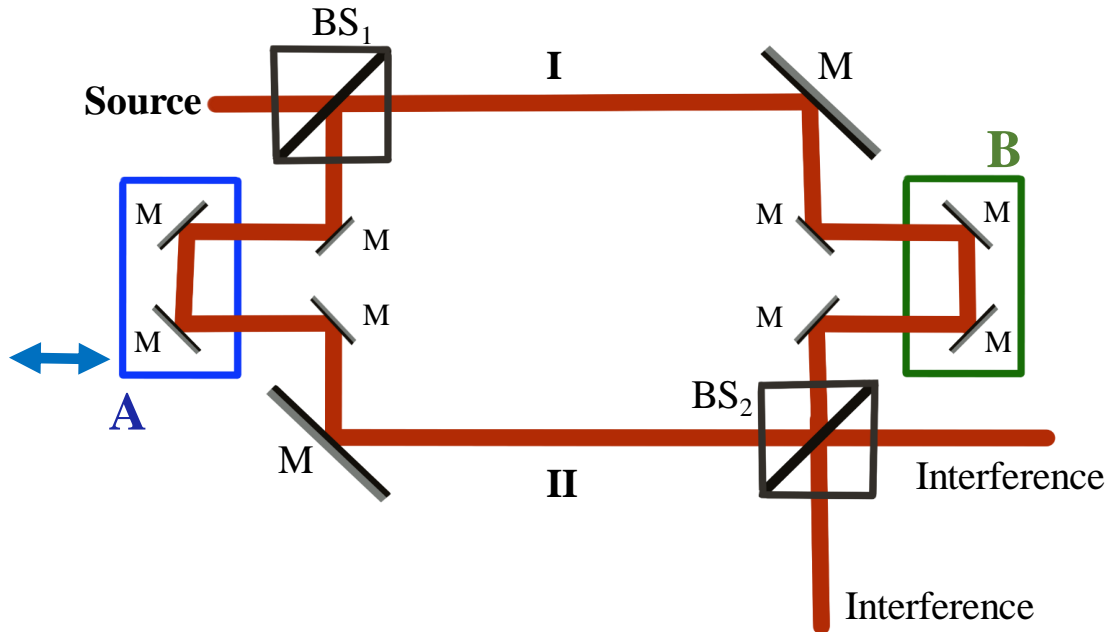


**Fig. 2.5** Schematic diagram of Mach-Zehnder interferometer.  $BS$  is 50:50 beam splitter and all  $M$  are mirrors. I and II are two paths created by  $BS_1$  and these two beam meet at  $BS_2$  for interference. Blue and green mirror assembly is to produce delay in one of the beams. The double sided arrow of 'assembly A' shows the method to delay one of the beams by adding extra path to beam II.

the two travelling path I and II. If this assembly is moved in the direction shown by double sided arrow, the I and II will have different travelling time and controlled time delay can be provided as  $\Delta L = c\Delta\tau$ . Here,  $\Delta L$  is path difference between I and II and  $\Delta\tau$  is corresponding time delay. Assembly A and B are used as instrument to provide coarse and fine delay  $\Delta\tau$ . Finally, the interference pattern is analysed to estimate  $|g^{(1)}(\Delta\tau)|$ .

This interferometer is mostly used when there is requirement of reference beam<sup>70-72</sup>. One of the path (between I and II) is kept as reference beam and some transparent sample is placed in the other path. The change in the interference or intensity correlation is then used for analysis.



## II. Michelson interferometer

Schematics of Michelson interferometers are given in Fig. 2.6. This interferometer uses less number of mirrors and beam splitter compare to Mach-Zehnder interferometer. In Fig.

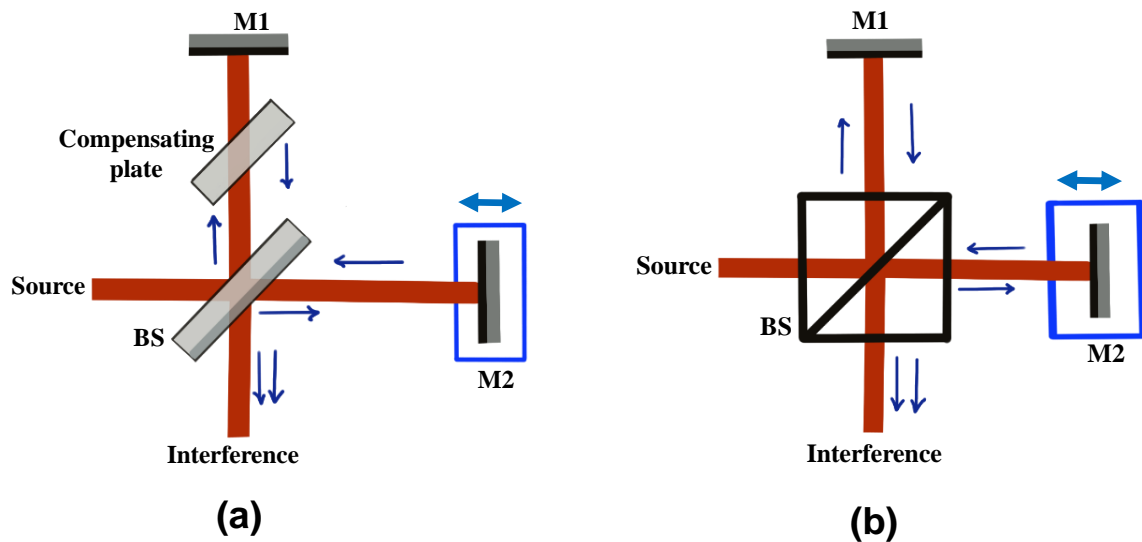


**Fig. 2.6** (a) Michelson interferometer with slab BS. A compensating slab of same refractive index as BS is placed in one arm. Mirror M2 can be moved to produce time delay. (b) same interferometer with cube BS.

2.6(a), the interferometer uses plate beam splitter where one of the surface is partially reflecting. Due to uneven number of beam travel through BS between two beams, a compensating plate of same refractive index is used. However, such BS suffer from beam shift, ghost reflection, hence cube BS is a better alternative. Such interferometer is shown in Fig. 2.6(b). The mirror M2 is able to produce temporal delay between two beams by moving in the direction shown by double sided arrow.

## III. Interference Fringe pattern

Fringe pattern in any optical interference is a two dimensional contour of phase difference between 0 and  $2\pi$  of two interfering optical fields. Phase is the function of space and time and, therefore, it can be manipulated by controlling the field temporally or spatially. One such manipulation is done by utilizing the refractive index ( $>1$ ) of a medium that introduce a

phase due to change in fields optical path<sup>73</sup>. The locus of equal phase points is a wave front and phase difference of two interfering two wave fronts makes the fringe pattern. With the help of Michelson interferometer, in Fig. 2.7, we produced fringe pattern with two different curvature

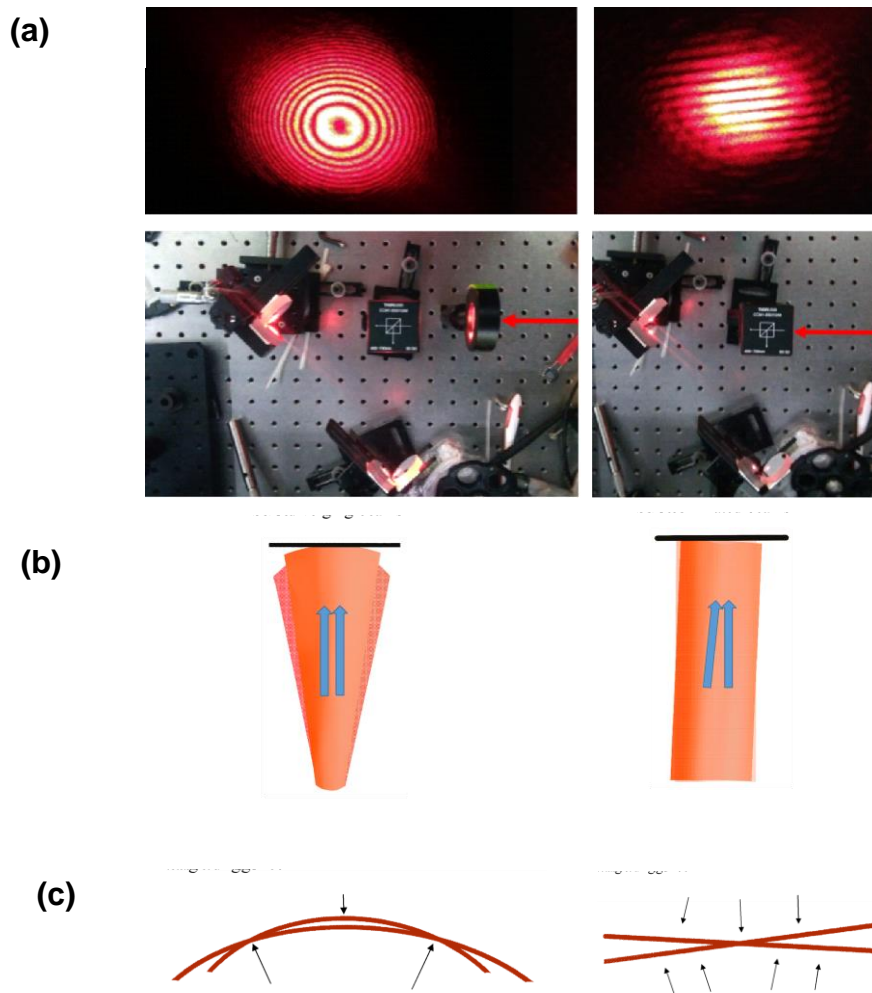


**Fig. 2.7** Two different types of fringe patterns due to curvature in the wave fronts of interfering beams (a) two types of experimental setups where one setup has diverging beam falling on BS (left) and collimated beam falling on BS (right). (b) Schematics of beams falling on screen. The diverging beam has curvature (left) and collimated beam has flat wave front (right). (c) Schematics of wave front of either case.

of wave fronts. In first case, the He-Ne gas laser (633 nm) is passed through concave lens ( $f = 50$  mm) and it creates spherical wave fronts going through the beam splitter. The reflections from mirrors of two arms are projected on screen for interference. In case of no temporal delay ( $\Delta\tau = 0$ ), two wave front superimpose perfectly leading to overall maxima. However, due to

difference in length of propagation, the two wave fronts have different curvature on the screen. The intersection of equal phase are circular due to spherical curvature of wave front and circular fringes are observed. The beam propagation and curvature intersections are shown in the left of Fig. 2.7 (b) and (c). In second case, the already collimated beam from laser is allowed to go through beam splitter. The beams showed the linear fringes due to slight inclination shown in Fig. 2.7(b) (right). This inclination or curvature difference between two wave fronts results in phase mismatch and where condition of interfering intensity is decided by equation of interference (Eq. (2.9)). In Fig. 2.7(c), the wave front intersections are shown for the second case. The fringe curvature analysis is used in finding the non-uniformity of reflecting surface. This is the basic idea behind Optical Coherence Tomography<sup>74-76</sup>. The relative phase between two fields are very sensitive towards any length variation in instruments. For an instrument of arm length of ~cm, the wavelength to arm length ratio is  $\sim 10^{-4}$ . The fringe motion is utilized in noticing small movements and wavelength measurement.

## 2.4.2 Spatial coherence measurement

In Case of spatial coherence, two points in the cross-section of (transverse direction) emitting light beam are selected for interference. The separation between those points is  $\Delta r$ . In Fig. 2.8(a), the schematics of Young's double slit interferometer is given where slits are separated by  $\Delta r$ . Fig. 2.8(b) shows the interference pattern formed at screen and its fringe profile. The light intensity coming from individual slit produces its own diffraction pattern which overlaps to make interference pattern. The equation of interference

$$I_{int} = I_1 + I_2 + 2|g(\Delta r)|\sqrt{I_1 I_2} \cos(k \cdot x - \varphi) \quad (2.15)$$

where  $k = \vec{k}_1 - \vec{k}_2$  and  $\vec{k}_1$  and  $\vec{k}_2$  are wave vector of interfering field and  $\varphi$  is constant phase factor and  $x$  is linear coordinate on screen. To extract the  $|g^{(1)}(\Delta r)|$  from interference pattern  $I_{int}$ , the value of  $I_1$  and  $I_2$  are required. These individual intensities are diffraction pattern from individual slit. To estimate the value of  $I_1$  and  $I_2$ , Fraunhofer diffraction conditions are fulfilled by using two convex lens on either side of slits pane. This condition is approximated by Fresnel number  $\frac{d^2}{b\lambda} \ll 1$ . Here  $d$  is distance between slit and screen and  $b$  is width of slit. And,  $I_1$  and  $I_2$  are assumed to be single slit diffraction 'sinc function' and fit in above given interference pattern. The sinc function is the Fraunhofer diffraction pattern of a rectangular slit.

However, the fitting condition of Fraunhofer diffraction demands uniform, coherent

irradiance at the individual slit for diffraction pattern. This usually fulfilled by keeping source at infinity. The detailed descriptions for Fraunhofer diffraction are provided in reference 69

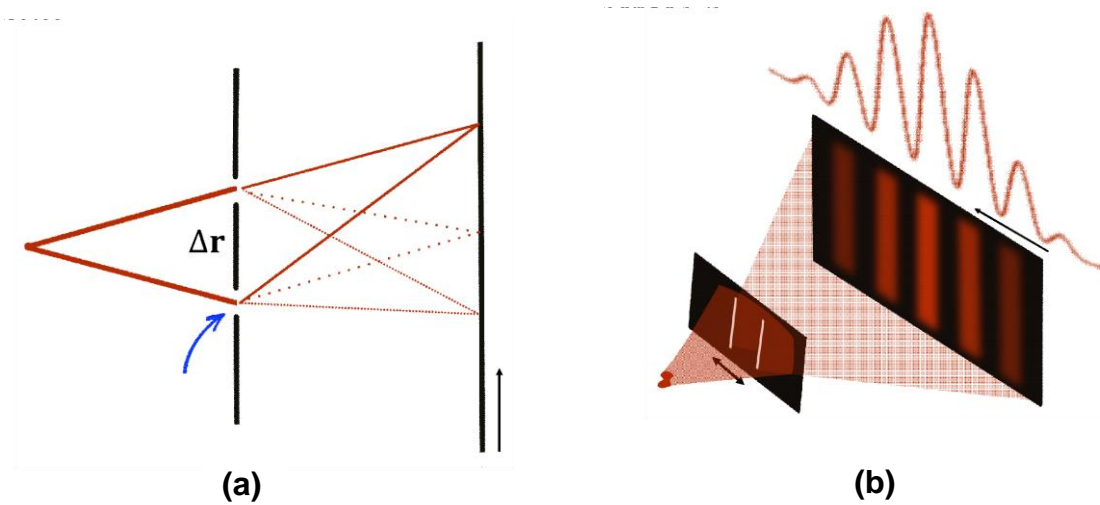


**Fig. 2.8** (a) Schematic of Young's double slit experiment. The investigated source ( $S$ ) is kept in front of two slits which are distance  $\Delta r$  apart. In front of slit, a screen is placed where light coming from slits interfere. (b) The schematics of double slits producing interference at screen.

and <sup>77</sup>. The case of longitudinal spatial coherence which is in the direction propagation of light is considered to be temporal coherence<sup>69</sup>. However, Ryabukho *et al.*<sup>78–82</sup> and Abdulhalim<sup>83–85</sup> has done theoretically and experimentally work claiming the distinction between these two coherences.

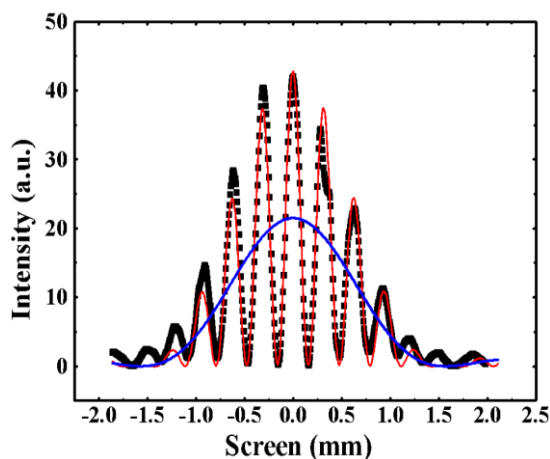


**Fig. 2.9** Interference pattern taken from He-Ne laser with slit width of 0.1mm and slit separation of 1mm. Black dots are data taken by CCD, red line is interference fitting function(Eq. 2.9). The blue line is diffraction from individual slit and in the form of sinc function. This sinc function is taken as intensity of individual slit.

## I. Visibility

An important perspective of understanding coherence is by superposition of many interference fringe. For example, if a point source has broad power spectrum and emits a range of wavelengths. The condition of interference i.e. the location of maxima and minima depends upon the wavelength and two different wavelengths do not interfere. Therefore, slightly shifted wavelengths going through same interferometer will result in slightly shifted maxima(s) and minima(s) and contrast of interference fringe will be reduced. Similarly, many point sources constituting an extended light source leads to superposition of many interference patterns and reduced contrast of interference fringes. The contrast of fringes is related to first order correlation function by visibility as

$$Visibility = \frac{I_{max} - I_{min}}{I_{max} + I_{min}} \quad (2.16)$$

where  $I_{max} = I_1 + I_2 + 2|g|\sqrt{I_1 I_2}$  and  $I_{min} = I_1 + I_2 - 2|g|\sqrt{I_1 I_2}$  are adjacent maximum and minimum intensity in fringe pattern. These maximum and minimum intensities are resulted at the point where  $\cos(k \cdot x - \varphi)$  in Eq. (2.15) are +1 and -1, respectively. If we put respective value of  $I_{max}$  and  $I_{min}$ , the visibility is

$$Visibility = 2|g^{(1)}| \frac{\sqrt{I_1 I_2}}{I_1 + I_2} \quad (2.17)$$

if  $I_1 = I_2$ ,  $Visibility = |g^{(1)}|$ . Here we omitted  $\Delta\tau$  and  $\Delta r$  since formula stands for both type of coherences. We will use  $Visibility$  to calculate the  $|g^{(1)}(\Delta\tau)|$  function in chapter 3 for temporal coherence measurement. However, in chapter 4, we avoided using it to estimate  $|g^{(1)}(\Delta\tau, \Delta r)|$  due to its very strict condition of  $I_1 = I_2$ . This condition is not fulfilled during spatial coherence measurement for sources with non-uniform emission output. Therefore,  $I_1$  and  $I_2$  are measured individually and Eq. (2.15) is used.

Here, we understood that correlation between individual emitter of light at the source affects the correlation of light at the screen. This property is utilized to investigate the correlation of source and to understand the underlying physics of light emission. For example, the BEC of polariton makes a macroscopic state of few micrometers and these remain spatially correlated which is known as ODLRO<sup>86</sup> (off-diagonal long range order) which result in increased spatial coherence on screen. Therefore, spatial correlation measurement is one way to measure this long range order.

## 2.5 Role of coherence in light emitting devices

Every light emitting device is fabricated/manufactured keeping a particular application in mind. The general illumination used for indoor lightening are usually white, less intense and incoherent for better visibility. Display devices constitute Red Blue and Green LEDs which are more coherent. Recently, QDs were used in display devices because of its narrow emission around a particular wavelength resulting in better performance. Further modifications in growth of these quantum structure are being made to improve the efficiency for a desired application. One such device level modification in quantum structures are presented in chapter 3. Holography is one application where temporally coherent light is required<sup>87</sup>. Coherence microscopy/white light interferometry require a source with small coherence length for a better depth resolution. Group velocity and refractive index measuring devices required partially coherent light which has coherence length only of the range of table top instruments. Gravitational wave detection lab used infrared laser with high coherence length which is used in measuring the phase variation due to gravitation wave having precision up to  $\sim 10^{-19}$  m. Super-luminescent diodes are good example of coherence controlled application. To reduce the effect of speckles in image projection devices which uses lasers, super luminescent diodes are used which has low temporal coherence and high spatial coherence. The stellar Michelson interferometer also uses the spatial coherence properties of star light to measure its angular dimension. These are all examples requiring the particular coherence properties.

Above, we gave some of the existing technological devices where optical coherence properties are utilized. However, the major benefit of studying optical coherence study is to investigate quantum optics. Extensive research is going to find appropriate material to use these quantum optical application to room temperature on device level. We briefly gave some of the examples above in section 2.2. Also, studying the coherence during the transition of device from non-lasing to lasing above threshold in low dimensional novel materials can be relevant from research point of view. For instance, excitonic emission is narrow and these materials make excellent active material for lasing. The reports on perovskite lasing<sup>88,89</sup> are mainly focused on emission bandwidth and intensity change. On the other hand, one can study the coherence of perovskite based light emitting materials and devices - before, after and during the transition from non-lasing to lasing. 1D quantum wire lasing uses the single wire<sup>90,91,92</sup> as active medium as well its own optical cavity without the need of any external cavity. Therefore, it will be interesting to study not only single quantum wire but also inter-wire correlations in

quantum wires based light emitting structures. This kind of structures can possibly make temporally coherent but spatially incoherent light sources. Polariton lasers<sup>39,41-43</sup> as low threshold highly coherent light emitting devices, can be potentially used in photonic circuits<sup>93</sup>, optical switching<sup>73</sup>, work as qubit<sup>93</sup> etc.

## 2.6 Conclusion

In this chapter, we discussed the theoretical aspect of coherence and its connection with optical interference. We showed the mathematical relation with interference and the first order correlation function  $g^{(1)}(\Delta\tau, \Delta r)$ . We also elaborated the experimental techniques to measure  $|g^{(1)}(\Delta\tau)|$  and  $|g^{(1)}(\Delta r)|$ . We discussed elaborately in motivation section about why studying optical coherence is timely topic of research. Additionally, we discussed in the role of coherence is light emitting device and some of the possible research areas. In chapter 3, we will analyse the temporal coherence of spectrally separated electroluminescence from quantum dots and quantum well to understand the role of non-radiative Auger recombination on coherence of individual emission. This study not only helps us to sense Auger process in such quantum dots based light emitting systems but also benefits to optimize these devices for application. Also, we require new tools and techniques to rigorously study both type of correlation in these novel-systems. In chapter 4, we are going to discuss a modified Michelson interferometer to measure both type of coherence in a single setup.

## Chapter 3

# Investigation of the effect of interface potential barrier and Auger recombination over the Electroluminescence and its temporal coherence in $\text{In}_{0.5}\text{Ga}_{0.5}\text{As}/\text{GaAs}/\text{Al}_{0.3}\text{Ga}_{0.7}\text{As}$ Quantum dot - Quantum well p-i-n heterostructure

### 3.1 Introduction

Infrared light is very useful in the field of optical data communication<sup>94,95</sup>, medical science<sup>96-98</sup>, astronomy<sup>99,100</sup>, thermal sensing<sup>101,102</sup>, high power industrial lasers and many more. It is evident that studying these infrared emitting materials are important for the point of view of applications as well as the basic science. People are trying to make devices with higher efficiency, lower noise and better stability. Over the last few decades, the advanced growth techniques have provided high quality quantum structures like quantum dots (QD), quantum wires and quantum wells (QW), which are able to improve the desired performance. QD laser diodes (LD) are of special interest due to its expected energy efficiency<sup>103</sup>, temperature stability<sup>104,105</sup>, and spectral sharpness than existing QW lasers<sup>106</sup>. Three dimensional spatial confinement in QDs form condition like atom and sharp energy levels are created. These carrier confinements and discrete energy levels are responsible for low lasing threshold and narrow emission spectra of QD lasers<sup>107-109</sup>. Additionally, different combinations of above given quantum structures can be fabricated to tune in to a desirable optical and/or electrical property. QDs grown inside a barrier layer, QDs grown on top of a barrier layer, multiple layers of QWs, QD inside a QW are few of the examples of different combination of quantum structures. We study in this chapter ‘quantum dot inside quantum well (QD-QW)’ combination designed for light emitting devices. The step-by-step like potential structure provides an extra confinement of charge carriers and finally inject these carriers into QDs for radiative recombination. This type of device level structural modification is expected to improve the yield of QD lasers.



However, we will study in this chapter that this QD-QW configuration also show density dependent Auger recombination (AR) which impacts the coherence of emission.

Although, heterostructures are useful but their functionality greatly depends upon the interface of heterostructure. Due to different bandgaps and different lattice constants, there are many physical factors which controls the electronic and optical defects and the level of electrostatic potential (strain induced or due to carrier transfer) at the interfaces. All these factors affect the carrier transport and final quantum yield of the device. We will show the impact of one such factor where a barrier potential is created between layer of QD and QW due to charge carrier drift and diffusions between two layers of different bandgaps which is significant in low carrier injection regime.

The radiative recombination at cryogenic temperature (~8 K in our case) is mostly dominated by excitonic recombination and its complexes like biexcitons or trions. At higher carrier densities, the probability of non-radiative AR increases and instead of photon emission, a third particle (electron or hole) is excited to higher energy state. There are many studies on AR, although, hardly any investigating the effect of AR on coherence of emission. There are reports of Ga based III-V QDs where full width half maxima (FWHM) of emission is broadened as the excitation intensity (carrier generation) is increased<sup>110-112</sup>. And, FWHM of emission is related to temporal coherence by Wiener-Khintchin theorem as discussed in chapter 2, however, direct measurement of temporal coherence is lacking in literature. Therefore, we probe temporal coherence of emission and its relation to AR. This direct coherence measurement can be crucial to improve quality of QD based devices.

In this chapter, first we discuss the details about samples under our investigation and the experimental setup used during the study. Then, we add elaborated discussions on results and finally conclude the chapter.

## **3.2 Experimental details**

### **3.2.1 Sample Details**

In this chapter, we investigate two samples (A and B) grown in the lab of Prof. Mohamed Henini in University of Nottingham, United Kingdom. Both the samples were grown by molecular beam epitaxy (MBE) on a semi-insulating GaAs (100) substrate. The samples are p-i-n structure where intrinsic layer is sandwiched between two positively and negatively

doped layers. Within the intrinsic region, the self-assembled QDs are grown in QW layer. The details of layers and their growth conditions are following. In sample A, a 500 nm n-type GaAs ( $6 \times 10^{18} \text{ cm}^{-3}$ ) was grown on the substrate at 600 °C. This layer works as bottom electrical contact for the sample. On top of this layer, 80 nm  $\text{Al}_{0.3}\text{Ga}_{0.7}\text{As}$  and six layers of QD-QW is grown. One layer of QD-QW consist 10 nm  $\text{Al}_{0.3}\text{Ga}_{0.7}\text{As}$ , 51 Å of GaAs, and 11 Å of  $\text{In}_{0.5}\text{Ga}_{0.5}\text{As}$  and again 51 Å of GaAs. This way, a  $\sim 100$  Å GaAs/  $\text{Al}_{0.3}\text{Ga}_{0.7}\text{As}$  QW is created and within this QW, a layer of  $\text{In}_{0.5}\text{Ga}_{0.5}\text{As}$  QDs is fabricated. After such six layers, 80 nm  $\text{Al}_{0.3}\text{Ga}_{0.7}\text{As}$  is grown which is followed by a 1.3  $\mu\text{m}$  capping layer consisting highly doped p-type  $\text{Al}_{0.3}\text{Ga}_{0.7}\text{As}/\text{GaAs}$  ( $6 \times 10^{18} \text{ cm}^{-3}$ ) which serve as top electrical contact. On top of this layer, ring-shaped mesas of golden alloy is deposited which has diameter of  $\sim 400 \mu\text{m}$  and area of  $\sim 5 \times 10^{-4} \text{ cm}^2$ . The ring provides the electrical contact while central empty region is used for optical access.

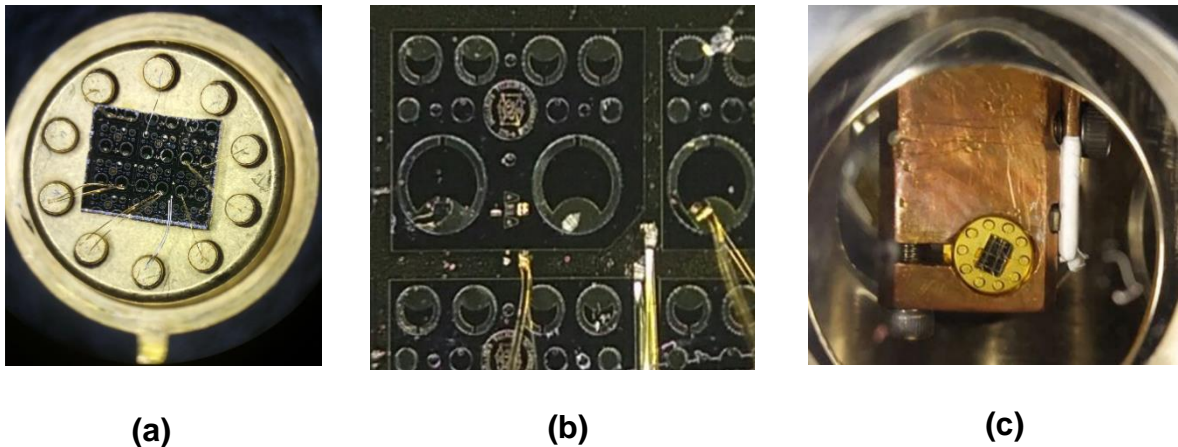


**Fig. 3.1** (a) The sample wafer attached to TO5 package and top electrical contact of ring are attached to package pins. (b) Zoomed image of sample wafer where mesas of diameter 200  $\mu\text{m}$  and 400  $\mu\text{m}$  are shown. Top golden ring contacted with golden wire is to provide top electrical contact. Rectangular strips are bottom electrical contacts. (c) The TO5 package is put in sample holder attached to cold-head of CCR which keeps a sample at a specific temperature.

Sample B is similar to sample A except for three difference; (i) two distributed Bragg reflector layers (DBR) are deposited between p and n-type layers making a DBR cavity. The DBR layer is formed by 20 repetition of  $\text{Al}_{0.6}\text{Ga}_{0.4}\text{As}$  (18 Å) and GaAs(10 Å) at 600 °C on either side of active region (ii) The 80 nm layer of  $\text{Al}_{0.3}\text{Ga}_{0.7}\text{As}$  in sample A is replaced by 110 nm layer in sample B (iii) there are only three layers of QD-QW.

### 3.2.2 Experimental setup and methods

The schematics of electroluminescence (EL) measurement setup is provided in Fig. 3.2 and a representative image of the setup is given in the inset. The sample is kept in a custom made copper sample holder (see Fig. 3.1(c)) designed by Dr. Amit Bhunia, in ARS CS204-DMX-20 closed cycle cryostat (CCR) for temperature dependent measurements. The electrical bias to sample is applied by Agilent E4980A LCR meter in DC mode.

Photodiodes has certain positive capacitance below the bias level of photo-emission. As light emission starts, diode shows negative capacitance<sup>113,114</sup>. Therefore, we measured the EL above the forward bias level where capacitance (AC applied voltage 30 mV at the 1 kHz frequency) goes to negative. Spectra are measured by Thorlabs CCS200 spectrometer. The spectral bandwidth of the spectrometer is  $<2$  nm (@633 nm). We did the  $\lambda^2$  correction<sup>115</sup> during conversion of  $\lambda$ -scale to energy-scale for all the EL data presented in this chapter.

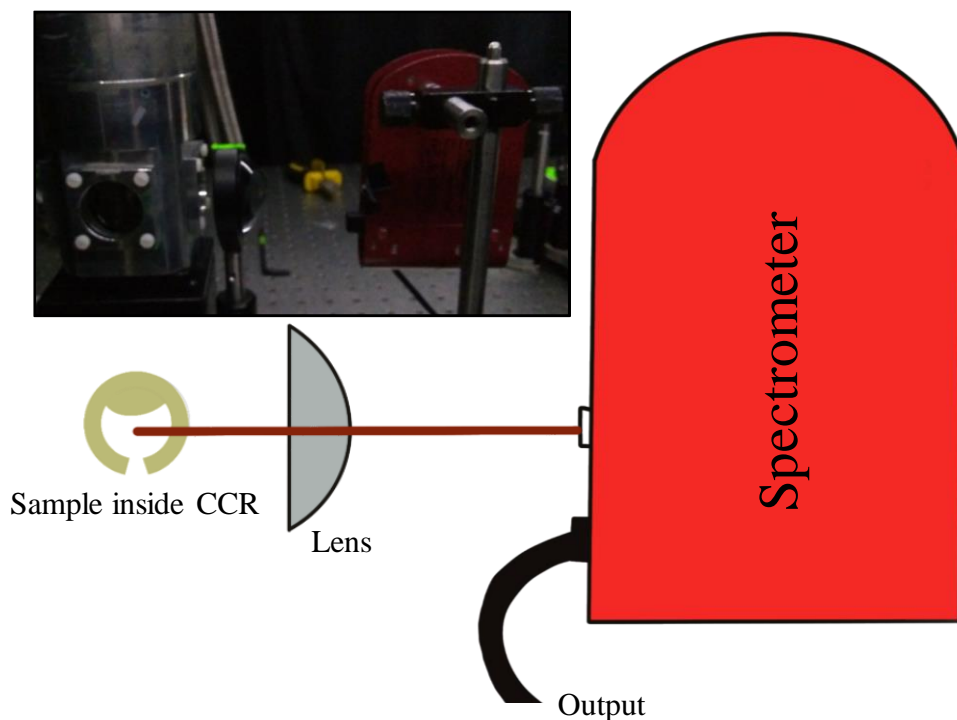


*Fig. 3.2 Schematics of experimental setup for EL measurement. The sample is placed in CCR under controlled temperature condition and emission is focused on the entrance of spectrometer by a plano-convex lens. The dark red line represents the emission direction. In the inset, the real photo of experimental setup is provided.*

For temporal coherence measurement, we used a simple Michelson interferometer setup where two plane mirrors are placed at the two faces of 50:50 beam splitter. The emission of sample is collimated on the beam splitter which split the beam into two beams of equal intensity. These two beams after falling on the mirrors reflect back to the beam splitter and interfere with each other depending upon the level of coherence between two beams. The interfering beams are fed to Acton Research SP2555i monochromator with full spectral bandwidth of  $\sim 9.6$  nm using 3 mm entrance and exit slits. The monochromator is able to spectrally separate different bands in EL emission. The output of monochromator is collected by Thorlabs BC106N-VIS/M CCD camera. The two mirrors of Michelson setup are connected

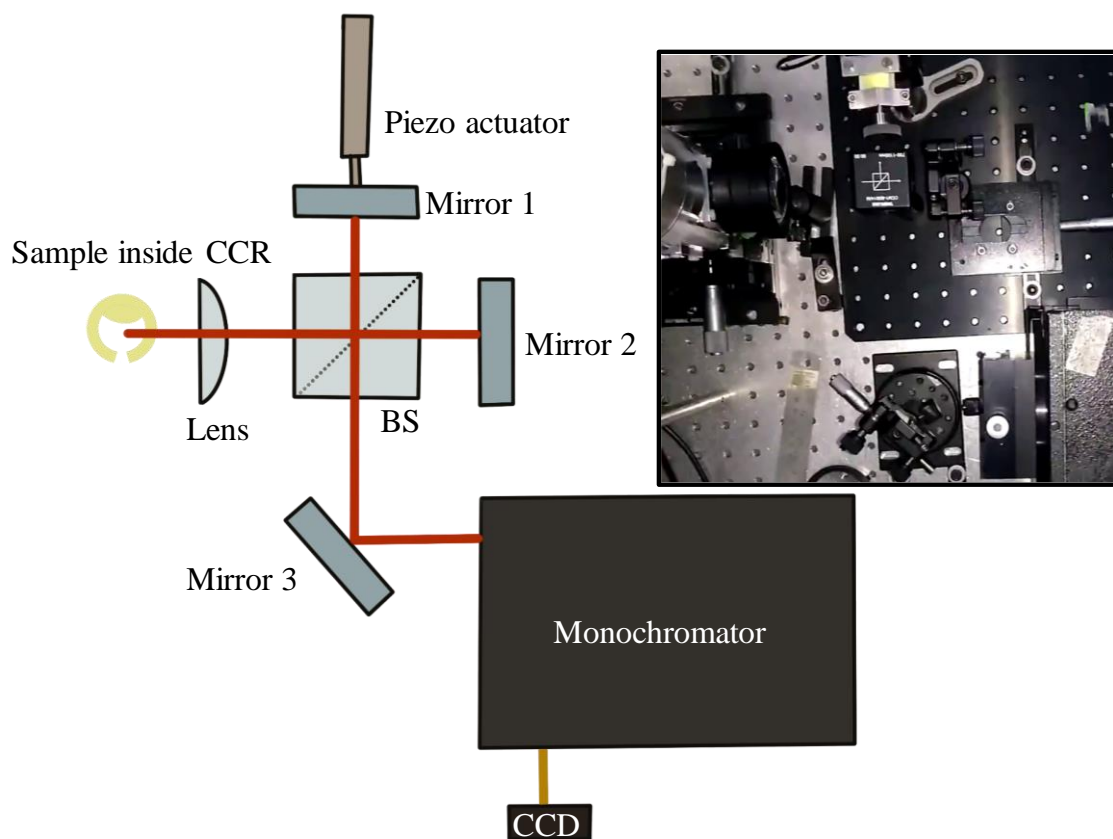


**Fig. 3.3** Schematics of autocorrelation measurement setup. The EL is collimated to BS and reflected back by Mirror 1 and Mirror 2. The reflected beams interfere and are fed to monochromator via Mirror 3. The monochromator is able to spectrally separate the contribution of two bands from pattern of interference. The dark red line represents the emission propagation. In the inset, the real photo of setup is given.

to piezo (PAS005, Thorlabs) and micro-meter linear stage, respectively. The piezo is controlled by home-made piezo controller and micro-meter stage is controlled with the help of a stepper

motor. The specified resolution of piezo is 20 nm and linear stage has resolution of 10  $\mu\text{m}$ . The piezo and stepper motor system is further calibrated and described in details in the Chapter 4. The piezo and stepper can move the Mirror 1 and 2 in direction of propagation of light and create difference in the path length travelled by split beams. The path difference results in difference of traveling time of both beams and thus, any path difference is equivalent to temporal difference between two beams. That is how, a temporal delay ( $\Delta\tau$ ) is introduced between two beams. However, for the autocorrelation experiment in this chapter, both the mirrors are kept at approximately equal length from the beam splitter and  $\Delta\tau \sim 0$ . First order temporal correlation function  $|g^{(1)}(\Delta\tau)|$  is measured by calculating the visibility of interference pattern.

$$|g^{(1)}(\Delta\tau)| = \text{Visibility} = \frac{I_{max} - I_{min}}{I_{max} + I_{min}} \quad (3.1)$$

Here,  $I_{max}$  and  $I_{min}$  are the maximum and minimum intensity of interference fringe pattern. The coherence measurements are done in the low-vibration mode of the cryostat.

### 3.3 Experimental Results of sample A

#### 3.3.1 Bias dependence of electroluminescence at $\sim 8.8$ K under low current regime ( $< 2.2$ mA)

The EL spectra are taken at different bias voltages at the constant temperature  $\sim 8.8$  K and the results are given in Fig. 3.4(a), (b) and (c). The combined spectra are also plotted as contour plot in Fig. 3.4(d). There are two clear distinct energy bands visible from the plot. The lower energy band is around 1.33 eV and higher energy band is around 1.47 eV. To understand the origin of these bands, the schematics of band diagram is drawn in Fig. 3.5(a). The lower energy band is coming from  $\text{In}_{0.5}\text{Ga}_{0.5}\text{As}$  QDs and higher energy, which is broader and seems to have convolution of two or more peaks is coming from  $\text{GaAs}/\text{Al}_{0.3}\text{Ga}_{0.7}\text{As}$  QW and wetting layer (WL). Hereafter, this peak is referred as QW-WL peak in this chapter.

In Fig. 3.4(c), it is seen that QW-WL peaks are more prominent at lower bias currents and only dominated by QD peak at higher bias current. In the contour plot Fig. 3.4(d), the QW-WL emission appears first when increasing the bias current. This indicates that at the lower injection levels of charge carriers, the major radiative recombination does not happen in QDs, but QW-WL. However, at higher injection currents, the QD emission start to dominate and

QW-WL peaks almost saturate. In a simple minded picture, a step by step potential should allow charge carrier to immediately go to QDs and ideally major radiative (or non-radiative) recombination should happen inside QD. However, the above data suggests a hindrance of charge carrier which prevent these from getting into QDs at lower injection current. To understand this observations, we present a schematic of the QD-QW heterostructure and its potential landscape in Fig. 3.5(a) and (b), respectively. There is a layer of potential barrier around the QD as shown by grey shadow in Fig. 3.5(a) (in zoomed section of layers at the right) and in inset of Fig. 3.5(b). This layer is likely to be created by transfer of electron from higher GaAs conduction band to low potential region of  $\text{In}_{0.5}\text{Ga}_{0.5}\text{As}$  conduction band at the interface of two layers. This type of charge depleted potential barriers are dynamically produced due to combined effects of drift and diffusion of electrons at the conduction band.

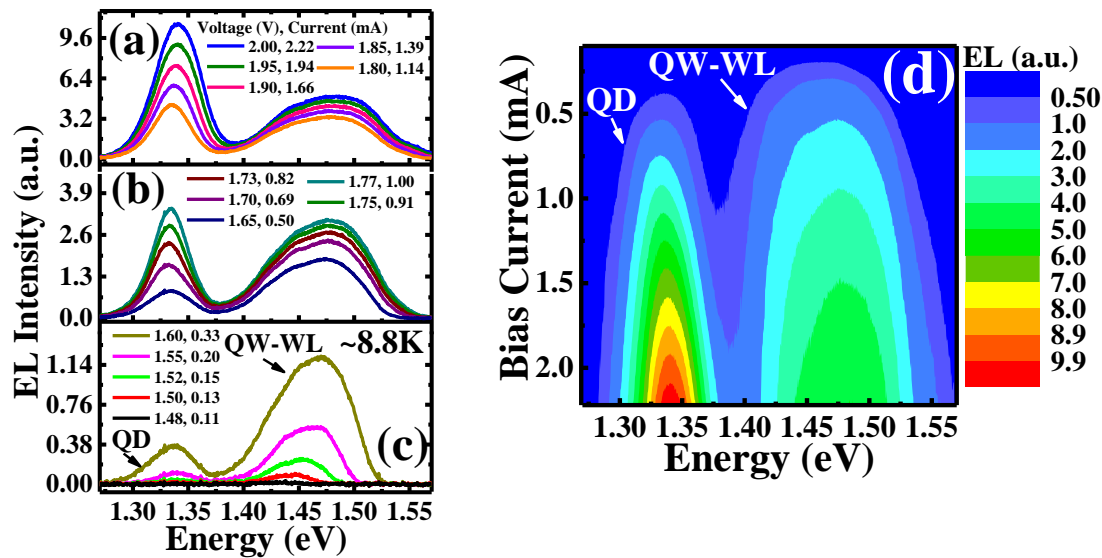


**Fig. 3.4** (a)-(c) EL spectra of  $\text{In}_{0.5}\text{Ga}_{0.5}\text{As}/\text{GaAs}/\text{Al}_{0.3}\text{Ga}_{0.7}\text{As}$  QD-QW heterostructure at  $\sim 8.8\text{K}$  for different bias voltage and their corresponding currents. (d) 2D Contour plot of all spectra at different bias current. The emission around 1.33 eV is from QDs while 1.47 eV is from QW-WL.

At low injection level, the carrier gets trapped inside QW and are not able to jump to the QDs due to the potential barrier. These electrons then recombine with the available holes in the valance band to emit light. This is the reason we witness a major emission from QW-WL as shown in Fig. 3.4(c). As the carriers are increased by increasing the injection current, the electron eventually cross the potential barrier and get into the QDs. As the injection current keep increasing, the QW-WL emission saturates after a particular bias and QD emission

increases exponentially. A similar study based on the potential barrier at the interface of an InAs/In<sub>0.15</sub>Ga<sub>0.85</sub>As/GaAs QD-QW system is done by Popescu *et al.*<sup>116</sup> and Mu *et al.*<sup>117</sup>. Both the authors claimed the reason for potential barrier is compositionally induced strain due to lattice mismatch at the interface of heterostructure. These potential barriers are formed in both

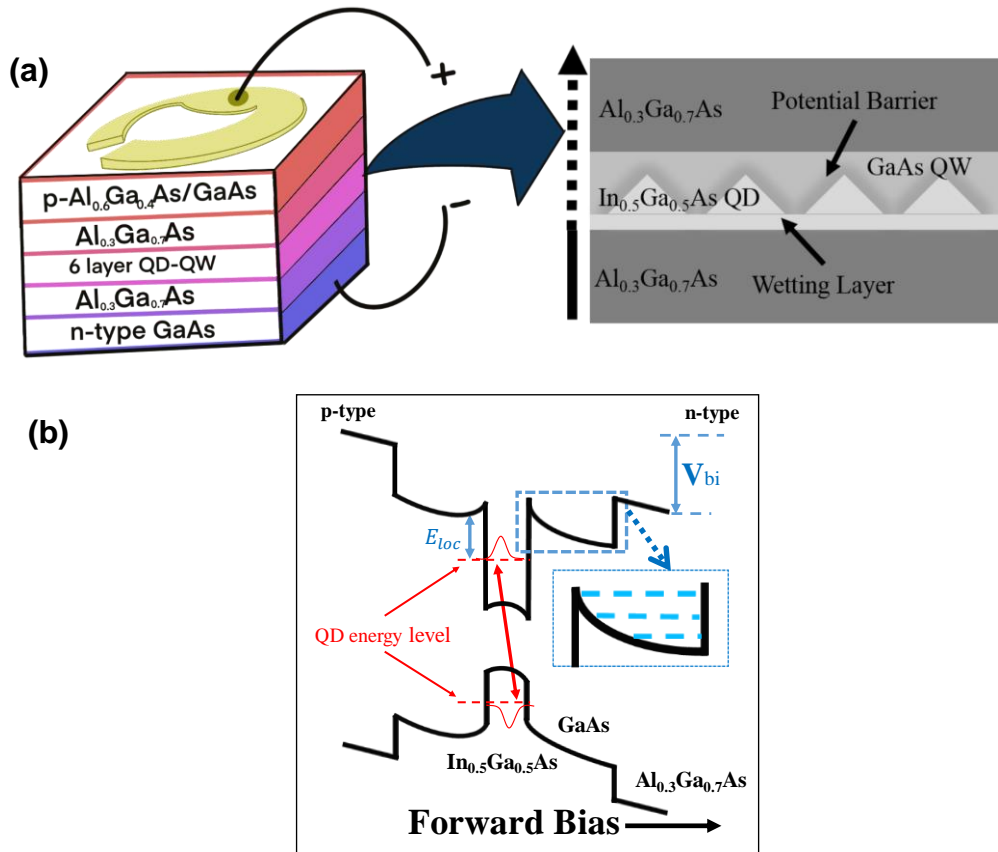


**Fig. 3.5** (a) (Left) Schematic diagram of sample layers. Different colours represent different layers of materials. Top golden ring and bottom n-type GaAs is for electrical contact. The device is being used in forward bias mode. The central active region is magnified to the right side of the diagram. The QW is formed between two Al<sub>0.3</sub>Ga<sub>0.7</sub>As layers (dark grey) and inside the QW, the light grey pyramids are self-assembled In<sub>0.5</sub>Ga<sub>0.5</sub>As QDs over the wetting layer (WL). The grey shadow over QDs represent the potential barrier between QD and QW. The dashed upward arrow shows the repeated layers in the growth direction. (b) Schematics of band diagram of one layer of QD-QW layer. The blue dashed square shows the potential barrier and different energy levels of QW. The forward bias is shown by black arrow. The red dashed lines are energy levels of QD. V<sub>bi</sub> is built-in potential. E<sub>loc</sub> is localization energy<sup>122</sup>.

conduction and valance band. However, we have mostly focused on the effect of potential barrier in conduction band on the EL. Popescu *et al.* proposed that the potential barrier can act as an added activation energy for carriers to escape from QDs other than the usual thermal activation energy.

Before discussing the analysis of these spectral results, it is required to understand some of these numbers related to band offset. The band offset between  $\text{In}_{0.53}\text{Ga}_{0.47}\text{As}$  and GaAs in the conduction band ( $\Delta E_c^{QD}$ ) is reported to be  $\sim 0.43\text{eV}$  at  $4.2\text{K}$ <sup>118</sup>. Similarly, the reported conduction band offset between  $\text{Al}_{0.32}\text{Ga}_{0.68}\text{As}$  and GaAs is  $\Delta E_c^{QW} \sim 0.25\text{ eV}$ <sup>119–121</sup>. Evidently, higher magnitude of band offset at the interface of two layers should also produce higher potential barrier due to larger potential difference and consequently, greater number of charge transfer. Ideally, there should also be some electronic/optically active states at the interface of  $\text{Al}_{0.3}\text{Ga}_{0.7}\text{As}/\text{GaAs}$  interface but we did not see any emission in the above current ranges. However, at higher current bias ( $>5\text{ mA}$ ), there is small emission at  $1.85\text{ eV}$ . If we compare the emission energy from  $\text{Al}_{0.3}\text{Ga}_{0.7}\text{As}$  and GaAs, and apply empirical rule of 60:40 which is commonly used for GaAs/AlGaAs systems, we find  $\Delta E_c^{QW} = 0.23\text{ eV}$  which is in good agreement with reported result. Small difference in calculated and reported values may come because we do not include the effect of WL and excitonic binding energies of  $\text{Al}_{0.3}\text{Ga}_{0.7}\text{As}$  and GaAs layers. On the other hand, if we compare the emission energy of GaAs and  $\text{In}_{0.5}\text{Ga}_{0.5}\text{As}$ , the  $\Delta E_c^{QD} = 0.08\text{ eV}$  which is significantly smaller than the reported value. This indicates that ground state energy levels are quite elevated in conduction and valance band (indicated by red dashed line in Fig. 3.5(b)). The elevated energy levels are due to high gallium content and small size of QDs. The difference between conduction band of GaAs and ground state energy level of QD is represented as localization energy,  $E_{loc}$ <sup>122</sup>

$$E_{loc} = \Delta E_c^{QD} - E_1^{QD} \quad (3.2)$$

where  $\Delta E_c^{QD}$  is conduction band offset of  $\text{In}_{0.5}\text{Ga}_{0.5}\text{As}/\text{GaAs}$  and  $E_1^{QD}$  is ground state energy level of QDs. Therefore,  $E_{loc}$  depends upon the size of QD and its gallium content. Now, we discuss the peak emission of  $\text{In}_{0.5}\text{Ga}_{0.5}\text{As}$  QDs at  $\sim 8.8\text{ K}$ . In the spectral results of Fig. 3.4(a)-(c), the QD peak is fitted with Gaussian function and their peak energy and FWHM are plotted in Fig. 3.6(a) and (b). The QD peak is slightly blue shifted at higher ( $> 1\text{ mA}$ ) but FWHM is not linear in nature. It first decreases below  $1\text{ mA}$  and then increases. To understand such nature, we again refer to Fig. 3.5(b) where a built-in potential ( $V_{bi}$ ) is shown as potential difference two ends of active layer. Due to p-i-n nature of device, p-side is energetically higher



than n-side and there is a potential gradient in the intrinsic region of sample. When forward bias is applied, the effective potential field in the active region is reduced by the  $V_{bi}$ .<sup>52</sup>

$$V_{eff} = V_{bi} - V_{app} \quad (3.3)$$

Here,  $V_{app}$  is the applied bias potential to the device. In the initial bias condition between 0.5 mA to 1 mA, the  $V_{app}$  is increasing while  $V_{eff}$  is reducing. This reduction in  $V_{eff}$  leads to the process of reverse quantum-confined Stark effect (QCSE)<sup>123</sup> which can reduce the FWHM in the above mentioned bias range. QCSE in a QD is shifting of energy levels in the presence of potential field in confinement of QD. The conduction band electron energy level reduces while valence band hole energy level raises up if potential field is increasing. This shift of energy level also shifts the electron and hole wave function away leading to increased FWHM.

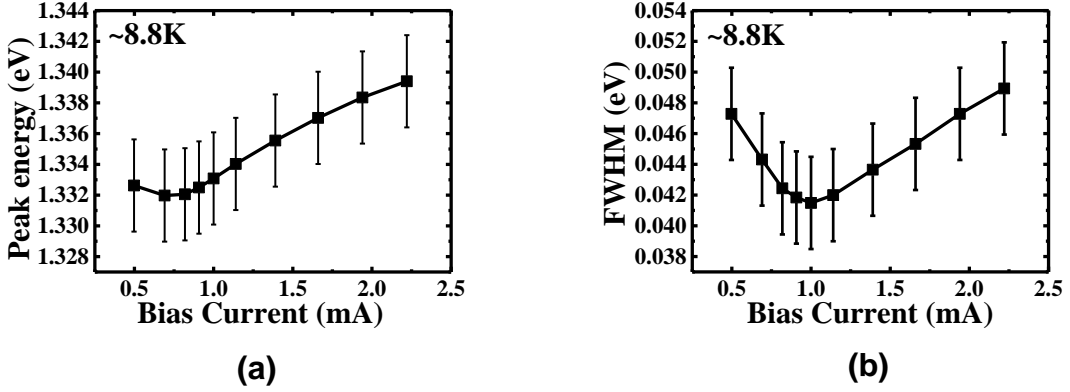


**Fig. 3.6** (a) Peak energy and (b) FWHM of Gaussian fit of QD peak in spectra of Fig. 3.4(a)-(c) at ~8.8K. The error bars are combined contribution of experimental bandwidth ( $\Delta E \sim 3$  meV) and standard deviation from the Gaussian curve fitting.

However, since the application of  $V_{app}$  is reducing the  $V_{eff}$ , we see a reverse QCSE where FWHM is decreased on the increase of applied bias. At applied bias ( $> 1$  mA), the FWHM is increased and peak energy is also blue shifted. This can be explained with the combined effect of QCSE and band filling effect<sup>124</sup>. It is possible that reverse QCSE is more effective at lower bias while band filling effect is more effective at bias  $> 1$  mA. Also, above this bias current, the carrier density in QDs will increase and this increased density may lead to Auger recombination (AR)<sup>124-126</sup>. Such non-radiative process may lead to increased FWHM as reported in this chapter.

Now, we compare the light emission from QD and QW-WL to understand the carrier dynamics between these two emitting sources at  $\sim 8.8$  K. The integrated EL (*Int. EL*) is estimated by calculating the area under the fitting Gaussian. The *Int. EL* is plotted in Fig. 3.7(a) and it can be seen that emission from QW-WL saturates at higher bias current while QD emission rises exponentially. To further clarify this transition, we also plotted  $Int. EL (QW - WL) - Int. EL (QD)$  and  $Int. EL (QW - WL) / Int. EL (QD)$ . The former quantity first rises

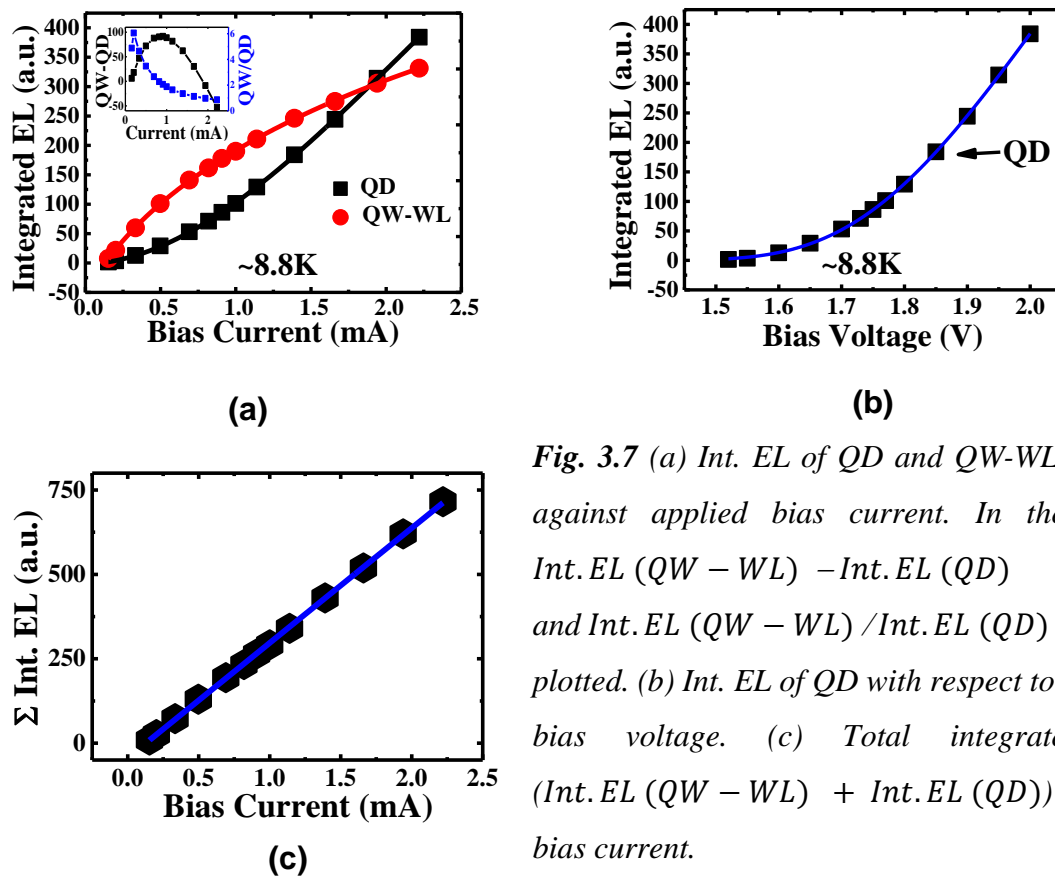


**Fig. 3.7** (a) *Int. EL* of QD and QW-WL plotted against applied bias current. In the inset,  $Int. EL (QW - WL) - Int. EL (QD)$  and  $Int. EL (QW - WL) / Int. EL (QD)$  are plotted. (b) *Int. EL* of QD with respect to applied bias voltage. (c) Total integrated EL ( $Int. EL (QW - WL) + Int. EL (QD)$ ) against bias current.

and later goes to negative indicating the greater emission form QD. The later quantity goes  $< 1$  to indicate the same transition. Such saturation and increase in emission of QW-WL and QD, respectively can easily be explained by the existence of barrier potential at the interface of QD and QW.

However, we also want to quantitatively estimate the role of potential barrier in such light emission. So we plotted the  $Int. EL (QD)$  with respect to bias voltage. It shows an exponential increase which is expected from p-i-n diode sample. However, determining the type of exponential can give us some information about the role of barrier potential over

emission. We derived a simple model, based on the Shockley diode model<sup>127</sup> and diode equation is given below,

$$I(V, T) = I_0 \left[ e^{\left(\frac{eV}{k_b T}\right)} - 1 \right] \quad (3.4)$$

The Eq. (3.4) can be written in differential form as,

$$\frac{dI}{dV} \propto (I + I_0) \quad (3.5)$$

$I_0$  is reverse saturation current and it can be ignored in the proportionality equation since we are working in forward bias and at a constant temperature where  $I_0$  is approximately constant. The Eq. (3.5) can be replaced with

$$\frac{dI}{dV} \propto I \quad (3.6)$$

In Fig. 3.7(c), we have plotted total integrated EL i.e.  $\sum Int.EL = Int.EL(QW - WL) + Int.EL(QD)$  and found it to be directly proportional to injection current. In the proportionality Eq. (3.6), the 'I' can be replaced with  $\sum Int.EL$  and proportionality will still hold.

$$\frac{d(\sum Int.EL)}{dV} \propto \sum Int.EL \quad (3.7)$$

The above result does not yield any information about individual emission of QD and QW-WL but only combined effect is approximated. If similar relation is to be found for QD i.e.  $\frac{d(EL(QD))}{dV}$ , the mutual dependence of QD and QW-WL emission due to barrier and applied bias has to be included. We do not know exact relation between potential barrier and emission of QW-WL, however, we understand that potential barrier should change with applied bias and consequently change the QW-WL emission. We then propose that Eq. (3.7) can be written for EL (QD) if we include additional applied bias term to incorporate the effect of QW-WL. Such empirical inclusion of bias term, according to our data is

$$\frac{dEL(QD)}{dV} \propto EL(QD)/V^n \quad (3.8)$$

The proportionality can be removed with a constant sign,  $\alpha$

$$\frac{dEL(QD)}{dV} = \alpha \times EL(QD)/V^n \quad (3.9)$$

After solving this differential equation, we finally get a stretched exponential,

$$EL(QD) = A. \exp\left(\frac{-\alpha}{mV^m}\right) \quad (3.10)$$

here,  $A$  is integration constant and  $m = (n + 1)$ . We think that  $\alpha$  can have an inverse temperature dependence, however, we only worked at constant temperature of this study and exact temperature dependence cannot be found. The estimated parameters from the Eq. (3.10) for EL (QD) as shown in Fig. 3.7(b) are

$$A = 1482 \pm 72 \text{ a.u.}, \alpha = 365 \pm 28 \text{ a.u. and } m = 5.6 \pm 0.1$$

Here the value of  $m$  can quantify the role of potential barrier. Higher the value of  $m$ , sharper is the increase in exponential growth of  $\sum EL(QD)$ , indicating the lower interface potential barrier. Therefore,

$$m \propto \frac{1}{\text{Potential barrier height}} \quad (3.11)$$

Finally, in this section, we discuss about the type of carrier recombination happening  $\sim 8.8$  K. This is because, at these cryogenic temperatures, the defect related non-radiative recombination are suppressed and excitonic recombination are major channels for emission both in QDs and QW. We fit log-log plot of *Int. EL* vs bias current of QD and QW-WL as show in Fig. 3.8. The power law exponent for *Int. EL (QD)* is found to be  $1.78 \pm 0.02$  and for *Int. EL (QW - WL)*, it is  $0.78 \pm 0.02$ . In case of QW-WL, the power exponent is close to unity

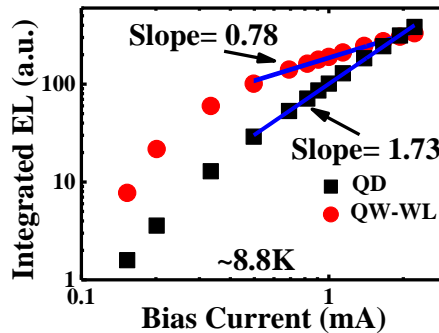


**Fig. 3.8** *Int. EL of QD and QW-WL plotted against bias current in log-log scale. The linear fit shows the exponent values of 1.73 and 0.78 for QD and QW-WL, respectively.*

that points towards the presence of excitonic recombination in QW-WL which is quite evident at such cryogenic temperatures. Moreover, the power exponent in QD is close to  $\sim 2$ . This type

of power exponent implies the bi-molecular recombination of free electron and holes. However, we have discussed earlier that after a particular bias, the effect of barrier potential is diminished. Subsequently, we witness an exponential increase in EL of QD due to higher carrier reception in QDs. Additionally, QDs are quantum structures which spatially confine electrons and holes from all three dimensions and thereby increasing the probability of existence of trions or biexcitons as well. Therefore, we relate the power exponent  $\sim 2$  to the symptomatic presence of trions or biexcitons related radiative recombination in QDs<sup>128</sup>. The existence of trions or biexcitons in QDs also implies the possibility of non-radiative AR of these excitonic complexes<sup>125</sup> and thus explains the broadening of EL in as shown in Fig. 3.6(b).

### 3.3.2 Temperature dependence of electroluminescence at constant bias

As we know, while increasing the temperature, more channels of defect/trap assisted non-radioactive recombination get activated further. Thermal escape of carriers from quantum structures (QD, QW) also reduces the number of radiative recombination and these two reasons

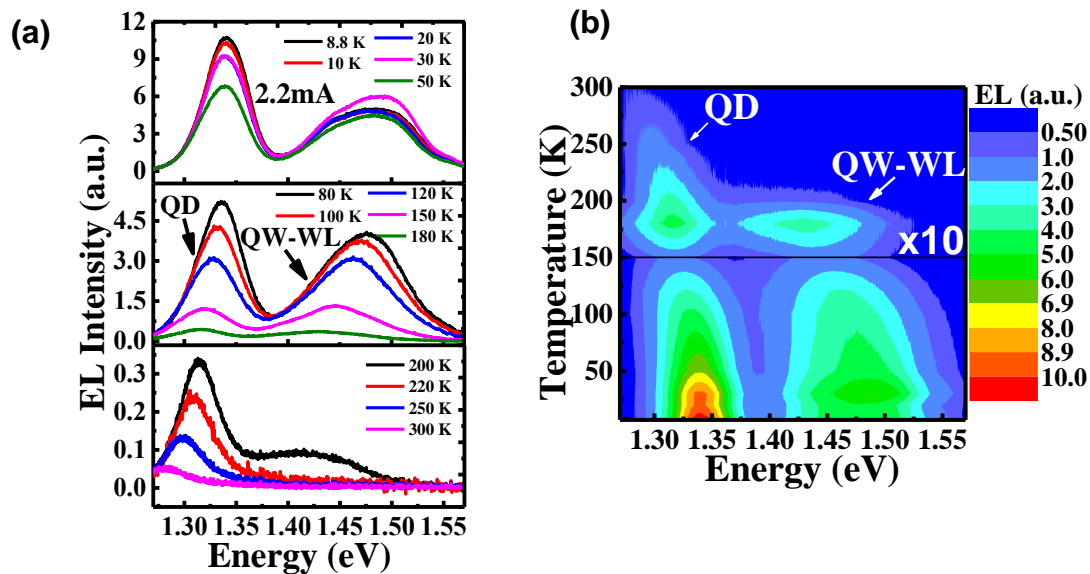


*Fig. 3.9 (a) EL spectra of  $\text{In}_{0.5}\text{Ga}_{0.5}\text{As}/\text{GaAs}/\text{Al}_{0.3}\text{Ga}_{0.7}\text{As}$  QD-QW heterostructure at  $\sim 2.2$  mA for different temperatures. (d) 2D Contour plot of all spectra at different temperatures. The emission around 1.33 eV is from QDs while 1.47 eV is from QW-WL. The QD emission survives up to 300 K while QW-WL emission is not detected after 200 K.*

usually quench any luminescence at increasing temperatures. To detect EL for broad range of temperature, we selected the highest bias from the range used in previous section. We measured

EL at a constant bias of  $\sim 2.2$  mA from  $\sim 8.8$  K to 300 K as show in Fig. 3.9(a). We see a red shifted emission from QD up to 300 K while QW-WL is not noticeable after 200 K. At this bias, the carriers can easily cross the barrier potential and any significant role of barrier is not expected over the investigated temperature range. However, for any QD-based light emitting device which has low threshold will be affected by this type of barrier potential. The major reason for quenching are non-radiative defect/tract activation and carrier escape for QDs and QW-WL. The required thermal energy for thermal escape of electron from QD is localization energy,  $E_{loc} \sim 140$  meV (See section 3.3.1) and same for QW-WL is band offset between GaAs and  $\text{Al}_{0.3}\text{Ga}_{0.7}\text{As}$ ,  $\Delta E_c^{QW} \sim 250$  meV. Even with such smaller escape potential, the emission from QD is seen up to room temperature which is possible due to three dimensional spatial confinement of carrier and their higher probability of recombination. On the other hand, QW-WL survived up to  $\sim 200$  K despite receiving escaped electrons from QDs. This implies that thermal escape from QW to  $\text{Al}_{0.3}\text{Ga}_{0.7}\text{As}$  and non-radiative recombination are more dominant at higher temperatures than radiative recombination in QW-WL.

As noticed, the QD peaks are red shifted with increasing temperature which is usual due to bandgap reduction. However, to know if there are other mechanism which may affect

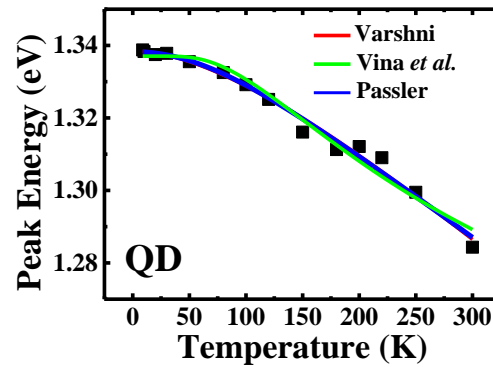


**Fig. 3.10** Peak energy of EL (QD) vs temperature for bias current of  $\sim 2.2$  mA (black squares). The peak energy is fitted with three models: Varshni (red), Vina *et al.* (green) and Passler (blue) which theoretically predict the bandgap change with temperature.

the peak energy of emission, we plotted peak energy of QD against temperature in Fig. 3.10 and fitted with three models namely Varshni<sup>129</sup>, Vina *et al.*<sup>130</sup> and Passler<sup>131</sup>. The fitting model formulae and their fitted parameters are given in table 3.1. Earlier study of QD emission with respect to temperature<sup>132,133</sup> shows sigmoidal behaviour of QD peak energy with temperature. In some cases, the peak energy is red shifted more than predicted by Varshni formula. The

carriers at higher temperature preferably goes to larger quantum dots due to their lower energy level. Such carrier redistribution readily happens via channel like wetting layer. However, we do not see any such variation in peak energy despite QDs having a wetting layer and lower localization energy ( $E_{loc}$ ). The possible reason for no such behaviour is fairly uniform sized QDs and their narrow size distribution.

<b>Table 3.1</b> Fitted parameter of Varshni, Vina <i>et al.</i> and Passler model for peak energy of QD			
Models:	Varshni	Passler	Vina <i>et al.</i>
	$E(T) = E(0) - \frac{\alpha T^2}{\beta + T}$	$E(T) = E(0) - \frac{\alpha\theta}{2} \left( \sqrt[4]{1 + \frac{\pi^2}{6} \left(\frac{2T}{\theta}\right)^2 + \left(\frac{2T}{\theta}\right)^4} - 1 \right)$	$E(T) = a - b \left( 1 + \frac{2}{e^{\frac{T}{\theta}} - 1} \right)$
E(0) (eV)	1.338	1.338	$a = 1.361 \pm 0.003$ eV
$10^{-4} \alpha$ (eV/K)	$3.0 \pm 0.5$	$2.4 \pm 0.2$	$b = 0.023 \pm 0.004$ eV
$\beta$ or $\theta$ (K)	$\beta = 230 \pm 87$	$\theta = 205 \pm 47$	$\theta = 300 \pm 36$

In Fig. 3.11(a), different possible carrier transport mechanism are shown which are involved in investigated sample. Injected carriers goes from  $\text{Al}_{0.3}\text{Ga}_{0.7}\text{As}$  barrier layer to GaAs QW and finally drops in  $\text{In}_{0.5}\text{Ga}_{0.5}\text{As}$  QD. These downward transitions (on energy scale of carrier) are shown as downward arrow. As temperature of sample rises, carrier jumps to escape the lower energy state. These are indicated as thermal escape ( $\text{TE}_{1/2}$ ) for QD and QW. Electron-hole recombination, either radiative or non-radiative are shown as side arrows indicating the departure from system. The grey line between  $\text{In}_{0.5}\text{Ga}_{0.5}\text{As}$  QD and GaAs QW is barrier potential discussed in section 3.3.1. To find activation energy of EL quenching, integrated EL of QD and QW-WL is plotted with respect to  $1/T$  and fitted with Arrhenius equation<sup>116</sup> with single activation energy.

$$I(T) = \frac{I_0}{1 + A \cdot \exp\left(-\frac{E_a}{k_b T}\right)} \quad (3.12)$$

here,  $k_b$  is Boltzmann constant,  $I_0$  is the integrated EL at  $\sim 8.8$  K,  $E_a$  is the activation energy, and  $A$  is a pre-exponential factor. The fitting values of  $E_a$  and  $A$  are given in table 3.2. The fitted activation energies for EL quenching for QD as well as QW-WL is below the potential energies,  $E_{loc}$  and  $\Delta E_C^{QW}$  (see section 3.3.1) required for thermal escape. However, such carrier escape is still possible due to the existence of thermodynamically non-zero probability of carrier escape i.e.  $\sim \exp(-E_a/k_bT)$  from such potential wells. Since, we only fitted single activation energy for EL quenching, it is assumed that this activation energy includes the combined effect of thermal escape as well as defects related non-radiative recombination.

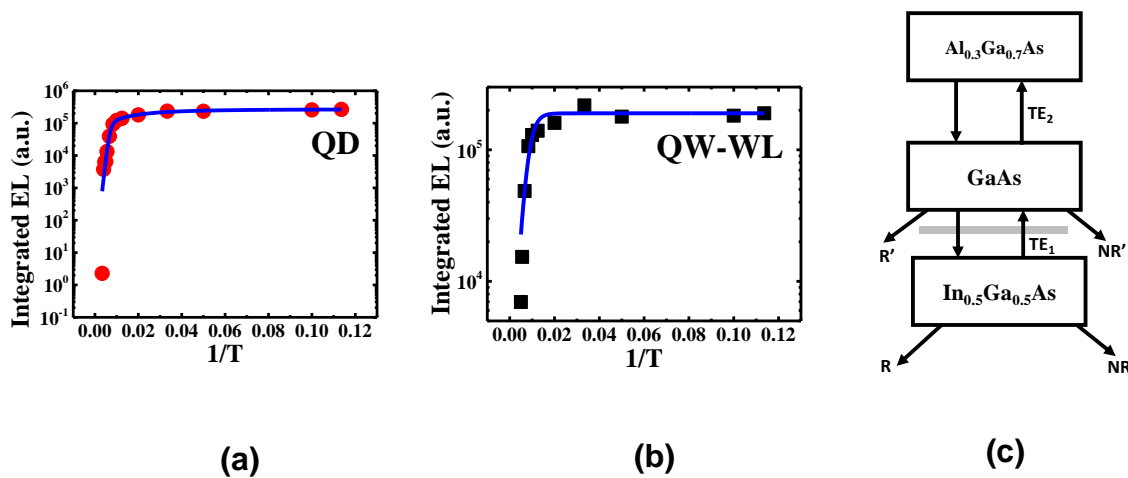


**Fig. 3.11** Int. EL of (a) QD and (b) QW-WL emission plotted against  $1/T$ . The blue solid line is fit of Arrhenius equation with single activation energy. (c) shows different mechanism of carrier transport.  $R$  and  $NR$  are radiative and non-radiative recombination from QD, respectively. Similarly,  $R'$  and  $NR'$  are radiative and non-radiative recombination in QW.  $TE_1$  and  $TE_2$  represent thermal escape of carrier from QD and QW-WL, respectively shown as upward arrow. The downward arrow shows carrier drop in lower energy state. The grey line between  $In_{0.5}Ga_{0.5}As$  QD and  $GaAs$  QW indicates the potential barrier.

<b>Table 3.2</b> Fitted values of Arrhenius equations Eq. (12) for QD and QW-WL, respectively	
<b>QD</b>	<b>QW-WL</b>
$E_a = 21 \pm 4$ meV	$E_a = 52 \pm 10$ meV
$A = 25 \pm 14$	$A = 201 \pm 192$



### 3.3.3 Temporal Coherence of QD and QW-WL emission at higher forward biases (1 mA – 16 mA) and at various temperatures

In section 3.3.1 and 3.3.2, emission spectra of QD and QW-WL up to 2.2 mA are studied. In the smaller current regime, the role of barrier potential and its subsequent effect on electron transport is determined. In the higher current regime where barrier potential has no significant contribution, optical temporal coherence of both (QD and QW-WL) bands of emitted light are measured. Phase fluctuations and decrease in coherence can indicate some disruptive type of phenomena such as Auger recombination, scattering or phase transition etc. In this section, at higher currents, the Auger recombination and its impact on coherence is investigated.

As elaborated in section 3.2.2, a Michelson interferometer is used to produce optical interference pattern of the light coming out of these samples. That fringe pattern is then spectrally filtered through monochromator to individually measure the coherence of two bands. The one dimensional (1D) fringe pattern is recorded by CCD and the visibility of those fringes are estimated. The interference pattern's stability is very sensitive to surrounding environment, therefore, the whole setup is covered and operated over a floating optical-table. We recorded 30 fringe pattern in a single run for any measurement. Fluctuations in fringe pattern are indicator of noises in the environment (if those fluctuations are not intrinsic to the system itself) and room temperature CCD used for these measurements also show hot-pixel related errors where one pixel shows erroneously high intensity. Such errors can lead to incorrect maxima measurement required in estimation of visibility. Therefore, these 30 patterns are averaged and mean value is taken to calculate visibility. The standard deviation of these averages are 1-2 order of magnitude lower than mean intensity of fringes which shows the well-controlled surrounding of the experiment.

The results of temporal coherence at ~10 K are plotted in Fig. 3.12(a). In QDs emission, the  $|g^{(1)}(\Delta\tau)|$  is decreasing with increasing bias which is possible due to AR at higher biases. AR is non-radiative phenomenon which dominates at high carrier densities and in lower bandgap materials. Such non-radiative recombination suppresses the luminescence and disrupts the optical coherence. QDs, being spatially confined, can possess higher carrier density which can reach the threshold of AR process. Moreover, the step-by-step band structure for extra carrier confinement can also add to increased intensity in QDs.

On the other hand, the QW-WL is not affected by AR and  $|g^{(1)}(\Delta\tau)|$  increases with bias. Here, the reasons we mentioned for QD are not dominating. For example, the QW-WL recombination occur with remaining carriers which can not constitute density high enough for AR. QW-WL has higher band gap and lesser spatial confinement than QDs. Also, in section 3.3.1, we attributed the power law exponent of integrated EL vs bias current to the presence of trion or biexcitons in QDs. Since AR is also three particle process, the trions can effectively contributes to the process of AR as concluded by Kurzmann *et al.*<sup>125</sup> for InAs/GaAs QDs. Therefore, in our sample, the presence of trions in QDs and loss of coherence at higher bias agrees with the above explanations. At  $\sim 15$  mA,  $|g^{(1)}(\Delta\tau)|$  is measured at varying temperatures (from  $\sim 10$  K to  $\sim 300$  K) for QD and QW-WL as shown in Fig. 3.12(b). Contrary to the

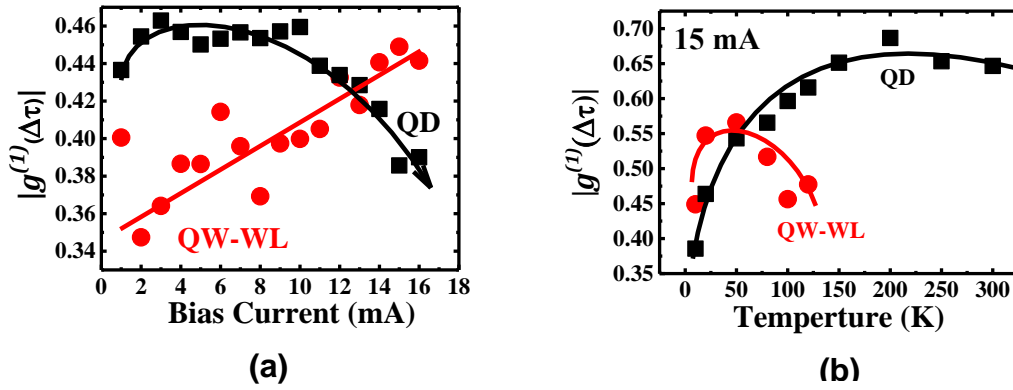


**Fig. 3.12** First order correlation function,  $|g^{(1)}(\Delta\tau = 0)|$  plotted against (a) bias current and (b) temperature for QD and QW-WL emission. The solid lines are guide for eyes only.

expectations, QD coherence increases with increasing temperatures and then saturates. As per above explanation, this suggests that AR is reduced which is possible due to low localized energy  $E_{loc}$  for QDs. At higher temperature, the carrier from QDs energy level (see Fig. 3.5(b)) can easily jump in to QW reducing the carrier density in QDs below the AR threshold. As a result of this effective reduction in carrier density, there is a subsequent decrease in AR<sup>134,135</sup> and an increase in coherence as a consequence. However, coherence of QW-WL is not affected due to absence of any significant AR and it shows decline after  $\sim 50$  K due to usual non-radiative recombination with increasing temperature. We could measure temporal coherence of QW-WL up to  $\sim 120$  K only due to luminescence quenching at higher temperatures and emission is small enough to give any significant estimation of  $|g^{(1)}(\Delta\tau)|$ .

To the best of our knowledge, this is the first report on the physical connection between the AR and optical coherence<sup>136</sup>. Here we monitor two important parameters for the performance of QD light emitting diode (LED), the efficiency and the temporal coherence of light. Efficiency demands more carriers to get in QD for better yield. On the other hand, coherence reduces if AR is effective due to higher carrier density. There is an intricate interplay between yield and coherence which could be very useful information to optimize a QD based LED or laser diodes (LD) from the application point of view. Therefore, spectrally selective measurement of optical coherence can be used as a method to sense AR and improve overall performance of QD base devices.

Additionally, the spectral experiments are tried on different mesa on the same wafer chip and results are reproducible as shown in Fig. 3.13.

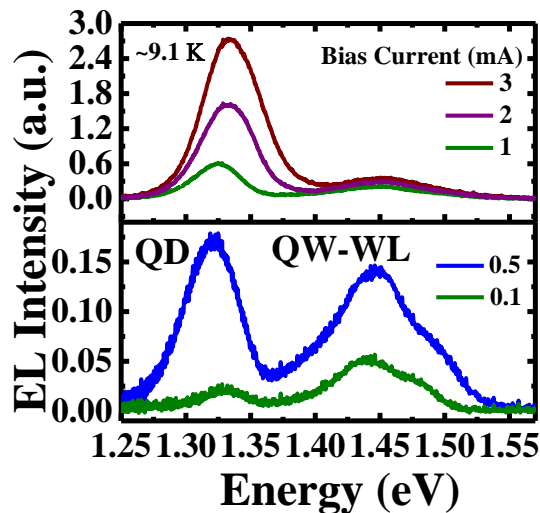


*Fig. 3.13 EL spectra taken for the same sample A at different mesa. The spectral features are reproduced as higher QW-WL peak emission precedes at lower bias currents and eventually saturates at higher biases while QD peak increases exponentially.*

### 3.4 Experimental Results of sample B

As mentioned in section 3.2.1, sample B contains two DBR stacks on both sides of the active layers which includes QD embedded within a QW in a step-by-step structure. This structure is similar to vertical cavity surface emitting laser (VCSEL) (sample structure is described in section 3.2.1). In Fig. 3.14(a), EL spectra of sample B is plotted for similar bias ranges as sample A. The emission peaks are clearly sharp and well separated. The peak energies are same coming from QD and QW-WL. However, in the QW-WL emission band, there are two spectrally separated peak, most probably from QW and WL. The evolution of peak with increasing bias is similar to sample A indicating the presence of potential barrier at the interface

of QD and QW. The FWHM of QD peak is  $<30$  meV while FWHM for sample A is 42-28 meV. The presence of DBR structure which forms an optical cavity only allows selective photonic bands. This could result in significant narrowing of FWHM.

In Fig. 3.14(b), the EL spectra are taken for different temperatures at same constant current as sample A ( $\sim 2.2$  mA). The QD peak emission is detected up to  $\sim 300$  K while QW-WL only disappear after  $\sim 250$  K. This can be easily explained as sample B only has three layers of QD-QW and carrier density is higher for the same current as compared to sample A which has six layers.

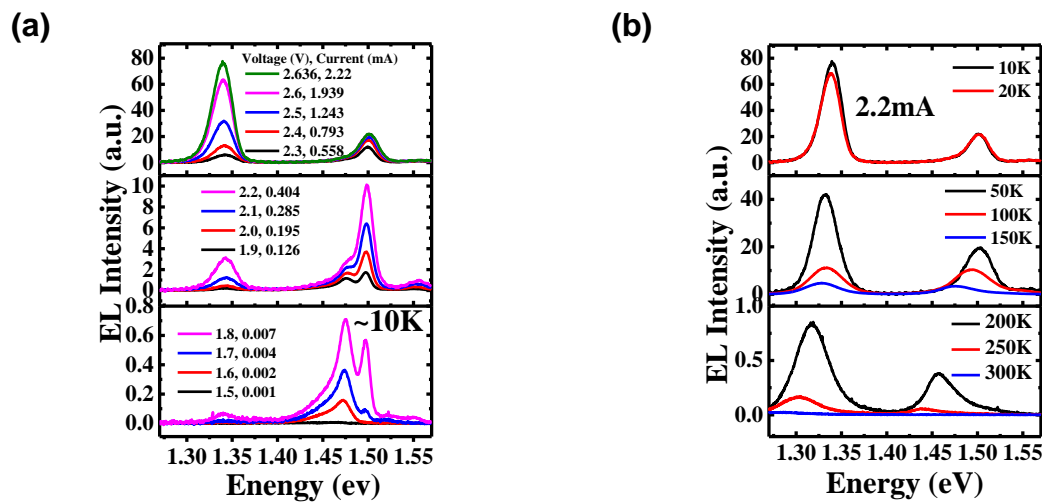


**Fig. 3.14** Sample B (a) EL spectra at different bias currents at constant temperature of  $\sim 10$  K. The corresponding voltage are also shown separated by comma. (b) EL spectra at constant current bias of  $\sim 2.2$  mA at different temperatures. The spectral peaks are sharp as compared to sample A.

### 3.5 Conclusion

In conclusion, we investigated a QD-QW heterostructure through the study of EL. The heterostructure has step-like potential for extra confinement of carriers which is expected to improve the yield of device but it gets affected by high density processes. We investigated the role of a potential barrier in the dynamics of charge carrier in QD-QW heterostructure and its impact on subsequent luminescence. This barrier is effective in low current regime ( $< 1$  mA) and it can influence the performance of low threshold LED or LD. We calculated an empirical mathematical formula to quantify the effect of such potential barrier. As current increased over

1 mA, the power exponent of integrated EL shows presence of biexcitons and trions in QDs. The temperature dependent EL shows the major reason for EL quenching is thermal escape of charge carrier.

The extra quantum confinement of QDs within the QW allows higher density of carrier accumulations inside the QDs as compared to QW. The study of temporal coherence shows the decline of coherence with increasing injection current in QDs. We argue that AR is major source of loss of coherence QDs. With increasing temperatures, due to the escape of carriers from QDs, the charge density reduces resulting in reduced ARs at a fixed bias current. These reduced ARs then further enhance the temporal coherence of light emission. Therefore, depopulation of carriers from QDs results in lower EL, but with improved optical coherence at higher temperatures. Therefore, we argue that spectrally resolved temporal coherence study can be a sensitive tool to detect the presence of ARs in such QD based light emitting devices. Also, from the applications point of view, study of optical coherence can help to achieve a dynamic balance between intensity and coherence of light in these quantum devices.

Additionally, as explained in section 1.2.2, the Auger recombination is still an ongoing study where various theoretical models are proposed to explain different empirical results. Similarly, we also require further theoretical and experimental investigations to enquire the relation between coherence and Auger recombination depending on the choice of materials and on particular heterostructures. The Auger recombination is predominantly studied on GaN and CdSe(CdS) materials, and coherence measurement on these materials can further reveal the relation between the two processes.

# Chapter 4

## Dual measurement of temporal and spatial coherence of light using a single experimental setup

### 4.1 Introduction

We have already mentioned the detailed theory of coherence and its applications in chapter 2. In the last chapter, the basic measurement of temporal coherence could detect the presence of Auger recombination in a quantum heterostructure. Therefore, a more elaborated work is required on detection tools and techniques of coherence. In this chapter, we will discuss the development of a modified Michelson interferometer and fringe analysis methods to measure spatial and temporal coherence using a single setup. Optical coherence is the basic concept behind optical interferometry and this technique is widely used in many fields of science and engineering. To begin with, Michelson and Morley<sup>137</sup> used it to detect the hypothetical ether. Young's double slit interferometer was used to prove the wave nature of light. And, the same experiment also demonstrated the dual nature of particles (say) electrons<sup>54,138</sup>. Recently, 'Laser Interferometer Gravitational-Wave Observatory' (LIGO) used it to detect gravitation waves. Apart from these famous experimental investigations, optical interferometry is used in quantum optics<sup>53</sup>, holography<sup>139</sup>, optical communication<sup>140</sup>, surface topography<sup>141</sup>, astronomy<sup>142</sup>, biology<sup>143</sup> etc. In the field of condensed matter, many-body cooperative phenomenon in light-matter interactions like excitonic<sup>34-37</sup> and polaritonic<sup>38-43,144</sup> lasing, Bose-Einstein condensation (BEC) of exciton<sup>145-147</sup>, polariton<sup>6,148</sup> and even photon<sup>149,150</sup> require interferometry to study the physics of optical coherence. Any light emitted from such condensate states show sharp increase in temporal and spatial coherence as the condensation thresholds are approached. These macroscopically large, coherent states are achievable up to room temperature due to the very low mass of these quasi-particle (say exciton) as compared to atomic systems (say Rb atoms). These can become a prominent candidates for quantum computation and communication<sup>151</sup> once such states can be coherently controlled in experiments. Therefore, a spatio-temporal study becomes crucial and there is a need to make a

single compact setup to investigate both kinds of coherences for a rigorous investigation. Here, we present an experimental setup based on Michelson interferometer to investigate both types of coherence in a single setup. We surveyed as well as adapted some earlier methods where attempt were made to design such single experimental setups and understood that some key points are overlooked in all of those. For example, a major issue of measurement of inter mixing of spatio-temporal coherence has never been dealt with. Subsequently, we developed a ‘temporal filtering’ method to resolve this kind of inter mixing. There are two parts to any optical coherence measurement set up - one is to provide necessary temporal or spatial delay between the two interfering optical fields and the second is to measure the resulting interference pattern. In this chapter, we first explain how the modified experimental setup is designed and then how the data is acquired and analysed to estimate the first order correlations. This estimation method is common to both the coherence measurements. Then, we will individually explain how temporal and spatial ‘purity’ of coherences were monitored and controlled in our modified instrument. This chapter is divided in to seven sections where we start, after the introduction, with experimental setup in 4.2. In this section, there are subsections to explain each part of instrument in details. In 4.3 and section 4.4, we explain common data acquisition and analysis methods to estimate first order correlation as coherence. In section 4.5, we describe how the usual temporal delay is introduced and also discuss the curve overlap technique for effective range extension of any instrument. In 4.6, we explain spatial coherence measurement with the modified Michelson interferometer and describe the ‘temporal filtering’ method. In section 4.7, the conclusion is presented.

## 4.2 Experimental setup

The basic design of our experimental setup is fundamentally based on Michelson interferometer. The amplitude of source light is divided by a beam splitter and two replicas of the same light are created. These two light beams can be separated in time as well as in space to see the effect of temporal and spatial coherence in the optical interference pattern. The schematic diagram of our experimental setup is given in Fig. 4.1(a). In our experiment, we use two retro-reflectors ( $M_1$  and  $M_2$ ), procured from Holmarc, India and a non-polarizing CCM1-BS013/M beam splitter from Thorlabs. Retroreflector  $M_1$  is attached to a piezo actuator PAS005 (Thorlabs) and this ‘piezo +  $M_1$ ’ combination is mounted on kinematic-mount which provides the retroreflector the freedom to tilt vertically and horizontally. This mount is installed on a linear stage which can move in the lateral direction (marked as double sided arrow 1 in

Fig. 4.1(a)). The least count of this stage is  $10\ \mu\text{m}$  and it can move up to  $25\ \text{mm}$ . Similarly, the retroreflector  $M_2$  is mounted on kinematic-mount and a linear stage. The movement of this stage is in longitudinal direction (marked as double sided arrow 2 in Fig. 4.1(a)).

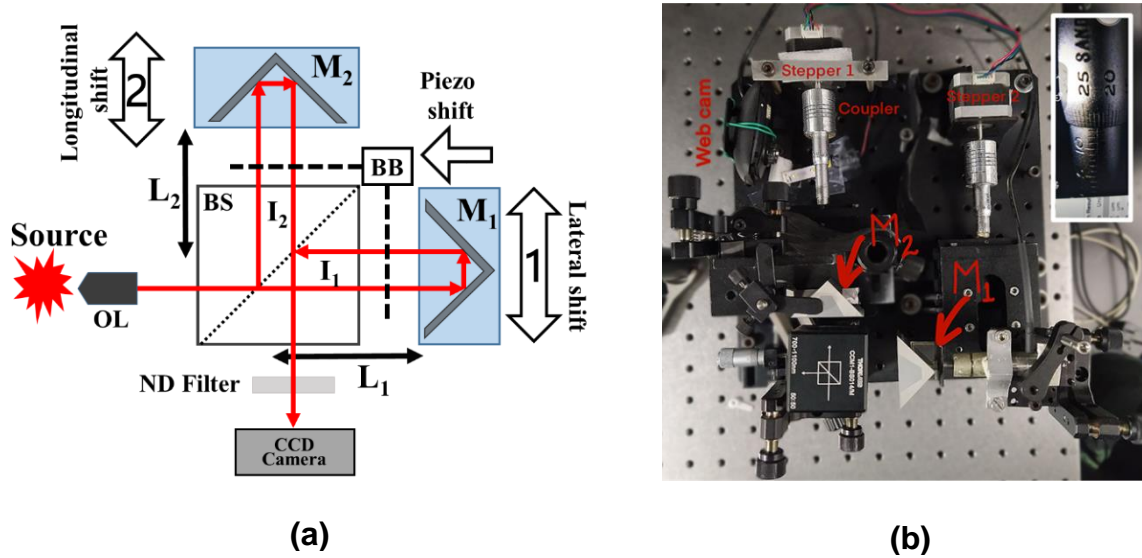


**Fig. 4.1** (a) Schematics of experimental setup.  $M_1$  and  $M_2$  are two retro-reflector which are  $L_1$  and  $L_2$  distance away from centre of beam splitter (BS). The direction of movement of retroreflectors are show by two sided arrows marked as 1 and 2. Light source is collimated by objective lens (OL) and beam intensity is captured by CCD camera which has neutral density (ND) filter in front of it. Over BS, there is beam blocker (BB) to close the path of light at each arm of interferometer. (b) Image of the setup. Retroreflector  $M_1$  and  $M_2$  are installed on linear manual stages. To move the stages, two stepper motors are coupled to rotating screw-head of stages with customized flexible coupler. The position of stage coupled to stepper 1 is observed through a webcam fitted to the side of stage by noticing the scale marks on the screw of stage. Camera output is shown in inset.

We used AlGaInP based multi-quantum well commercial laser diode (LD) HL6358MG (Thorlabs) as a source which has emission wavelength at  $639\ \text{nm}$  and lasing threshold  $\sim 30\ \text{mA}$  current. Emission below threshold current is in a non-lasing mode and the sample works as a simple LED. We used this LD at current input of  $1\ \text{mA}$ , one order of magnitude below threshold to have a source of low coherence since we are interested in making a setup which can also measure low and variable coherence of light source. The bias to LD is provided by ITC4001



Controller (Thorlabs). An objective lens (magnification 10×) is placed in front of LD to make collimated beam.

### 4.2.1 LabVIEW controlled CCD Camera

The collimated source beam went through beam splitter and reflected back from the two faces of retroreflector to meet at CCD sensor of BC106N-VIS/M beam profiler (Thorlabs). This CCD sensor has  $1360 \times 1024$  pixels and sensor area is  $\sim 8.77 \times 6.60 \text{ mm}^2$ . The CCD is controlled through LabVIEW interface where automated control to the camera parameters and output intensity is achieved. In the provided application (with CCD), as shown in Fig. 4.2(a), intensity could be saved over only two pixel lines with manual commands. Therefore, we

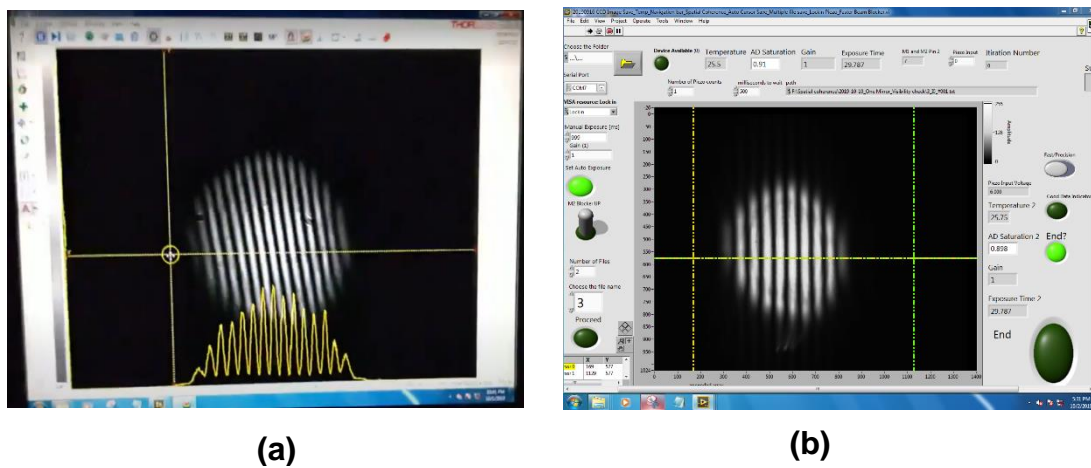


**Fig. 4.2** (a) The provided CCD computer application software showing interference pattern and intensity profile (yellow fringes) along one horizontal axis. (b) LabVIEW interface to save 2D-array of output image.

created a LabVIEW interface where we could save the whole 2D screen in terms of pixel numbers. These numbers later converted to actual distance by conversion factor of  $6.45 \mu\text{m}$  (pixel size) and screen coordinates of camera are called X-Y coordinates. In front of the CCD, we used neutral density filters from Newport to attenuate light by 0.3 dB to 4 dB to protect camera against any intense light and subsequent overload or damage.

### 4.2.2 Beam blocker

On top of the beam splitter, we installed a beam blocker which is made to block either of the beams going to  $M_1$  or  $M_2$ . It is made of two servo motors (SG90) and two opaque sheets

attached to their shaft (shown in Fig. 4.3(a)). In the schematic diagram in Fig 4.3(b), the beam blocker is shown to block beam going to  $M_1$  retroreflector and only allowing beam from  $M_2$  retroreflector. We used Arduino microprocessor and driver ICs to operate stepper and servo motors. In Fig. 4.3(c) and (d) the circuits of servo and stepper motor are provided.

### 4.2.3 Piezo driver

As mentioned above, the  $M_1$  is attached to a piezo and this piezo requires a power supply to provide specific voltage for piezo movement. We made a cost-effective piezo driver

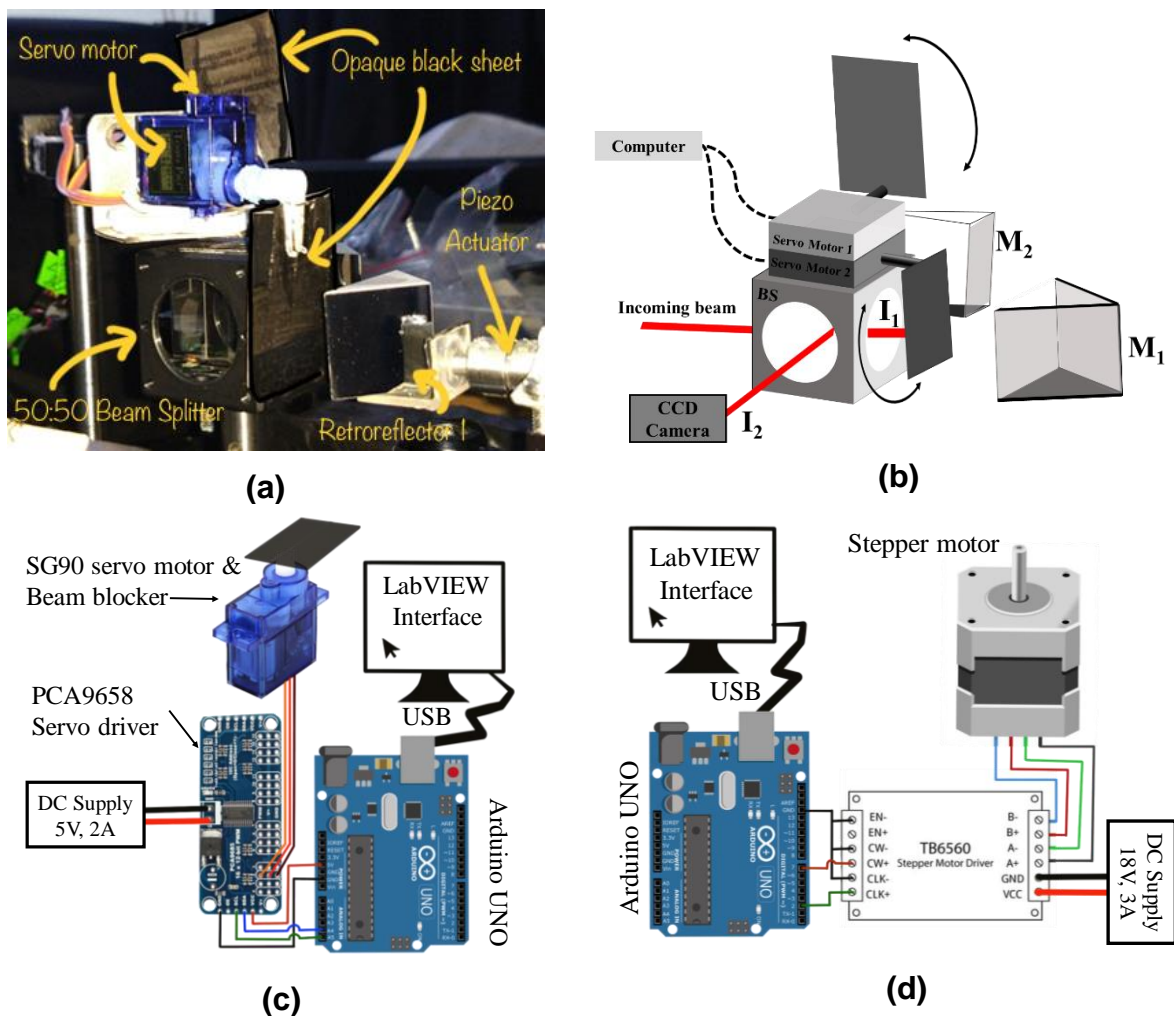


**Fig. 4.3** (a) Image of beam blocker over beam splitter. (b) Schematic of beam blocker. (c) The electronic circuits for the servo and (d) the stepper motor.

with high voltage-high current op-amp IC. The circuit is simple Op-amp based amplifier in

non-inverting mode. Op-amp IC (3583JM) was procured from Burr-Brown. The common collector DC voltage ( $V_{cc} = 70 \text{ V DC}$ ) is provided with a lab built AC-to-DC converter. In Fig.

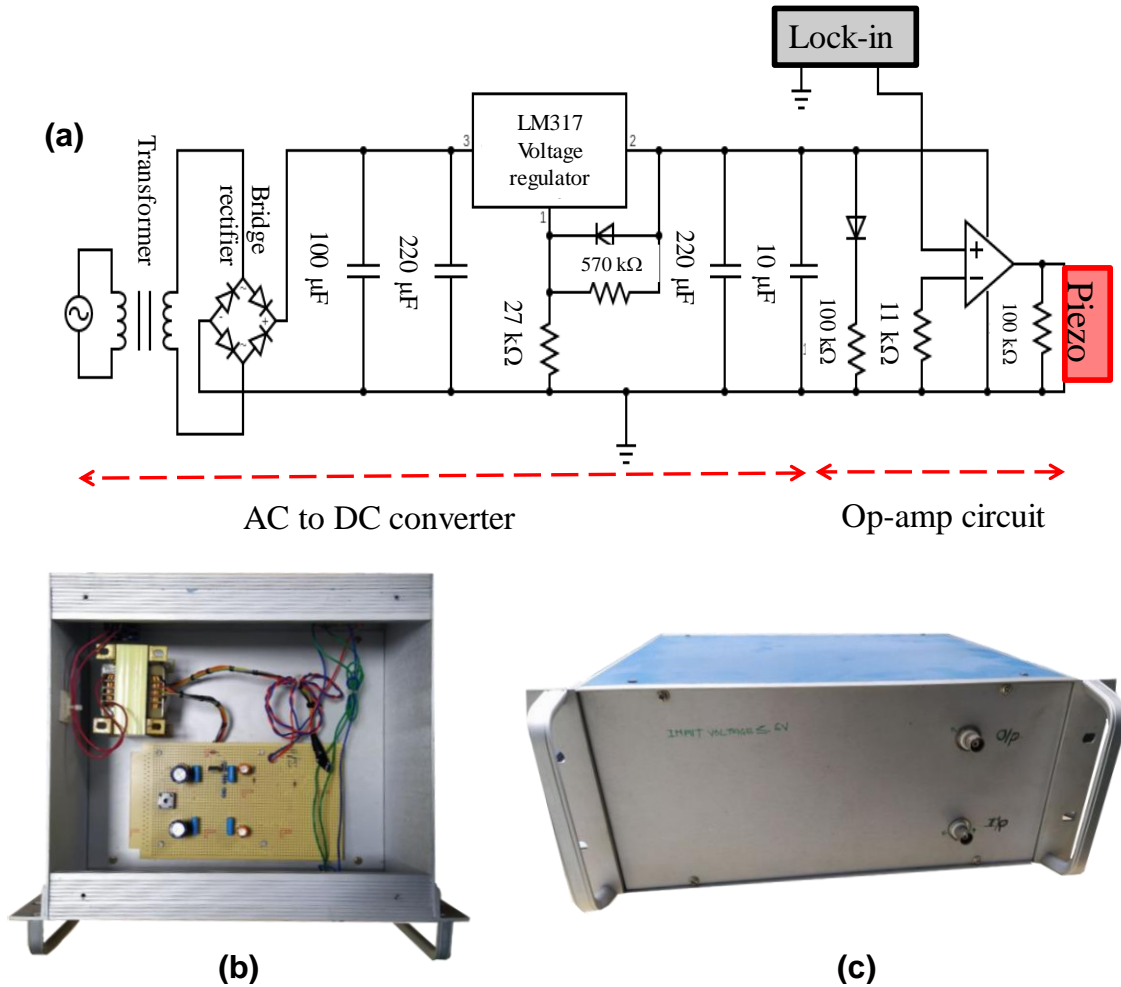


**Fig. 4.4** (a) Circuit diagram of piezo driver. The circuit works as a voltage amplifier with amplification value of  $\sim 10$ . The input voltage is provided with lock-in amplifier auxiliary output and amplified voltages are fed to piezo actuator. Red dashed line shows the separation between DC converter circuit (left) and Op-amp IC circuit (right). (b) and (c) are images of piezo driver electronic setup.

4.4(a) left to the red dashed line shows the circuit diagram of DC converter. Right to the dashed line shows the Op-amp configuration in non-inverting mode. The gain in non-inverting mode is

$$Gain = 1 + \frac{R_f}{R_i} \quad (4.1)$$

where  $R_f$  feedback resistor and  $R_i$  in input register. The value used for  $R_i$  and  $R_f$  are  $11\text{k}\Omega$  and  $100\text{k}\Omega$ , respectively resulting in gain of 10.09. After assembling the piezo driver, the system is calibrated with He-Ne gas laser ( $\lambda = 633\text{ nm}$ ) as light source on the same setup shown in Fig. 4.1(a). Laser is highly monochromatic source and appropriate for such calibrations. A plano-convex lens ( $f = 100\text{ mm}$ ) is put in front of the laser to make a beam of slightly curved wave front. The radially symmetric curved wave fronts are able to produce circular fringe pattern

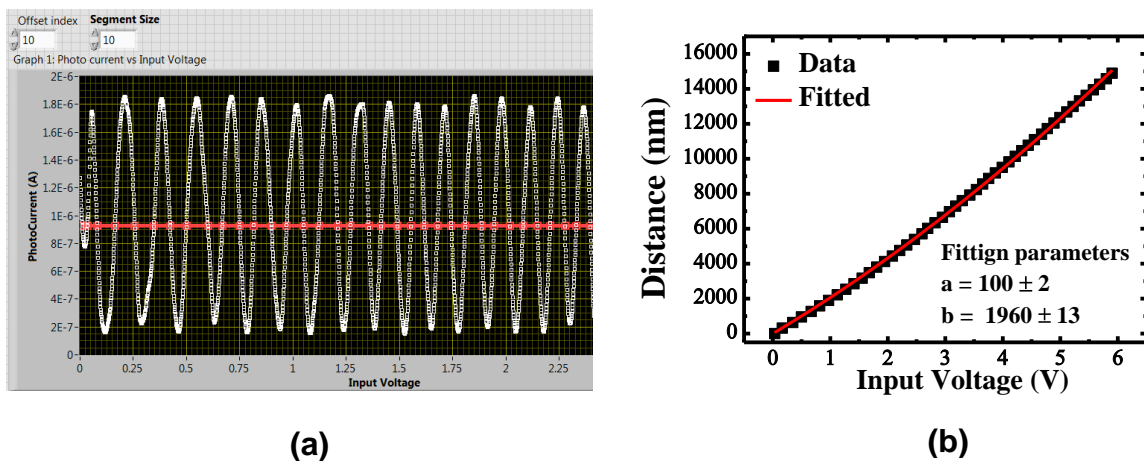


**Fig 4.5** (a) Fringe oscillation vs input voltage of lock-in auxiliary to piezo driver. (b) The distance vs input voltage plot of one of the experiments. This data is extracted from fringe oscillations.

when both beams of interferometer are in overlapping condition. A small slit hole of about  $1 \times 1\text{ mm}$  create by putting two linear slits perpendicular to each other. Central part of fringe pattern is allowed to go through the slit hole to fall on Silicon photodiode (FDS0010, Thorlabs). The photodiode is provided 5 V in reverse bias through Keithley source meter and photocurrent is recorded. As the input voltage is provided by lock-in amplifier's auxiliary output in steps of 0.001 V, the piezo started to move leading to fringe movement. The movement of piezo  $\lambda/2$  will produce one complete cycles of the fringe and one complete cycle of photo current because optical path is twice the physical path in Michelson type interferometers. The fringe oscillations are recorded for 0 to 6 V and only a portion of that record is shown in Fig. 4.5(a) to clearly visualize the oscillations. The fringe analysis is done with an algorithm written in LabVIEW which produces a line intersecting with oscillation curve at a specific photocurrent. The input voltage at these intersecting points are taken sequentially and alternative points (a full cycle of oscillation) are selected to mark the shift the piezo by  $\lambda/2$ . Alternate points, separated by piezo

shift of  $\lambda/2$ , are plotted as input voltages against the integer multiple of  $\lambda/2$  (nm) as shown in Fig. 4.5(b). The wavelength distance vs input voltage is fitted with a quadratic formula as given in Eq. (4.2) to find a relation between distances moved by piezo and input voltage.

$$Distance(nm) = aV^2 + bV \quad (4.2)$$

where  $V$  is input voltage in volts. The same experiment is repeated 33 times and these 33 values of parameters ‘ $a$ ’ and ‘ $b$ ’ are taken for statistical averaging. The averaged values are given in Table 4.1. The final equation of calibration for piezo is

$$Distance(nm) = 120V^2 + 2004V \quad (4.3)$$

The piezo movement is not linear with respect to input voltage. The minimum and maximum distances by piezo are calculated to be 303 nm and 514 nm, respectively. During the experiment, we provided lock-in voltage in step of 0.15 V from 0 to 6 V in 40 steps and piezo moved by  $\sim 16 \mu\text{m}$ . All the optical components and stages are compactly assembled on single  $25 \text{ cm} \times 25 \text{ cm}$  optical breadboard as shown in Fig. 4.1(b). The initial alignment of the setup is done by He-Ne gas laser. The experiment is done on an ultra-low vibration optical table to avoid noise in interference pattern due to any surrounding vibrations.

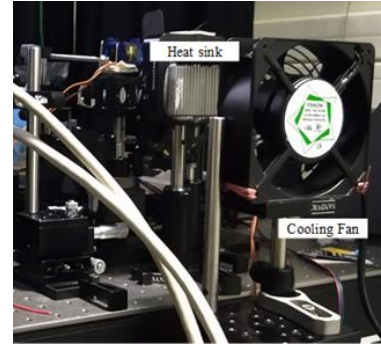
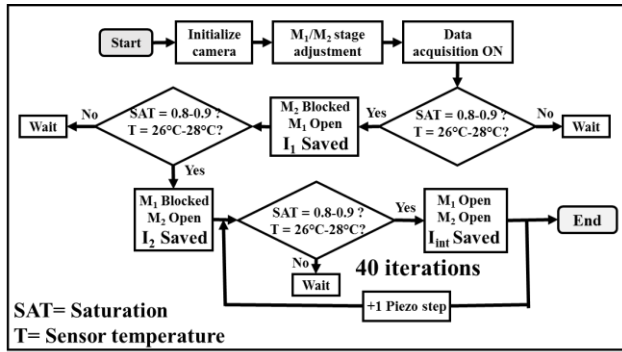
<b>Table 4.1</b> Fitting parameter of Eq. 4.2 of piezo calibration	
Parameter	Value
$a$	$120 \pm 7 \text{ nmV}^{-2}$
$b$	$2004 \pm 136 \text{ nmV}^{-1}$

### 4.3 Data acquisition

After the above mentioned description of experimental setup, in this section we explain how interference data is taken using this modified instrument without invoking the idea of temporal or spatial coherence in the first place because this method is common to both measurements. Therefore, correlation function is denoted as simple  $|g^{(1)}|$  in this section. As discussed in Chapter 2, the knowledge of individual intensity ( $I_1$  and  $I_2$ ) and interference ( $I_{int}$ ) is required to estimate the correlation function  $|g^{(1)}|$  through interference equation,

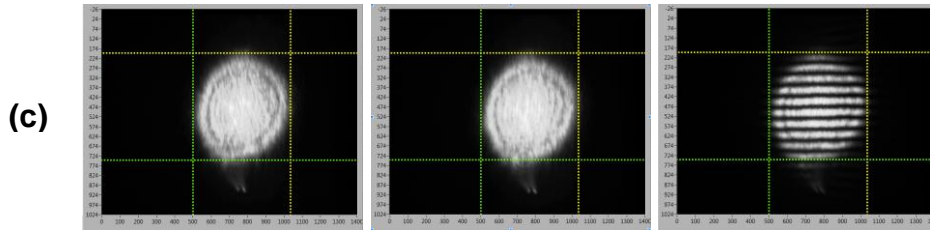
$$I_{int} = I_1 + I_2 + 2|g^{(1)}|\sqrt{I_1 I_2} \cos(\varnothing) \quad (4.4)$$

where  $\varnothing$  is phase between two interfering fields. With beam blocker, all three intensities could be put on CCD, one by one. We used our home-built LabVIEW interface to collect the 2D-array ( $1360 \times 1024$ ) of the images of these beams. CCD parameters such as gain (G), exposure-time (ET), saturation (SAT) and sensor temperature (T) simultaneously are also recorded for each 2D image. The CCD is used in auto-exposure mode which keeps the optimum values of



(a)

(b)



(c)

**Fig. 4.6** (a) Flow-chart of data acquisition method used in the experiment. Saturation value (SAT), and sensor temperature (T) of camera are kept in narrow range of 0.8-0.9 and  $26^\circ\text{C}$ - $28^\circ\text{C}$ , respectively. For each step of stage  $M_1$  (or  $M_2$  for the case of spatial correlation measurement),  $I_1$  and  $I_1$  are saved and 40 images of  $I_{int}$  are saved for 40 steps of piezo. (b) A heat sink attached to body of CCD through thermal paste and a cooling fan is placed outside the floating optical-table in front of heat sink. The fan is kept off during the measurement and only run when CCD temperature gets higher than  $28^\circ\text{C}$ . (c) The image  $I_1$   $I_2$  and  $I_{int}$  on CCD screen and four cursor lines are used to make to mark the position of each beam spot.

G and ET depending upon the intensity of incoming light. CCD automatically tries to keep saturation value from 0.8 to 0.9 indicating no overloads or saturation has occurred. However, the sudden change in intensity can result in instant overload and it takes some attempts for

CCD to adjust again. With operation time, air-cooled CCD sensor used in our experiments are heated up and that results in the offsets in the recorded image data. Therefore, data taken at substantially different values of these sensor temperatures have different offsets and initially lead to incorrect results. In our interface, we set conditions over saturation value and sensor temperature for 2D images to be recorded. An additional heat sink and air flow system is attached to CCD to keep the temperature range (shown in Fig. 4.6(b)). Flow-chart for data acquisition is given in Fig. 4.6(a). First, we turn on the Laser diode in LED mode and initialize the CCD camera. Depending upon the experiment (temporal or spatial) we adjusted  $M_1$  and  $M_2$  stages and kinematic mounts. Then, we saved images of  $I_1$ ,  $I_2$  and  $I_{int}$  by using beam blocker. 2D image of  $I_{int}$  could be saved for 40 values of piezo steps in a single run keeping the conditions of saturation and sensor temperature. The image of one such  $I_1$ ,  $I_2$  and  $I_{int}$  is shown in Fig. 4.6(c).

#### 4.4 Data Analysis Method

After recording the individual intensities as well as the interference pattern ( $I_1$ ,  $I_2$  and  $I_{int}$ ), the next objective is to estimate the first order correlation as  $|g^{(1)}|$ . We normalized the 2D array by dividing it with their corresponding G and ET values to put these arrays on single scale of intensity

$$\text{Corrected 2D array} = \text{Camera output 2D array} / (G \times ET) \quad (4.5)$$

From the 2D image of  $I_{int}$ , one axis is chosen to extract the 1D data. One such image is given in Fig. 4.7(a) and chosen axis is indicated by the  $\sigma$ -axis at the centre of  $I_{int}$  by black dashed line. X-Y axes are CCD sensor coordinates along horizontal and vertical direction. We chose the  $\sigma$ -axis along Y-axis throughout our experiment for uniformity of measurement. The intensity values over this axis is extracted from images of  $I_1$ ,  $I_2$  and  $I_{int}$  as  $I_1(\sigma)$ ,  $I_2(\sigma)$  and  $I_{int}(\sigma)$  as shown in Fig. 4.7(b). We took 10 more pixels on either side of  $\sigma$ -axis for averaging to avoid any pixel related error. To estimate  $|g^{(1)}|$  from these data, we rearrange Eq. (4.4),

$$\frac{I_{int}(\sigma) - I_1(\sigma) - I_2(\sigma)}{(2)\sqrt{I_1(\sigma) * I_2(\sigma)}} = |g^{(1)}| \cos(k_\sigma \cdot \sigma - \varphi) \equiv S(\sigma) \quad (4.6)$$

Here  $S(\sigma)$  is evaluated by using intensities of  $I_{int}(\sigma)$ ,  $I_1(\sigma)$  and  $I_2(\sigma)$ . If all intensities are corrected by normalization process (mentioned above),  $S(\sigma)$  should simulate a cosine function

whose amplitude gives the value of  $|g^{(1)}|$ . Here  $\phi = k_\sigma \sigma = (\vec{k}_1 - \vec{k}_2) \cdot \vec{\sigma} + \varphi$  where  $\vec{k}_1$  and  $\vec{k}_2$  are wave vectors of two interfering fields,  $(\vec{k}_1 - \vec{k}_2) \cdot \hat{\sigma} = k_\sigma$  and  $\varphi$  is constant phase factor. The  $S(\sigma)$  is estimated for  $I_{int}$ ,  $I_1$  and  $I_2$  of Fig. 4.7(b) and is shown in Fig. 4.7(c). Now, there are effects of dark currents due to CCD and other electronics, and  $|g^{(1)}|$  is strictly a positive ( $0 \leq |g^{(1)}| \leq 1$ ) quantity. Therefore, we fitted  $S(\sigma)$  as

$$\text{Fitting function } S(\sigma) = S_0 + \exp(b) \cos((\sigma - \sigma_0)/d) \quad (4.7)$$

where  $|g^{(1)}| = \exp(b)$  fulfills the condition of  $|g^{(1)}| > 0$  and  $S_0$  is an offset which shows the effect of dark currents or systematic error in the calculation of  $|g^{(1)}|$ .  $\sigma_0$  and  $d$  depends upon values of  $k_\sigma$  and  $\varphi$ . The fitting of this equation generates a  $4 \times 4$  covariance matrix where the square root of diagonal elements provides the standard error of fitting parameters. The standard error of  $\exp(b)$  is multiplied to the student t-inverse cumulative distribution function to get 95% confidence interval.

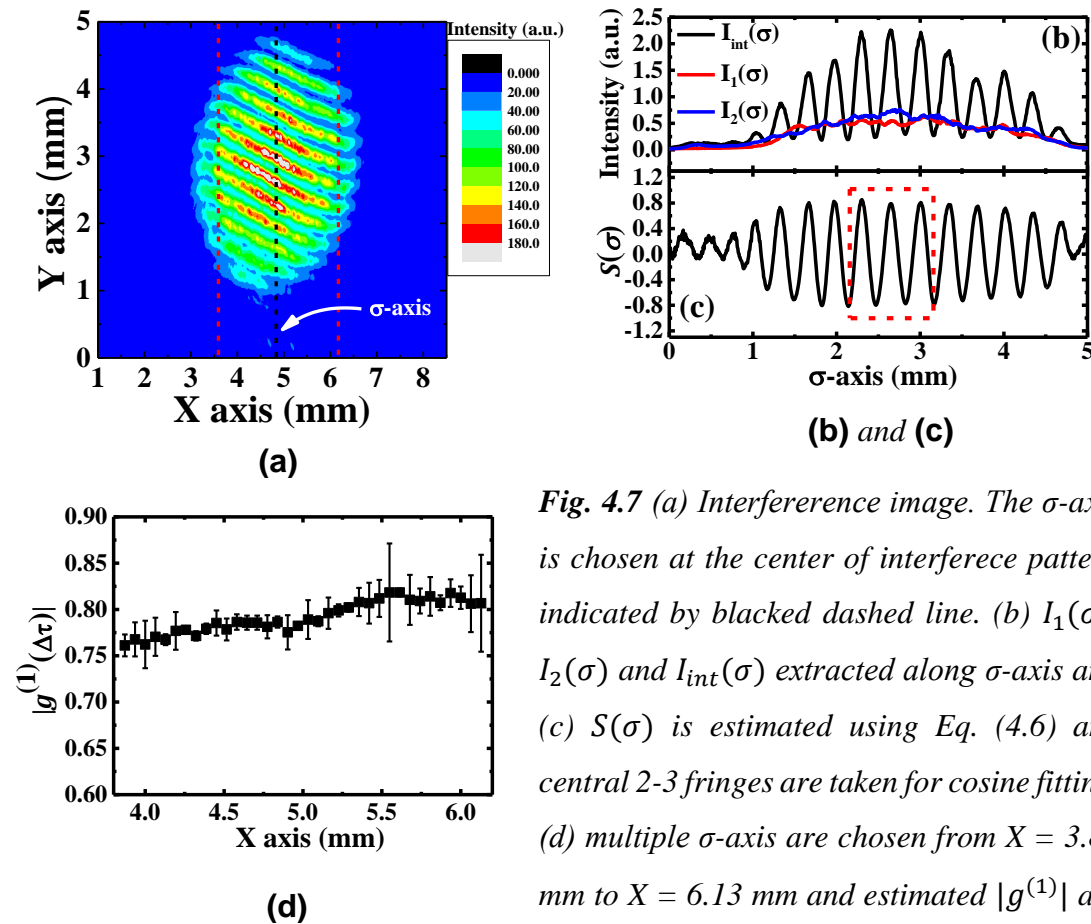


*Fig. 4.7 (a) Interference image. The  $\sigma$ -axis is chosen at the center of interference pattern indicated by black dashed line. (b)  $I_1(\sigma)$ ,  $I_2(\sigma)$  and  $I_{int}(\sigma)$  extracted along  $\sigma$ -axis and (c)  $S(\sigma)$  is estimated using Eq. (4.6) and central 2-3 fringes are taken for cosine fitting. (d) multiple  $\sigma$ -axis are chosen from  $X = 3.87$  mm to  $X = 6.13$  mm and estimated  $|g^{(1)}|$  are plotted in (d).*



In the initial experiments, we noticed high value of offset  $S_0$ , almost comparable to  $|g^{(1)}|$  when CCD sensor temperature was not monitored. After narrowing the temperature range,  $S_0$  reduced sufficiently low compared to  $|g^{(1)}|$  values. Moreover, the choice of  $\sigma$ -axis is manual and it is prone to random error; therefore, we selected a range of  $\sigma$ -axes to see the variation of  $|g^{(1)}|$ . On Fig. 4.7(a), from CCD sensor coordinate axis  $X = 3.87$  mm to  $X = 6.13$  mm (as shown by red dashed lines), different  $\sigma$ -axis with separation of  $\sim 0.06$  mm (10 pixels) are chosen to estimate  $|g^{(1)}|$ . Here, we did not take pixel average. These  $|g^{(1)}|$  are plotted in Fig. 4.7(d) with offset  $S_0$  as error bar to compare the value of  $|g^{(1)}|$  with corresponding  $S_0$ . The mean value of all the  $|g^{(1)}|$  is 0.79 and the standard error is 0.01.  $S_0$  is noticeably smaller than  $|g^{(1)}|$  and minute deviation in choice of  $\sigma$ -axis did not affect the  $|g^{(1)}|$  results. Hence, the methods adopted for data acquisition and analyses are robust against small variations of selection of  $\sigma$ -axis.

## 4.5 Temporal coherence measurement

So far, we have discussed the method of acquisition of  $I_1$ ,  $I_2$  and  $I_{int}$  and calculation of  $|g^{(1)}|$ . To measure temporal coherence, we are required to provide a time delay between two beams ( $I_1$  and  $I_2$ ) without involving any  $\Delta r$ , and then measure  $|g^{(1)}(\Delta\tau)|$ . The schematics of

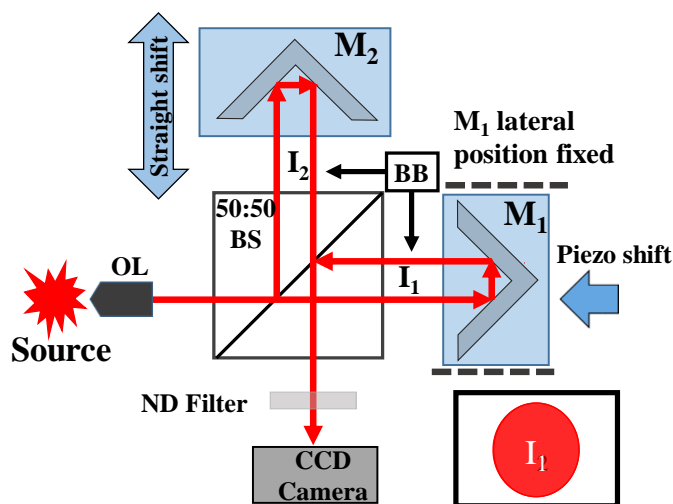


*Fig. 4.8 The schematics of setup used for temporal correlation measurement. The retroreflector  $M_1$  is fixed at a position where  $I_1$  and  $I_2$  beam spot on CCD are at complete overlap condition as shown in the inset.*

setup used for temporal delay is shown in Fig. 4.8. The  $M_2$  retroreflector could move in longitudinal direction leading to path difference of  $\Delta L = L_1 - L_2$  which is equal to temporal delay of ( $\Delta\tau = 2\Delta L/c$ ). The piezo attached to  $M_1$  is also moved in longitudinal direction to

provide fine  $\Delta\tau_p$ . The  $\Delta\tau_p$  (with subscript ‘p’) is specifically used to indicate piezo related time delay while  $\Delta\tau$  is for any general time delay. Moreover, lateral movement of  $M_1$  is fixed at a position where  $I_1$  and  $I_2$  beams are in complete overlap leading to  $\Delta r \sim 0$ .

The condition of complete overlap of two beams is assured by four cursor lines on the CCD output screen (see Fig. 4.6(c)). The position of  $I_2$  and  $I_1$  is controlled by kinematic mounts and lateral movement of  $M_1$ . The stage of  $M_2$  if moved by  $10\mu\text{m}$  provides temporal delay of  $\sim 66$  fs and piezo of  $M_1$  moved up to  $\sim 108$  fs in 40 steps (see section 4.2.3). These two

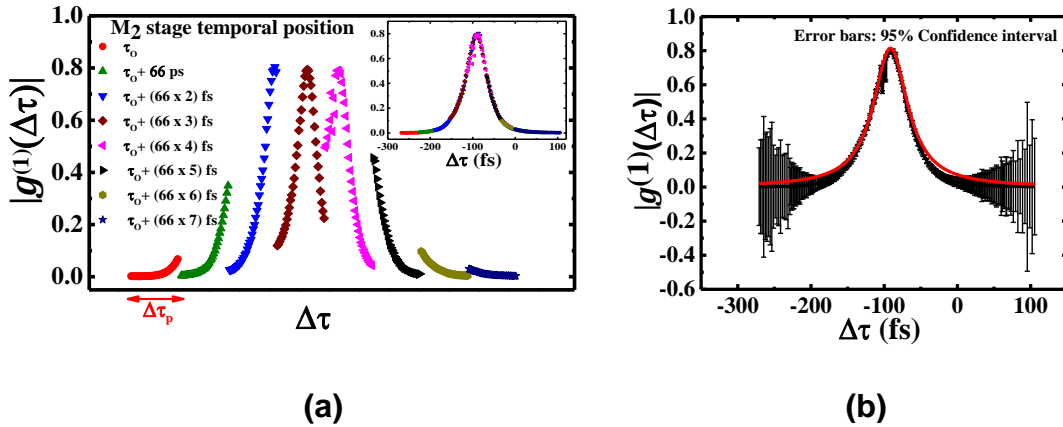


**Fig. 4.9** (a) Individual curve show estimated values of  $|g^{(1)}(\Delta\tau_p)|$  and while different curve show  $M_2$  stage temporal position. The red arrow on  $\Delta\tau$  scale shows the plot of one  $|g^{(1)}(\Delta\tau_p)|$ . Plots of different  $M_2$  stage are manually segregated along the  $\Delta\tau$  axis for clarity. Therefore, scale marker along  $\Delta\tau$  are not given. Inset of (a) show different curves translated on  $\Delta\tau$  scale to make a single curve. (b) The different  $|g^{(1)}(\Delta\tau_p)|$  are translated by using algorithm shown in Eq. (4.8) into a single curve.

instruments independently provided coarse and fine temporal delays. We followed the acquisition algorithm mentioned in section 4.3 and 40 values of  $|g^{(1)}(\Delta\tau_p)|$  calculated by piezo, then linear stage is moved by  $10\mu\text{m}$  and process of piezo acquisition is repeated. The result is shown in Fig. 4.9(a) where each curve (black, red, green, blue etc.) contains 40 data points corresponding to 40 steps of piezo and each consecutive curve is at the next step of linear stage. We see a significant overlap between consecutive curves because piezo range ( $\sim 108$  fs) is greater than the step of stage ( $\sim 66$  fs). We translated these curves in  $\Delta\tau$  axis to the condition of ‘good’ overlap’ and results are shown in the inset of Fig 4.9(a). If piezo range is to be exactly equal to linear stage step, the manual translation of these different curves into a single curve

would be difficult in the absence of any criteria and precision of instrument would be compromised. The better method is extend the range of piezo and use numerical analysis to translate the curves into one single curve. We used an algorithm to minimize the difference between overlapping points of two curve to find the optimum value of translation.

$$\Delta g = \frac{\sum_i \{(g_n^{(1)})_i(\Delta\tau) - (g_{n+1}^{(1)})_i(\Delta\tau \pm t)\}}{\sum_i} \quad (4.8)$$

where  $i$  = number of overlapping point in curve.  $(g_{n+1}^{(1)})_i$  are points of  $(n + 1)th$  curve of  $M_2$  stage which overlap with adjacent  $(n)th$  curve. The  $(n + 1)th$  curve is translated in  $\Delta\tau$  by the unit of  $t = N \times (\text{minimum step of piezo})$  where  $N = 1, 2, 3, \dots$ . The translated curves using above method are stitched together and complete curve is shown in Fig. 4.9(b). The benefit of the curve overlap method is that it extends the range of measurement while retaining the precision. We mentioned few physical phenomena in section 4.1 where coherence of the source changes and this curve overlap method can be very helpful to measure those changes in coherence. Moreover, good overlap also indicates good reproducibility and reliability of data. Each curve overlaps with two immediate adjacent curves on either side by  $\sim 60\%$  and two more adjacent curves by  $\sim 20\%$ . Any misaligned overlap would have suggested that either the source is not stable or there are changes due to movement of  $M_2$  stage. However, we see reasonably good extent of curve overlaps in inset of Fig. 4.9(a). This indicates that data is reproducible even after movements of linear stage  $M_2$  and the beam alignment is maintained to fulfil the condition of total beam overlap. These matching overlaps further validate our instrumentation and the method of analysis as mentioned above. The error bars in Fig. 4.9(b) is 95% confidence interval calculated with the method mentioned in section 4.4. The curve is fitted with Lorentzian function

$$|g^{(1)}(\Delta\tau)| = g_0 + \frac{2(A)}{\pi} \left( \frac{w}{4(\Delta\tau - \Delta\tau_{center})^2 + w^2} \right) \quad (4.9)$$

where  $g_0 (\geq 0)$  is offset,  $w$  is FWHM,  $A$  is area and  $\Delta\tau_{center}$  is centre of curve on  $\Delta\tau$  axis.  $R_2$  value of fitting is 0.979. The values of fitting parameters are given in table 4.2. The approximated coherence ( $\tau_c$ ) of the source is FWHM of  $|g^{(1)}(\Delta\tau)|$  curve. The error of fitting of FWHM is only 1 fs. However we take highest piezo step as scale of error bar in measurement and estimated coherence time is  $57 \pm 3$  fs.

**Table 4.2** Lorentzian fitting parameter of Fig. 4.9(b)

Fitting parameter	Value
$g_0$	0 (with condition of $g_0 \geq 0$ )
$\Delta\tau_{center}$	-91
$A$	73 fs <sup>2</sup>
$w$	57 fs

Next, to check the validity of our measurement, we used Wiener-Khinchin theorem to calculate the coherence time. We measured the power spectra of source at 1 mA and took its Fourier transform. And, the FWHM of Fourier transformed curve is  $\sim 62$  fs. Two independent measurements estimating similar values of  $\tau_c$  validates the functionality of our instrument.

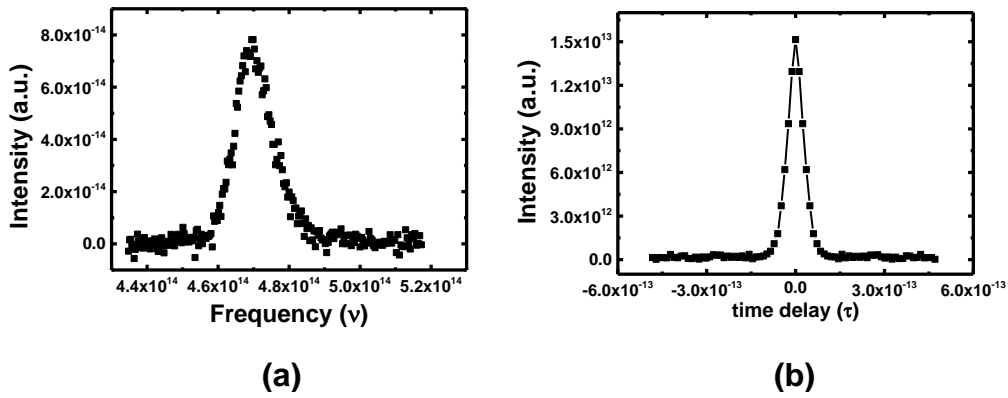


**Fig. 4.10** (a) Normalized power spectra of source at 1 mA bias current. (b) Normalized Fourier transform of power spectra.

## 4.6 Spatial coherence measurement

In the modified Michelson Interferometer, by the lateral movement of  $M_1$ ,  $I_1$  and  $I_2$  beams can partially overlap on CCD. The overlapping parts of beam interfere based on their spatial correlation. The schematic of cross-section of the beam is drawn in Fig. 4.11 (left). Pairs of exact dotted and dashed lines are separated by distance  $\Delta r$  (shown as red arrow). This same beam passes through beam splitter and after reflecting back from  $M_1$  and  $M_2$ , falls on CCD. If the separation between two beam ( $I_1$  and  $I_2$ ) is  $\Delta r$ , the parts of beam spot indicated by exact dot and dashed lines will be in complete overlap. This overlap is drawn in Fig. 4.11 (right).

This way, we are able to overlap those parts of same beam which are separated by  $\Delta r$ . The interference generated by these partial overlap is used to measure spatial coherence.

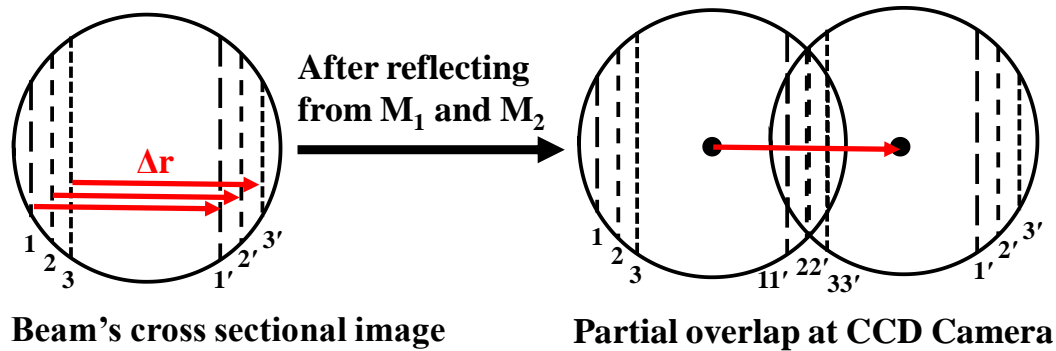


**Fig. 4.11** (Left) Schematic cross-sectional image of beam originating from objective lens. Identical dashed and dotted lines (1 and 1', 2 and 2', 3 and 3') are  $\Delta r$  distance apart in the same beam. (Right) Partially overlapping image of  $I_1$  and  $I_2$  after reflecting back from  $M_1$  and  $M_2$ . The beams are  $\Delta r$  distance apart and identical dashed and dotted lines overlap.

In all previous experiments, to achieve spatially shifted beams, either of the mirrors of interferometer are tilted or one of the beams is spatially inverted by using only one retroreflector. In these two approaches, an angle between two beams is introduced. The schematics of these two methods are given in Fig. 4.12(a) and (b). This angle between beams can lead to an unwanted temporal phase as shown in Fig. 4.12 (c). For a typical table-top interferometer having 10 cm of distance between screen and mirror, the angular tilt by  $1^\circ$  can result in  $\sim 15 \mu\text{m}$  ( $\Delta\tau \approx 50 \text{ fs}$ ) of path difference which is 24 times the  $\lambda$  used in our experiment and about the same length as measured coherence length of our source. The beam spot size in our case is 3 mm and to move it by 2 mm with above mirror to screen distance, the required angular tilt for mirror is  $>1^\circ$ . Therefore, it can be understood that such temporal involvements during spatial shift can lead to incorrect estimation of spatial coherence.

To avoid this, we use linear shift of beam instead of angular tilt to achieve partial overlap. We use setup whose schematic diagram is shown in Fig. 4.13(a). For partial overlap,  $I_1$  beam is shifted by laterally shifting the linear stage of  $M_1$  in direction as indicated by arrow 'Lateral shift'.  $M_2$  is locked in position of approximated  $\Delta\tau \sim 0$ . The lateral shift of  $M_1$  shifts the  $I_1$  beam without introducing any angle between beams, hence, it prevents any additional  $\Delta\tau$ . The simple trigonometric explanation is as follows. In Fig. 4.13(b), retroreflector  $M_1$  is shown as ACD. For calculation purpose, we show movement of beam instead of movement of

$M_1$  and it does not change the explanation. The dotted and solid red lines are the same incoming beam which fall on different parts of  $M_1$  when  $M_1$  is shifted laterally (see Inset of Fig. 4.13(b)). Two beam entering at point P and Q travels the equal path which is equal to AD. The line BC divides beam path into equal halves. We calculate beam path in one half and multiply it by two to get actual path. Since ABC is a right-angled triangle where  $\angle A$  and  $\angle B$  are  $45^\circ$  and  $\angle C =$

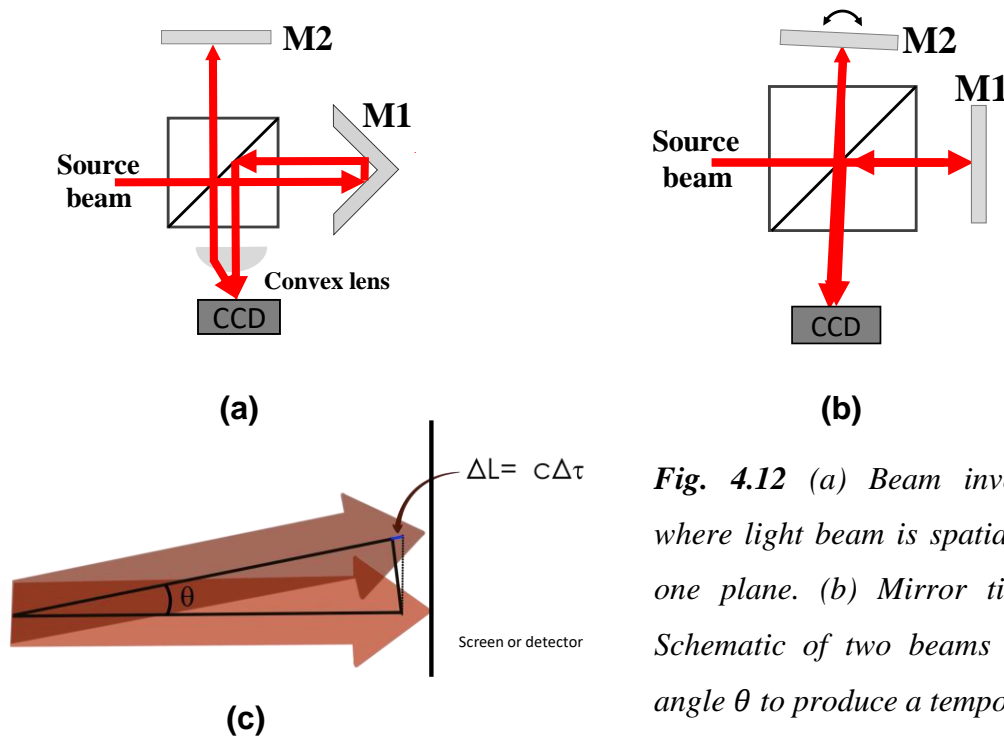


**Fig. 4.12** (a) Beam inversion method where light beam is spatially inverted on one plane. (b) Mirror tilt method. (c) Schematic of two beams meeting at an angle  $\theta$  to produce a temporal shift/lag.

$90^\circ$ , therefore, height and base of triangle are equal i.e.  $BC=AB$ . APR and RSC are also right angled triangles similar to ABC, hence,  $AP=PR$  and  $RS=SC$ . RS is also equal to PB since these are two arms of the rectangle RSBP. Half beam path =  $PR+RS$  which is equal to  $AP+PB = AB$ . Similarly, for solid red line,  $QU+UV=AQ+QB=AB$ . Both the beam travel same path which is equal to  $2AB$ . This shows that ideally, lateral shift of  $M_1$  do not change the beam path and does not introduce any  $\Delta\tau$ .

In Fig. 4.14(a), 2D image of  $I_{int}$  is shown for partial separation of  $I_1$  and  $I_2$  by  $\Delta r \sim 2.8$  mm on CCD coordinates. The  $\sigma$ -axis is chosen at the middle of fringe pattern and  $I_{int}(\sigma)$ ,  $I_1(\sigma)$ ,  $I_2(\sigma)$  is plotted on Fig. 4.14(b). The  $\sigma$ -axis is chosen at the middle of the fringe pattern and perpendicular to the direction of spatial translation along X, which is parallel to the lateral shift of  $M_1$  along the horizontal plane. The  $S(\sigma)$  calculated from these intensities using Eq. (4.6) and  $S(\sigma)$  shows clear cosine pattern in Fig. 4.14(c). The piezo motion does not change

the fringe orientation due to stability of motion of piezo actuator, however, the stage movement can change the direction of beam (say by only  $0.1^\circ$ ) along the fringe length, and it can change the orientation of fringes by  $\sim 10^\circ$ . However, we refrained from physically intervening the retroreflector orientation during the measurement to correct the fringe direction.

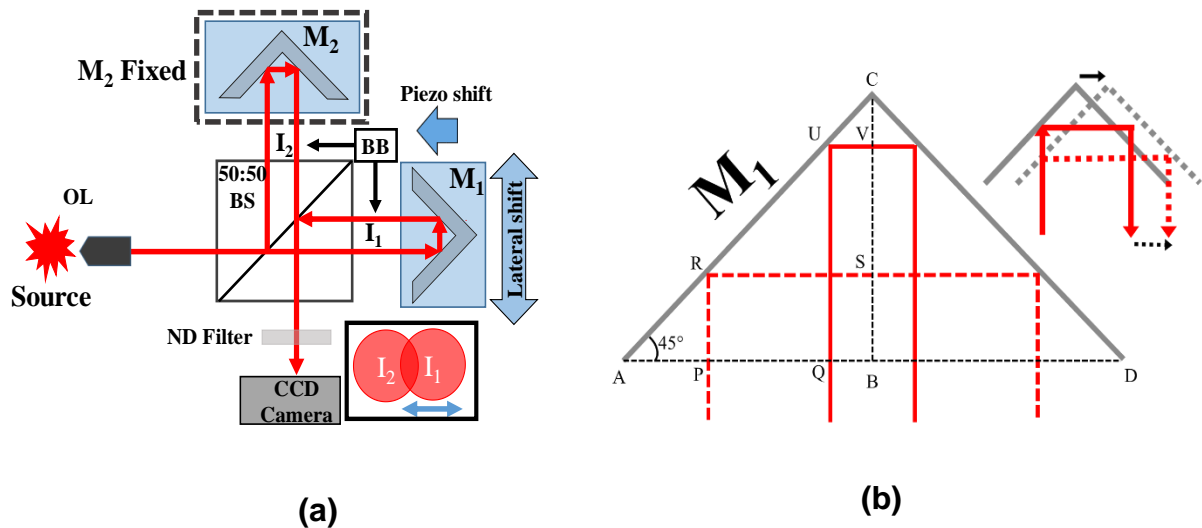


**Fig 4.13** (a) Schematic of spatial correlation measurement setup. Linear stage of  $M_2$  is locked at a fixed position such that  $L_1 \approx L_2$ .  $M_1$  move in lateral direction to shift  $I_1$  beam to change spatial overlap of  $I_1$  and  $I_2$  as shown in inset of (a). Piezo moves in the direction indicated by arrow labelled as ‘Piezo shift’. (b) Trigonometric representation of linear beam shift by lateral shift of  $M_1$ . Right angled grey lines are two reflecting faces of retroreflector  $M_1$ . In the inset, red dotted and solid lines are same beam only reflected from different part of  $M_1$  due to shift of  $M_1$ .

Ideally, the lateral shift method should not introduce any temporal phase; however, there can be other sources of unwanted temporal phase due to optical misalignment caused by movements of different mechanical components. To eliminate such temporal delays, we use a technique called ‘temporal filtering’. Here we use motion of piezo to take measurements of  $|g^{(1)}(\Delta r, \Delta \tau_p)|$  where  $\Delta r$  is separation between beam spot of  $I_1$  and  $I_2$  and  $\Delta \tau_p$  is fine temporal delay. At every beam separation ( $\Delta r$ ), we allow piezo to take 40 data of  $|g^{(1)}(\Delta r, \Delta \tau_p)|$  with respect to fine temporal delay ( $\Delta \tau_p$ ) while  $\Delta r$  is fixed. These  $|g^{(1)}(\Delta r, \Delta \tau_p)|$  at different  $\Delta r$  values are plotted in Fig. 4.15(a). The maximum value of

$|g^{(1)}(\Delta r, \Delta\tau_p)|$  of every curve indicates the position of  $\Delta\tau_p = 0$ . These maximum values are picked and plotted against  $\Delta r$  in Fig. 4.15(b). This way, we are able to filter any contribution of  $\Delta\tau$  in spatial coherence measurement and  $|g^{(1)}(\Delta r)|$  is estimated. The curve of  $|g^{(1)}(\Delta r)|$  is fitted with Lorentz function as given in Eq. (4.9) where  $\Delta\tau$  and  $\Delta\tau_{center}$  is replaced by  $\Delta r$  and  $r_{center}$ .  $R^2$  value of fitting is 0.994.  $g_0$  is 0.2,  $r_{center}$  is 0.01 and  $A_r$  is  $3.8 \text{ mm}^2$ . FWHM is 3.8 mm

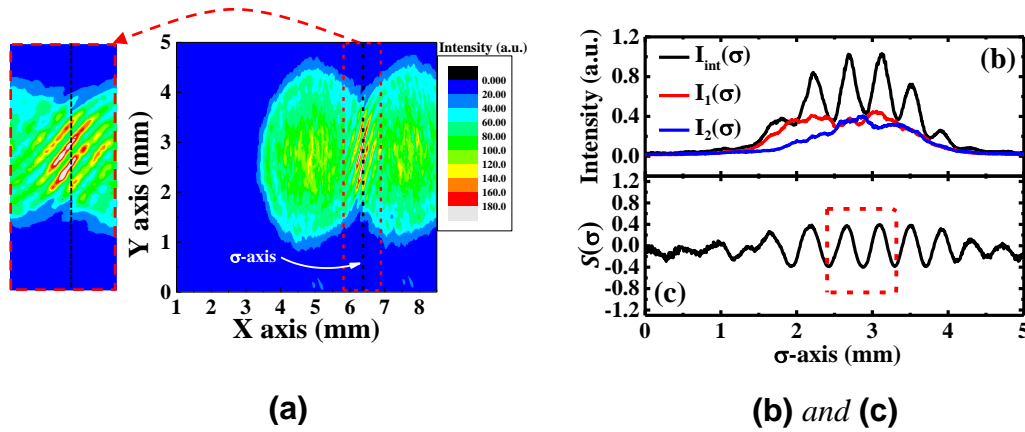


**Fig. 4.14** Interference image due to partial overlap of  $I_1$  and  $I_2$  beams. Beams are separated by  $\sim 2.8 \text{ mm}$  on CCD sensor coordinates. The  $\sigma$ -axis is in the centre of interference pattern indicated by black dotted line. Magnified image of interference pattern is shown in red dashed box (left). (b)  $I_1(\sigma)$ ,  $I_2(\sigma)$  and  $I_{int}(\sigma)$  are extracted from interference image along  $\sigma$ -axis. (c)  $S(\sigma)$  is calculated using Eq. (4.6).

with standard error of fitting  $\sim 0.2 \text{ mm}$ . Here, the standard error of fitting is greater than the instrumental precision of  $r$ , hence it is being used as uncertainty in FWHM. The FWHM length can be called as a length on beam image up to which correlation is significant. Since we are using magnification of  $10\times$ , on the emitting surface of source, this length is  $380 \pm 20 \mu\text{m}$ . This can be called ‘spatial coherence length’ ( $r_c$ ) on the surface of emission.

The obvious question is if ‘spatial filtering’ is actually required during temporal correlation measurement. If there is any spatial separation between two beams during temporal correlation measurement, it can be visualized by four cursor lines in CCD computer output and then corrected. However, temporal phases are not visualized through CCD output, therefore,



temporal filtering method is required. This correction method can be applied to earlier method shown in Fig. 4.12(a) and (b).

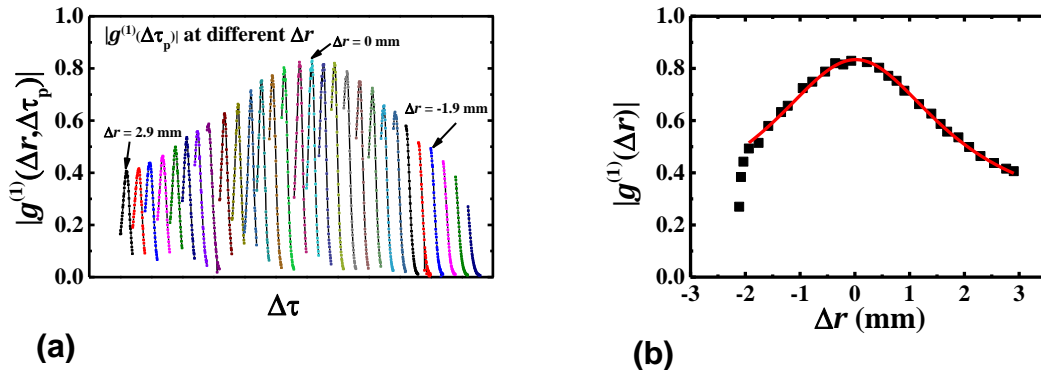
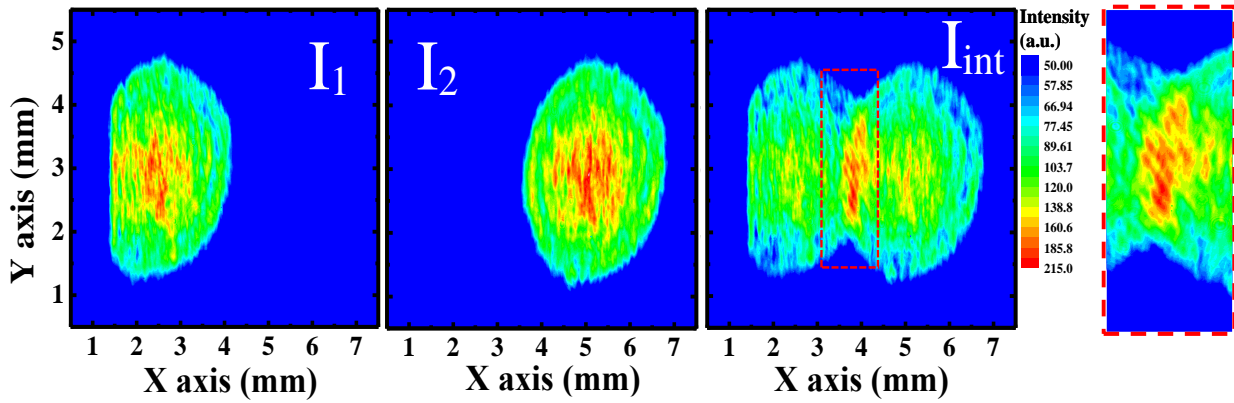
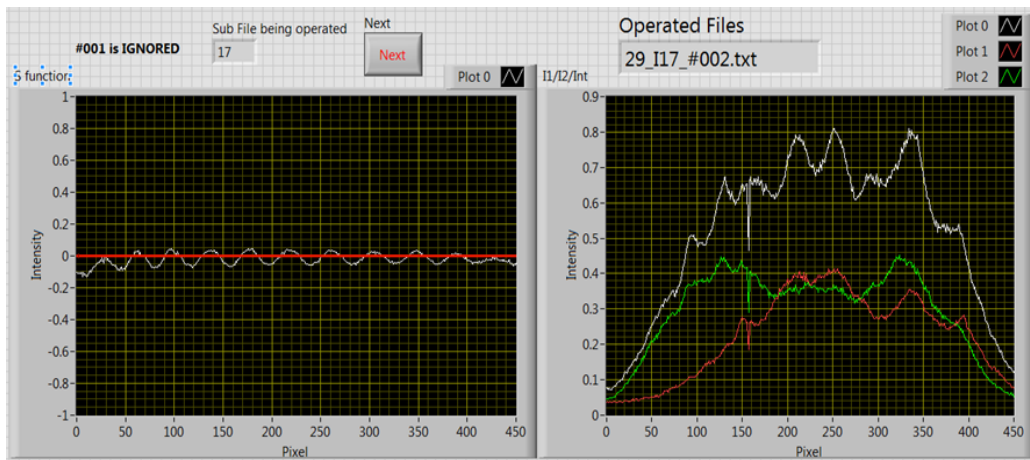


**Fig. 4.15** (a) shows the calculated  $|g^{(1)}(\Delta r, \Delta \tau_p)|$  plotted against fine motion of piezo ( $\Delta \tau_p$ ) for different spatial separation ( $\Delta r$ ) of  $I_1$  and  $I_2$ . The  $I_1$  beam shifts laterally from  $\Delta r = 2.9$  mm to  $\Delta r = -2.0$  mm with respect to  $I_2$  beam. At each  $\Delta r$ , the individual curve shows  $|g^{(1)}(\Delta \tau_p)|$  plotted against fine  $\Delta \tau$  motion of piezo actuator. The maxima of these curves is  $|g^{(1)}(\Delta \tau = 0)|$  or simply  $g^{(1)}(r)$ . (b) shows the maxima of  $|g^{(1)}(\Delta \tau_p)|$  plotted against  $r$  as  $|g^{(1)}(\Delta r)|$ . The curve is fitted with Lorentzian function and indicated by red line.

Another important issue is about using the visibility method to measure  $|g^{(1)}|$ . We did not use visibility since it requires a strict condition of  $I_1 = I_2$  which is not always fulfilled if the beam under investigation is not circularly symmetric in intensity around center. This is certainly not the case for many light emitting sources. Fig. 4.16(a) show  $I_1$  and  $I_2$  and their partial overlap to form interference pattern  $I_{int}$ . When  $\sigma$ -axis is taken at the centre of interference pattern, the resulting  $I_1(\sigma)$ ,  $I_2(\sigma)$  and  $I_{int}(\sigma)$  are shown in Fig. 4.16(b) (right). The intensities of  $I_1(\sigma)$ ,  $I_2(\sigma)$  are not exactly equal and  $I_{int}(\sigma)$  does not show clear fringe pattern. However, when Eq. (4.6) is used to calculate  $S(\sigma)$ , a clear cosine pattern is seen. Therefore, we use the method where individual intensities are taken and  $|g^{(1)}|$  is estimated.



(a)



(b)

**Fig. 4.16** (a) The 2D plot of  $I_1$ ,  $I_2$  and  $I_{int}$ . The zoomed data of interference is shown by red dashed rectangle. The interference fringes are barely visible. The analysis method is able to calculate cosine oscillation where intensities are non-symmetric and unequal. (b)(right)  $I_1(\sigma)$ ,  $I_2(\sigma)$  and  $I_{int}(\sigma)$  taken along one  $\sigma$ -axis from  $I_1$ ,  $I_2$  and  $I_{int}$  2D plots. (left) Image of LabVIEW interface where  $S(\sigma)$  is being calculated from  $I_1$ ,  $I_2$  and  $I_{int}$ .

## 4.7 Conclusion

In conclusion, with the instrumentation discussed in this chapter, we are able to provide a table-top instrument to measure temporal and spatial coherence of a light in a single setup. This type of instrument is suitable to study light-matter interactions in condensed matter physics lab. This modified interferometer can be kept outside at room temperature to study the emission from samples kept inside compact systems like cryostat. This setup can be used to study the coherence of those many-body cooperative phenomena discussed above in section 4.1. The

achievement of off-diagonal long range order can be verified with this instrument, and it can be used to further investigate new emerging physics. We have developed the method of ‘temporal filtering’ in the measurement of spatial coherence to avoid the unwanted temporal phase. This method is generalized and can be used in earlier methods of dual measurement. Additionally, we devised a ‘curve overlap’ method to extend the range of instruments while keeping its precision in cases where fine and coarse inputs are provided with independent instruments. So far, we have investigated optical coherence of a commercial diode and a QD-QW heterostructure (Chapter 3), and this method can be applied to probe various other kinds of light emitting systems and photonic devices. In fact, the possibilities are many if we can couple this interferometer with other instruments like Fabri-Perot to find correlation between different cavity modes or couple with E-k spectroscopy set ups to find correlation between lights of different k values. We can further modify this instrument with confocal tools to see correlation between two different quantum dots to study the nature of carrier transport.

## Chapter 5

# Experimental Evidence of Macroscopically Large Quantum Coherent State of Bose-Einstein Condensate of Indirect Excitons

### 5.1 Introduction

The study of collective dynamics of charge carriers and their interactions inside any novel heterostructures is critical in condensed matter physics. These carrier properties play significant roles in applications based on these heterostructures. With certain heterostructure designs (discussed in Chapter 1), the quantum mechanical behaviors of these charge carriers can be observed and manipulated. These include shifting of discrete energy levels in potential confinements via applied bias, controlled tunneling of particles through barriers, charge accumulation layers etc. Earlier in our group, we studied<sup>31</sup> a single barrier sample where an 8 nm AlAs barrier layer is fabricated in GaAs in p-i-n structure. The presence of spatially indirect excitons and their response to applied bias and temperature was studied using the technique of photocapacitance. The sample used in this chapter (InAs dots in AlAs barrier) is already studied<sup>152-154</sup> by other groups, where photocurrent oscillations are observed and explained. However, the study of spatially indirect excitons in this sample is to be done. We pursue the photocapacitance study to find the active role of indirect excitons in photocapacitance oscillations. There can be many possible explanations of photocurrent and photocapacitance oscillations. Here, we argue the possibility of the existence of Bose-Einstein Condensation (BEC) of indirect excitons with photocapacitance results through different experiments. The presented results in this chapter are part of a more extensive ongoing study where other results are published in two theses; PhD Thesis by Dr. Amit Bhunia, IISER Pune and MS Thesis by Mr. Yuvraj Chaudhry, IISER Pune.

A simplistic conduction band schematic is given in Fig. 5.1(a) where discrete energy levels are created in two adjacent quantum wells (QWs). Due to difference in the widths of these QWs, the separations of energy levels in individual QWs are also different. Under an applied bias voltage, the energy level rises and band profile starts to bend creating a potential

gradient across the structure as shown in Fig. 5.1(b). Whenever energy levels of both QW match, it results in enhanced tunneling between two QWs and a large current is expected across the sample. Such energy level matching is one of the required condition for resonant tunneling<sup>155</sup> in quantum structures. With few discrete energy levels in either QW, multiple resonance conditions can result in multiple peaks in tunnel current with variation in applied

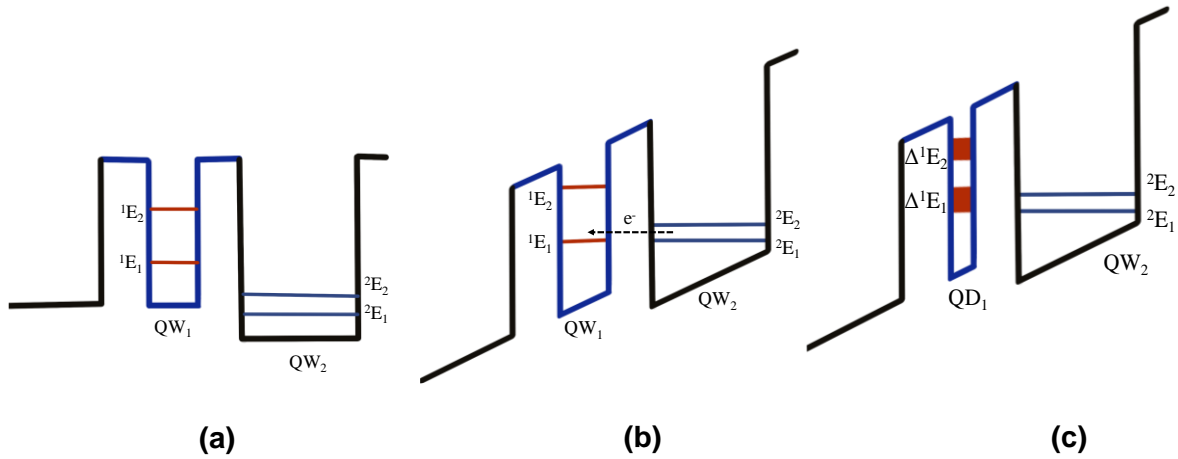


**Fig. 5.1** (a) Simplistic conduction band schematics of two QWs of different widths. <sup>1</sup>E<sub>1,2</sub> are energy levels of QW<sub>1</sub> and <sup>2</sup>E<sub>1,2</sub> are energy levels of QW<sub>2</sub> (b) Application of bias results in band banding and shifting of energy levels. The matching of energy levels results in resonant tunneling of electrons. (c) The QW<sub>1</sub> is replaced with layer of QD with broad size distribution. The discrete energy levels are effectively working as energy bands (Δ<sup>1</sup>E<sub>1,2</sub>).

biases. However, instead of the single QW<sub>1</sub> (see Fig. 5.1(b)), if there is a layer having large numbers (~10<sup>11</sup> cm<sup>-2</sup>) of quantum dots (QDs) having broad size distributions, then the distributions in quantized energy levels of individual QDs will collectively result in an energy band, and any sharp peaks of tunnel current will be suppressed. If tunnel current fluctuations survive within this QD layer, it indicates towards the QD size uniformity. Moreover, if the number of peaks in tunneling current are more than the available energy levels participating in resonant tunneling and if these number of peaks also depend on photoexcitation intensities, then the cause of current oscillations should to be different. It will require the existence of some form of phase coherent resonant tunneling phenomena to explain such observations. Moreover, if electrons choose non-resonant mode of tunneling, and if these number of peaks also depend on photoexcitation intensities, then the cause of such current oscillations should to be different as well.

In a QD laser diode, where the active medium has large numbers of QDs, photons in the optical cavity trigger stimulated photon emission when the condition of population inversion is met. Stimulated emission is a coherent phenomenon where stimulated photons are in phase with the photons in the optical cavity. This type of collective phase coherent behavior of millions of QDs is the reason behind these coherent light emissions from QD-based laser diodes. Suppose similar phase coherence is achieved among QDs through some other physical process (say tunneling current). In that case, the similar collective behavior of QDs can also be witnessed in optical and electrical measurements. Many-body cooperative phenomena in condensed matter physics such as BEC<sup>6,145-149,156</sup> actually shows such coherent behaviors. The bosonic quasi-particles excitons, owing to their low effective mass, are expected to show BEC within semiconductor based quantum heterostructures.

In this chapter, we will present the investigation of a p-i-n heterostructure having InAs QD layer separated from GaAs triangular quantum well (TQW) by an AlAs barrier, similar to Fig. 5.1(c). These spatial separated QD-TQW can allow the indirect exciton in the 0D-2D configuration where hole of QD is restricted in zero dimensional QD while electrons of TQW have two dimensional freedom. Under the photoexcitation, these indirect excitons can show macroscopic coherent behavior under certain applied voltage biases and excitation intensities. We use capacitance measurement to specifically study these spatially indirect excitons to find their role in the observed oscillations. As such, the excitonic BEC is reported in III-V semiconductors at cryogenic temperatures, however, in this chapter, we argue that the required conditions of BEC can be matched for higher temperatures up to ~100 K if we manipulate the system electrically and optically. For example, photoexcitation of barrier heterostructure under selective applied bias can form spatially indirect exciton which has higher binding energy. A direct photon absorption to form indirect exciton and coherent resonant tunneling of electron between QD and TQW can restrict the available momentum space for the electrons of these indirect excitons which can result in momentum space narrowing. With such controlled manipulations, can indirect excitons form BEC? We will discuss these conditions in details with the experimental results.

The sample is investigated in both forward and reverse bias, but we particularly focus on the reverse bias in this chapter. Reader is advised to go through reference 157 for additional details of the presented work. Some of the experimental results and analysis, which are required to clarify the conclusion of this chapter, will be referred.

## 5.2 Experimental details

### 5.2.1 Sample Details

We use a single crystal having double barrier p-i-n heterostructure grown in the lab of Prof. Mohamed Henini in University of Nottingham, United Kingdom. The InAs quantum dots are grown in between AlAs barrier layers in the GaAs/AlAs/GaAs quantum heterostructure by Molecular beam epitaxy (MBE). The growth sequences are the following. The structure is grown on highly doped n-type GaAs substrate. On top of the substrate, a 1  $\mu\text{m}$  layer of heavily doped n-type ( $4 \times 10^{18} \text{ cm}^{-3}$ ) GaAs is grown at 550  $^{\circ}\text{C}$ . This highly doped layer serves as bottom side ohmic electrical contact along with gold for our measurements. Next, a 100 nm layer of n-type ( $2 \times 10^{16} \text{ cm}^{-3}$ ) GaAs is grown followed by 100 nm of GaAs spacer layer. A 1.8 monolayer of InAs is then deposited between two 5.1 nm wide barrier layers of AlAs. The strain induced quantum dots are formed with an areal density of  $\sim 1 \times 10^{11} \text{ cm}^{-2}$ . On top of these layers, an undoped layer of GaAs having 60 nm width is deposited. This is then followed by

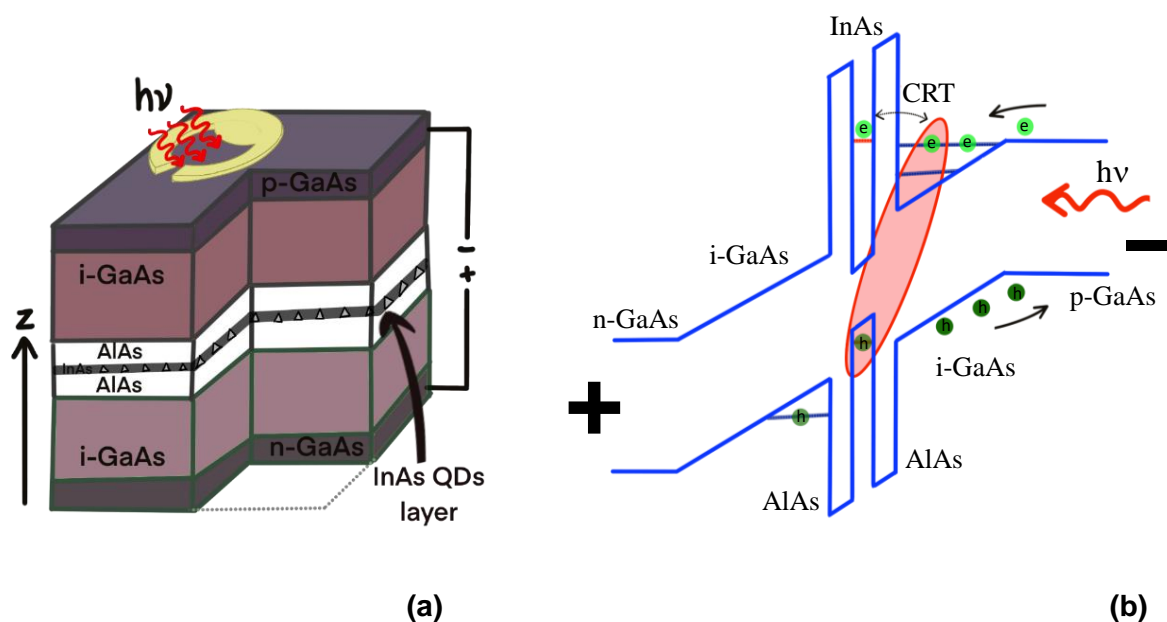


**Fig. 5.2** (a) The schematic of different layers of sample. Here  $z$  is the growth direction as well the direction of application of applied reverse bias. Photoexcitation is provided through golden mesa. (b) Schematics of band diagram under reverse bias.

510 nm of heavily doped p-type ( $2 \times 10^{18} \text{ cm}^{-3}$ ) GaAs layer. This highly doped layer is used to facilitate the fabrication of top side ohmic electrical contact. On top, a golden mesa of  $\sim 200 \mu\text{m}$  diameter is deposited to provide ohmic type electrical access as well as an area to probe the

structure optically. The simple schematics of the sample structure and the associate band diagram is given in Fig. 5.2.

## 5.2.2 Experimental setup and methods

Studies on this sample is mostly done at cryogenic temperatures ( $< 13$  K) which is achieved with the help of closed cycle cryostat CS-204S-DMX-20 from Advanced Research Systems and Lakeshore (Model-340) temperature controller. The photoexcitation is provided through p-GaAs side (see Fig. 5.2) using three following sources

- I. 1000-W quartz-tungsten-halogen lamp from Newport, a white light source
- II. Ion Laser 177-G02 (Newport) emitting at 488 nm
- III. He-Ne Gas laser emitting at 633 nm.

Depending upon the experiment, one or a combination of two sources are used for photoexcitation. Impedance measurements which yield the value of capacitance and conductance are measured by Agilent's E4980A LCR meter. For capacitive measurement, AC bias can be modulated over DC applied bias with a condition that AC modulation are orders of magnitude lower than DC bias. We use an AC modulation of  $30 \text{ mV}_{\text{RMS}}$  with 10 kHz frequency. The DC biases are typically in  $\sim$ Volts; therefore, AC modulations do not affect the overall response of sample due to applied DC bias. The typical capacitance of sample is  $\sim$ pF which can offer reactance ( $X_c$ ) of  $\sim 160 \text{ M}\Omega$  at frequency of 10 kHz. Therefore, parallel circuit mode ( $C_p$  mode) is used in LCR meter as shown in Fig. 5.3(a), where parallel resistance  $R_p$  can be significant compared to  $X_c$ . Conductance  $G = 1/R_p$  is shown as  $G/\omega$  to make it in same unit as capacitance (pF) and, it is measured simultaneously with capacitance. Hereon, we will use only capacitance measurement and simultaneous  $G/\omega$  measurement is implied. Along with these impedance measurements, we also measure DC and AC currents. In particular, the short-circuit and open-circuit based impedance corrections are made to avoid residual capacitance due to electrical cables or other circuitry elements.

For spectral measurements, we use Acton Research SP2555 monochromator ( $f = 0.5$  m,  $\sim 9$  nm bandwidth) and quartz-tungsten-halogen lamp to photoexcite sample and collect their response with LCR meter. To focus photoexcitation beam over sample, we use Keithley 2611 sourcemeter to measure the photocurrent response in real time while adjusting the beam position. This helps us to correctly align our setup.



The photo responses of this sample are studied under different experimental conditions and all results (capacitance, conductance, DC current, AC current) are collected simultaneously from single instrument which suppresses the possibility of any random error between different results. Other cautionary factor is to check if there is any offset, systematic error between different results which might be leading to incorrect analysis. During different sets of

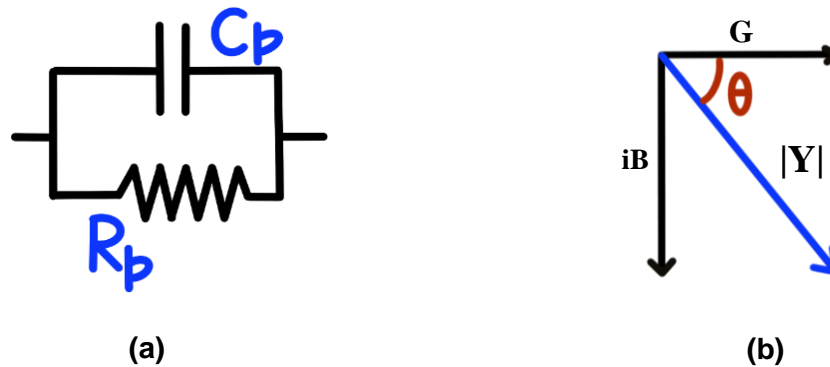


**Fig. 5.3** (a) Capacitance and conductance measurement mode (parallel mode,  $C_p$ ). (b) Complex valued admittance  $|Y| (= \sqrt{G^2 + B^2})$  is measured across parallel circuit where  $G = \text{Conductance}$  and  $B = \text{Susceptance}$ . Capacitance is estimated from  $B = \omega C$  where  $C$  is capacitance and  $\omega$  is AC frequency.

experiments (intensity dependent), we see the phase varies over the range of bias and in-phase behavior turns to out-phase, which would not be possible with a systematic error in phase. We calibrate the capacitance measurement regularly with a standard capacitor for any possible error. Once assured with data, we further proceed to analysis and found that these impedance oscillations are not merely the result of simple energy-level matching related resonant tunneling but a phase coherent phenomenon where millions of QDs behave collectively.

### 5.3 Background research and earlier results

A similar sample is studied by Vdovin *et al.*<sup>152–154</sup> where oscillations were observed in DC photocurrent. In our research group, we took another approach by measuring the variation of photocapacitance to probe the average electrical polarization of the excitons as mentioned before. All these results in this chapter are under reverse bias and under photoexcitation. The capacitance is referred as photocapacitance (PhCap) and the photoconductance (PhG) as  $\text{PhG}/\omega$ . The PhG is divided by  $\omega$  to keep both capacitance and conductance in the same unit

(farad). Earlier in our group<sup>31,32,113</sup>, we showed that PhCap measurement is able to pick the dipolar states in the deeper layers of such heterostructure where optical response is very feeble. Therefore, any dipolar entity inside the heterostructure should respond to PhCap measurement.

## 5.4 Temperature dependent measurement of Photocapacitance and Photoconductance

As mentioned above, the PhCap is measure of average polarization of excitonic dipoles and increase in number of dipoles or alignment of dipolar orientation in one direction results in increased PhCap. If  $\sigma_{IX}$  is surface density of indirect excitons<sup>32</sup> across the AlAs barrier layer and  $\langle \vec{P} \rangle$  is effective polarization due to these indirect excitons then  $\sigma_{IX}$  and  $\langle \vec{P} \rangle$  can be estimated with PhCap and applied bias (V) as  $(\text{PhCap})V = \sigma_{IX}e = \langle \vec{P} \rangle \cdot \hat{z}$ , where  $e$  is electronic charge

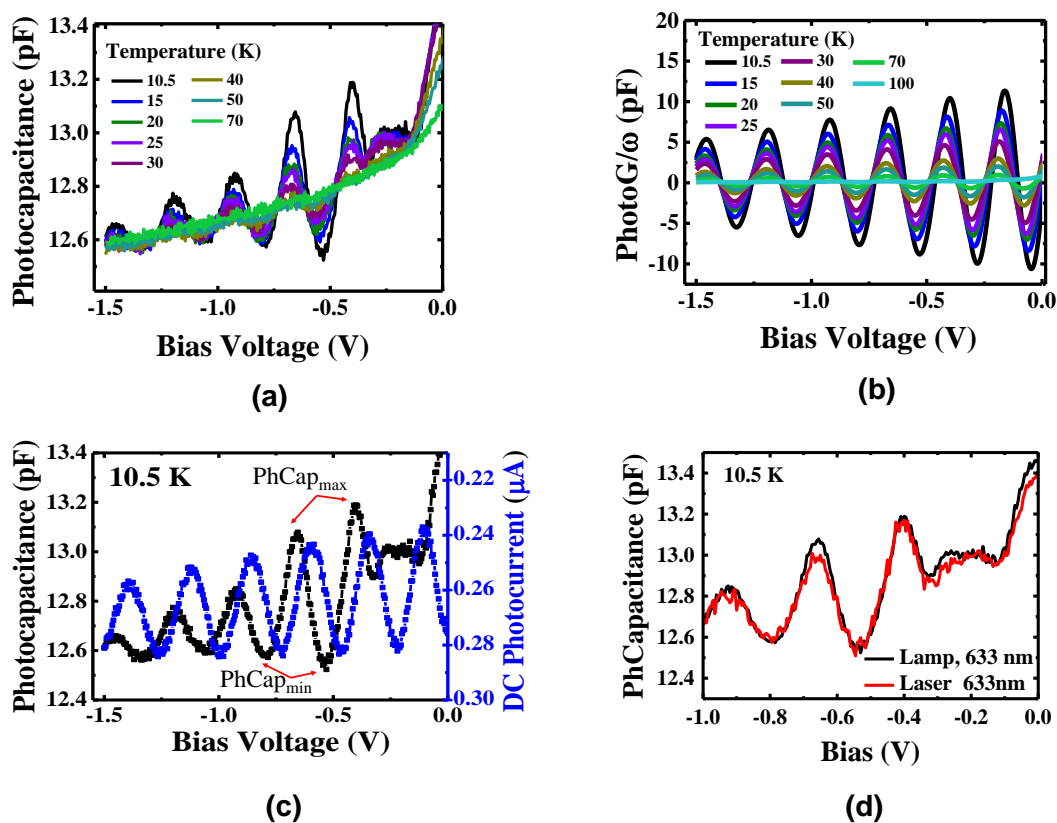


*Fig. 5.4 (a) PhCap vs applied bias taken for different temperatures. (b) Similarly, PhotoG/ω is plotted for different temperatures. (c) PhCap and Photocurrent comparison at 10.5K (d) Comparison between photo excitation by laser (633 nm) and lamp (633 nm).*

and  $\hat{z}$  is the direction of applied bias. As the bias is increased, the photogenerated charge carriers are driven towards AlAs barrier layer resulting in higher density of dipoles ( $\sigma_{IX}$ ). Consequently, more excitonic dipoles are formed and the PhCap should increase with increasing bias, however, we notice periodic oscillations with respect to bias as shown in Fig. 5.4(a), (b) and (c).

At first, it appears to have come from the resonant tunneling of electrons where energy levels of TQW match with the energy level of QDs. As a result of this sequential tunneling, PhCap oscillates (see Fig. 5.2(b)). However, the period of oscillations over the bias is almost constant<sup>154</sup> which contradicts any sequential tunneling since energy levels of TQW are not evenly spaced. Moreover, the number of oscillations<sup>154</sup> are much larger than the typical number of energy levels residing in TQW of such samples. Therefore, such simple minded, sequential tunneling due to energy level matching does not answer these oscillations. Once this energy level matching condition is ruled out, the other possible resonance condition can come from momentum space distribution of carriers (electron and hole). As argued above, the effective polarization  $\langle \vec{P} \rangle \cdot \hat{z}$  can increase with increasing number of dipole (excitons) or orientation of dipoles in one direction. Applied bias drives the carrier towards AlAs barrier which increases the number of dipoles but this too does not answers the lowering of PhCap at periodic bias voltage. The DC photocurrent is also out of phase with PhCap as shown in Fig. 5.4(c). During the temperature dependent measurement, as show in Fig. 5.4(a) and (b), the spontaneous PhCap oscillations start below  $\sim 100$  K. It has been predicted that excitons owing to their low effective mass and bosonic nature can go under Bose Einstein condensation (BEC) at cryogenic temperatures. When excitons go under such phase transition, the indirect excitons collectively align towards one direction as represented by schematics in Fig. 5.5. In this chapter, we pursue this possibility.

Before we go to experimental verification of BEC, let us see the resonant tunneling and spontaneous increase of polarization together. It is understood that these sharp oscillations of PhCap with bias cannot be due to non-resonant tunneling which has a broad distribution of allowed energies. And, resonant tunneling<sup>158,159</sup> of electron between TQW and QD requires

$$E_{QD}^e(V, I) = E_{TQW}^e(V, I) + \left[ \frac{\hbar^2}{2m^*} (\vec{k}_x^2 + \vec{k}_y^2) + \Phi^{EX}_{xy}(V, I) \right] + (eV) \quad (5.1)$$

Where  $E_{QD}^e(V, I)$  and  $E_{TQW}^e$  are ground state energies of QD and TQW, respectively.  $k_x$  and  $k_y$  are in-plane momentum of electron in TQW,  $\Phi^{EX}_{xy}(V, I)$  is net Coulomb interaction energy

of these indirect excitons in the x-y plane and  $I$  is light intensity of photoexcitation. Resonant tunneling of ensembles of electrons at a particular bias and intensity is possible if  $\left[ \frac{\hbar^2}{2m^*} (\vec{k}_x^2 + \vec{k}_y^2) + \Phi^{EX}_{xy}(V, I) \right]$  is same for all electrons. In this term, there are three variables ( $k_x$ ,  $k_y$  and  $\Phi^{EX}_{xy}(V, I)$ ) which makes a large range of all possible combinations. However, for a direct photoexcitation of indirect excitons at the minimum of Brillouin zone, the excitonic momentum ( $\vec{K}_{IX}(V_0)$ ) must be

$$\vec{K}_{IX}(V_0) = \vec{k}_e^{TQW}(V_0) + \vec{k}_h^{QD}(V_0) \cong 0 \quad (5.2)$$

where  $\vec{k}_e^{TQW}(V_0)$  is momentum of electron in ground energy level of TQW and  $\vec{k}_h^{QD}(V_0)$  is momentum of hole in QD at ‘resonant bias voltage’  $V_0$ . The electrons of these photogenerated excitons are taking part in resonant tunneling then these must follow the condition of constant phase<sup>160</sup>  $\theta = \vec{k}_e^{TQW}(V_0) \cdot \vec{z}_{QD}$  assuming nearly monodisperse InAs QDs, specifically in the

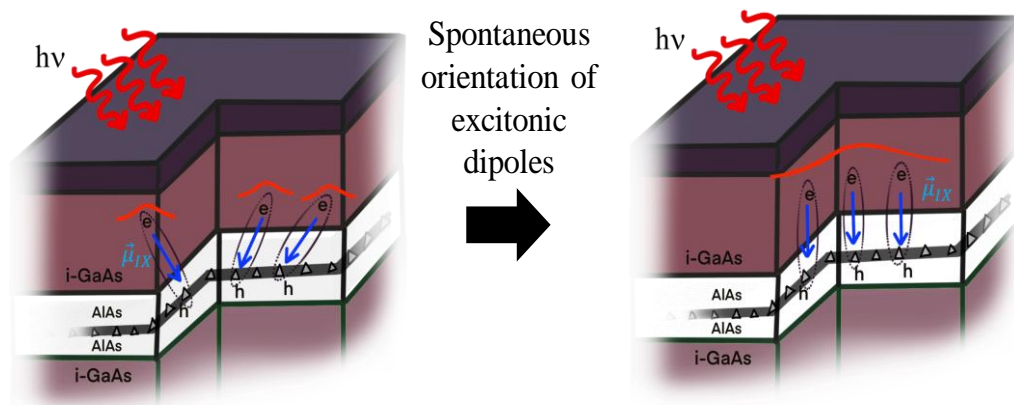


**Fig. 5.5** Spontaneous enhancement of effective polarization due to orientation of excitonic dipole in one direction. On left the curved red lines are representative wave function of individual indirect excitons above  $\sim 100$  K. On right, the red curve represent wave function of macroscopic quantum state of excitonic BEC.

$\vec{z}_{QD}$  direction. On top of it, direct photoexcitation puts the condition  $|\vec{k}_e^{2DEG}(V_0, I_0)| \rightarrow |\vec{k}_h^{InAs}(V_0, I_0)|$ . These two conditions present the evidence of momentum-space narrowing which is one of the condition to form BEC and that leads to spontaneous enhancement of collective polarization  $\langle \vec{P} \rangle$ .

After the condition of resonance, the  $\langle \vec{P} \rangle$  falls below dark capacitance since the condition of resonance is lost. The increased bias also increases density of excitons at junction and excessive charge carrier tunnel out of heterojunction until the next condition resonance is reached. This way, excitonic system oscillate between the conditions of resonance and non-resonance.

The temperature dependent data is taken by photoexcitation through lamp at 633 nm using monochromator. The data is compared with photoexcitation of laser (similar intensity to lamp power) and it showed that coherent laser did not impact the behavior of PhCap. The further experiments are done with laser and it will be shown that coherence of excitation light is not relevant for these oscillations.

## 5.5 Experimental evidence of BEC

The critical density for two-dimensional BEC as order parameter<sup>161</sup>, calculated in reference 157 for the same sample, is  $\sim 1.52 \times 10^{11}/\text{cm}^2$  at 10 K which is close to excitonic dipolar density  $\sigma_{IX} \sim 1.099 \times 10^{11}/\text{cm}^2$  estimated from peak capacitance value at 10 K. The thermal de-Broglie wavelength ( $\lambda_{Th}$ )  $\sim 100$  nm is bigger than the average inter-dot separation ( $\sim 11$  nm) in QD plane. The critical temperatures estimated via BEC and Berezinskii-Kosterlitz-Thouless (BKT)<sup>162,163</sup> theories for the III-V material system came out to be near 100 K, around which the oscillation in PhCap is observed. Please see reference 157 section IV for detailed information on these analyses.

### 5.5.1 Interference of two macroscopic groups of excitons

Although, the estimated critical density and temperatures are close to experimental values of excitonic BEC, however, further experimental observations are needed. We tried three different experiments. Long range phase coherence is one of the characteristic experimental signature of a macroscopic quantum state like BEC. The schematics of first experimental setup is shown in Fig. 5.6(a). We used a He-Ne laser, a beam splitter and a plano-convex lens to focus the laser beam on sample. The macroscopically large laser spot is moved over the golden mesa by moving the beam splitter and PhCap is recorded at different location of beam spot. The schematics of different scenario is given in Fig. 5.6(b) where laser spot moves from one side of mesa and crosses over it. When light spot is away from mesa, obviously no excitation would show no PhCap oscillations. As light approaches the mesa, the oscillations

in PhCap start to appear. When beam spot bifurcated by circumference of golden ring, the

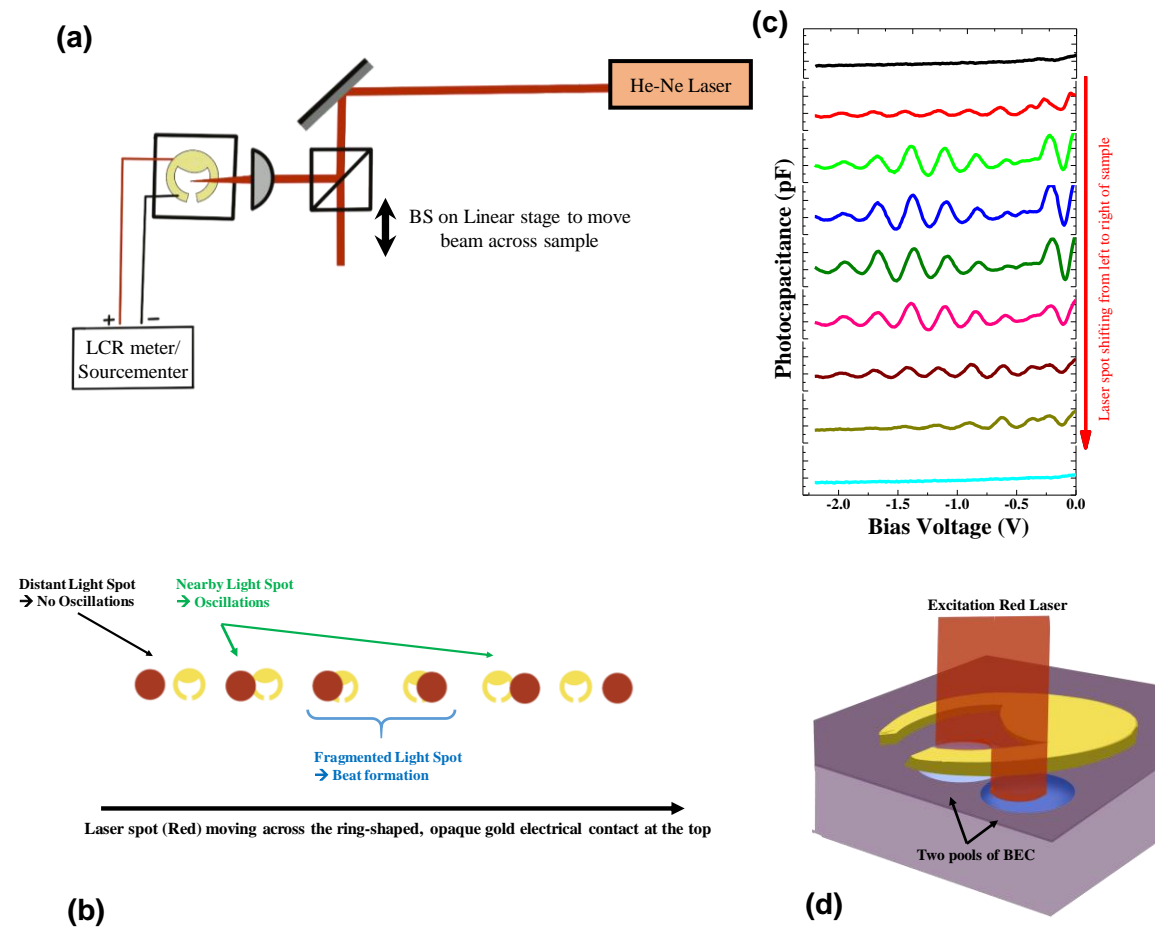


**Fig. 5.6** (a) Schematics of experimental setup. (b) Representation of different scenario of laser beam spot crossing over golden mesa. (c) PhCap vs Bias at the different scenario shown in (b). (d) Simplified image to show two pools of BEC due to fragmentation of beam spot.

interferometric beat pattern starts to appear in PhCap. Results are shown in Fig. 5.6(c). The fragmented excitations possibly create two pools of excitonic BEC on either side of ring and interference of these two phase correlated states leads to beat pattern in PhCap. This scenario is demonstrated in Fig. 5.6(d).

In second experiment, the focusing lens is moved backward to change the distance between sample and lens which resulted in increasing excitation spot size of laser. The schematics of experimental setup and PhCap results are shown in Fig. 5.7(a) and (b), respectively. The similar beat pattern is observed as laser spot size increased. This arrangement

also also create two pools of BEC when spot size is big enough to reside on inner and out sides of golden mesa similar to the case show in Fig. 5.6(b).

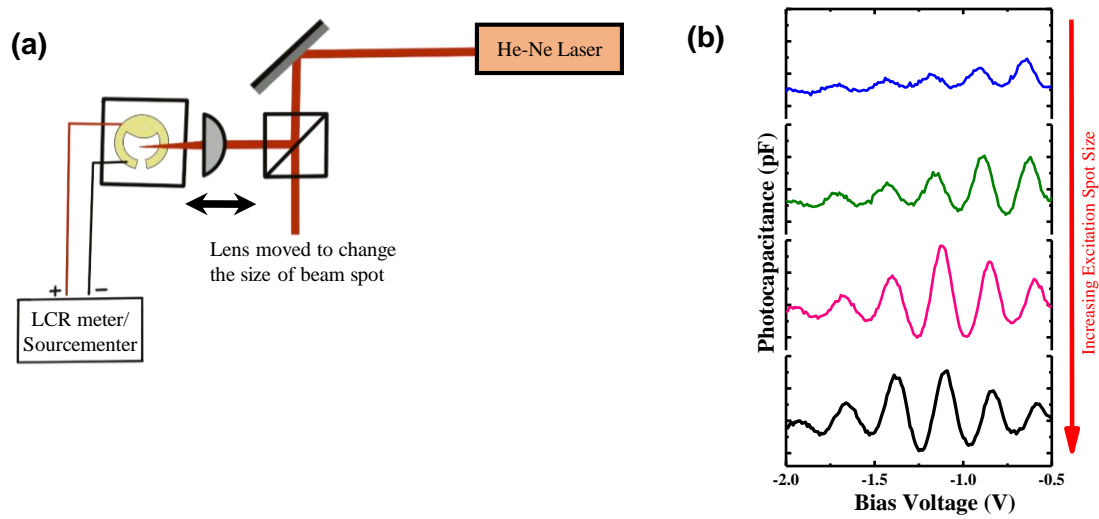


**Fig. 5.7** (a) Schematics of experimental setup. The distance of lens is moved to change the beam spot size. (b) The PhCap plot vs increasing excitation size.

In third experiment, two pools of BEC are created by using two independent lasers namely 633 nm emitting He-Ne laser and 488 nm emitting ion laser. The schematic of experimental setup is given in Fig. 5.8(a). The PhCap response is recorded with individual lasers (while other laser is shut), and simple oscillations in PhCap are observed. When both lasers excited the sample simultaneously, interference beat pattern showed. The results are plotted in Fig. 5.8(b). Combined effect does not match with simple algebraic addition of PhCap due to either lasers. The effect is generated by the combination of two excitations. Two BEC with a different in-plane Coulomb correlation energy  $\Phi^{EX}_{xy}(V, I)$  oscillate (with respect to bias) with slightly different frequencies resulting in interference of these two excitonic states. The contrast  $\left(\frac{C_{max}-C_{min}}{C_{max}+C_{min}}\right)$ , where  $C_{max}$  and  $C_{min}$  are consecutive maximum and minimum value of PhCap oscillation is a measure of first order correlation. This contrast increase with increased photoexcitation intensity indicating towards density dependent phase transition to excitonic BEC state. Also, phase correlation of two pools of excitonic BEC states is a measure spatial coherence<sup>164,165</sup> and off-diagonal long range order (ODLRO)<sup>86</sup> of a quantum entangled state. The previous three experiments were done with lasers, which are highly coherent sources. However, two independent lasers are not correlated and the effect of interference is still seen with two lasers. To discard the possibility of laser coherence making any impact on the

interference of PhCap, the experiment is done with white light using a lamp. The schematics is shown in Fig. 5.9(a), the monochromator is used in open mode where it allows the white light to pass through. Similar beat pattern is observed even with incoherent white light. Interference of photocapacitance oscillations indicates that phase coherence is not from the coherence of

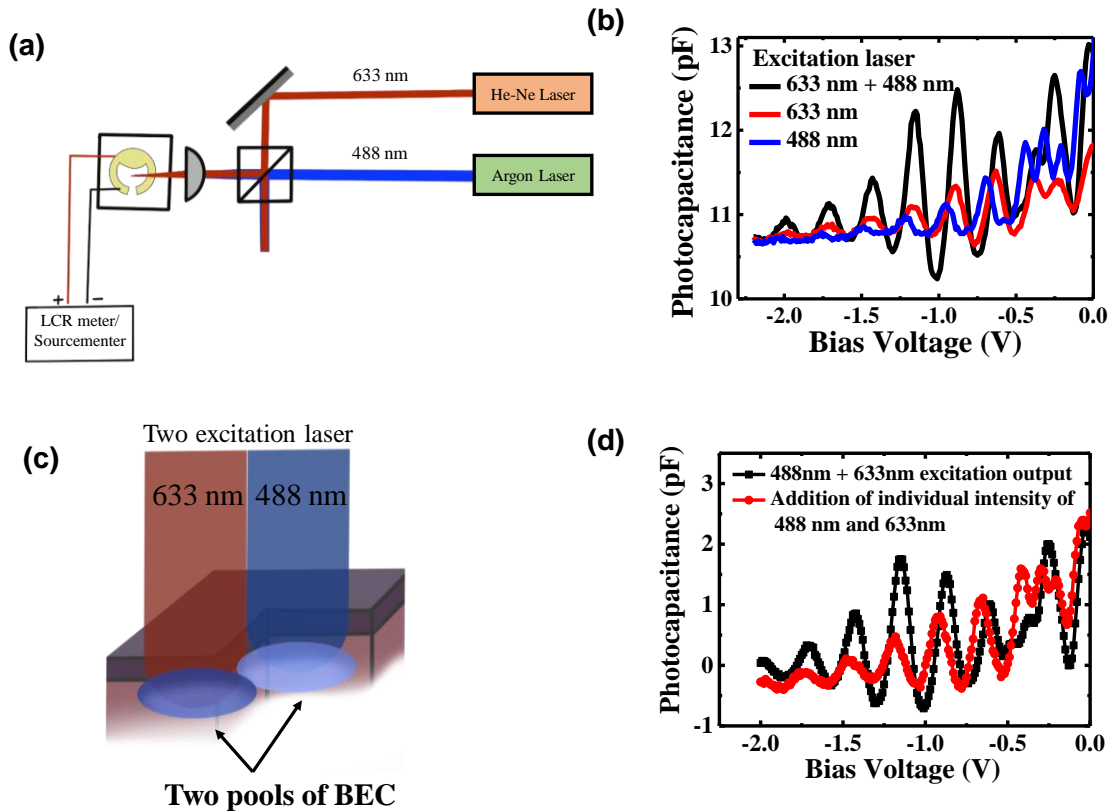


**Fig. 5.8** (a) Schematics of experimental setup. (b) The PhCap resulting from simultaneous and individual excitation of two lasers (633 nm and 488 nm). (c) The schematics of two excitonic BEC pools being created by two lasers. (d) Comparison between PhCaps due to combined laser and numerically calculated algebraic sum of PhCap due to individual laser after the dark capacitance is subtracted.

excitation light but it is possibly due to the presence of stable, long range spatial correlation among these indirect excitons as well as the existence excitonic matter waves.



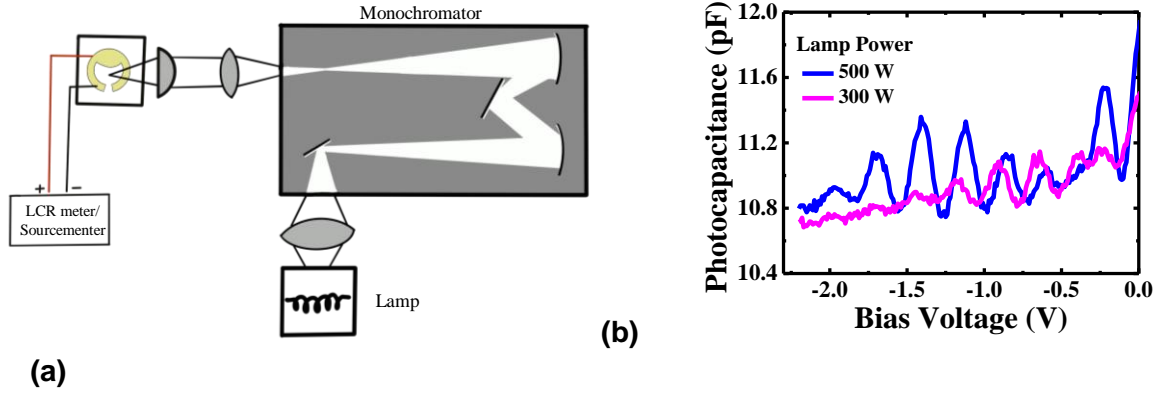


**Fig. 5.9** (a) Schematics of experimental setup. (b) PhCap with white light at different lamp power.

### 5.5.2 Rabi Oscillation of excitonic BEC state

At the fix biases of maximum and minimum of PhCap as shown in Fig. 5.4(c), we varied intensity of photoexcitation and recorded the response of PhCap. The schematics of experimental setup is given in Fig. 5.10(a). Here we used two sets discrete ND filters (Newport) and one variable ND filter (Newport) to vary the intensity. The photocurrent plotted for PhCap<sub>max</sub> and PhCap<sub>min</sub> with varying intensity is plotted in Fig. 5.10(b). There are no photocurrent oscillations, however, PhCap and PhG/ $\omega$  show oscillations. Such oscillations without the condition of resonance can come from Rabi oscillation of the BEC state. The excitonic Rabi oscillation against photoexcitation amplitude (Intensity<sup>0.5</sup>) are reported for single QD<sup>166–170</sup>. Here, we see the Rabi oscillation of macroscopic coherent state of excitons. The result of PhCap and PhG/ $\omega$  with respect to varying intensity are shown in Fig. 5.10(c) and (d).

It is known that continuous excitation (e.g. continuous wave lasers) can also drive two-level quantum system into stable, steady state even in the presence of decoherence<sup>171–173</sup>. However, Rabi oscillations are seen with pulsed lasers at times much shorter than the dephasing time ( $\tau_\gamma$ ) (see reference<sup>157</sup>). Rabi frequency is  $\Omega_R = |\vec{\mu}_{12} \cdot \vec{E} / \hbar|$  and pulse area is  $= |\vec{\mu}_{12} \cdot [\int_0^{\Delta\tau} \vec{E}(t) \left(\frac{dt}{\hbar}\right)]| = |\vec{\mu}_{12} \cdot \vec{F}|$  where  $\vec{\mu}_{12} \cong \vec{\mu}_{12}(V, I)$  is the electric dipole matrix for excitonic transition and  $\Delta\tau$  is duration of probe in our measurement. The pulse-area in our experiment can be of the order of coherence time of laser ( $\tau_c \sim \text{ns}$ ). Therefore survival of these Rabi oscillation points towards negligible<sup>174,175</sup> dephasing rate ( $\sim \frac{1}{\tau_\gamma}$ ). The spectral PhCap

response at the bias voltage of  $\text{PhCap}_{\text{max}}$  and  $\text{PhCap}_{\text{min}}$  are reported in reference 157 section VIII where two distinct energy peak of  $\sim 1.53$  eV and  $\sim 1.61$  eV are observed at bias of  $\text{PhCap}_{\text{max}}$  bias. These sharp peaks are resonant excitonic transition as expected since there is coherent resonant tunneling of electron between QD and TQW. At the bias of  $\text{PhCap}_{\text{min}}$ , a single broad peak in middle the above mentioned peak is detected at  $\sim 1.55$  eV. This broaden peak is at the condition of non-resonance and it includes the combined effect of indirect excitons around AlAs barrier in both GaAs n and p side. Quantum coherent tunneling at bias of  $\text{PhCap}_{\text{max}}$  and creation of two-component BEC can be modeled as Hadamard gate operation (reference 157 section IX). Assuming electron, due to its low effective mass, is key contributor in coherent

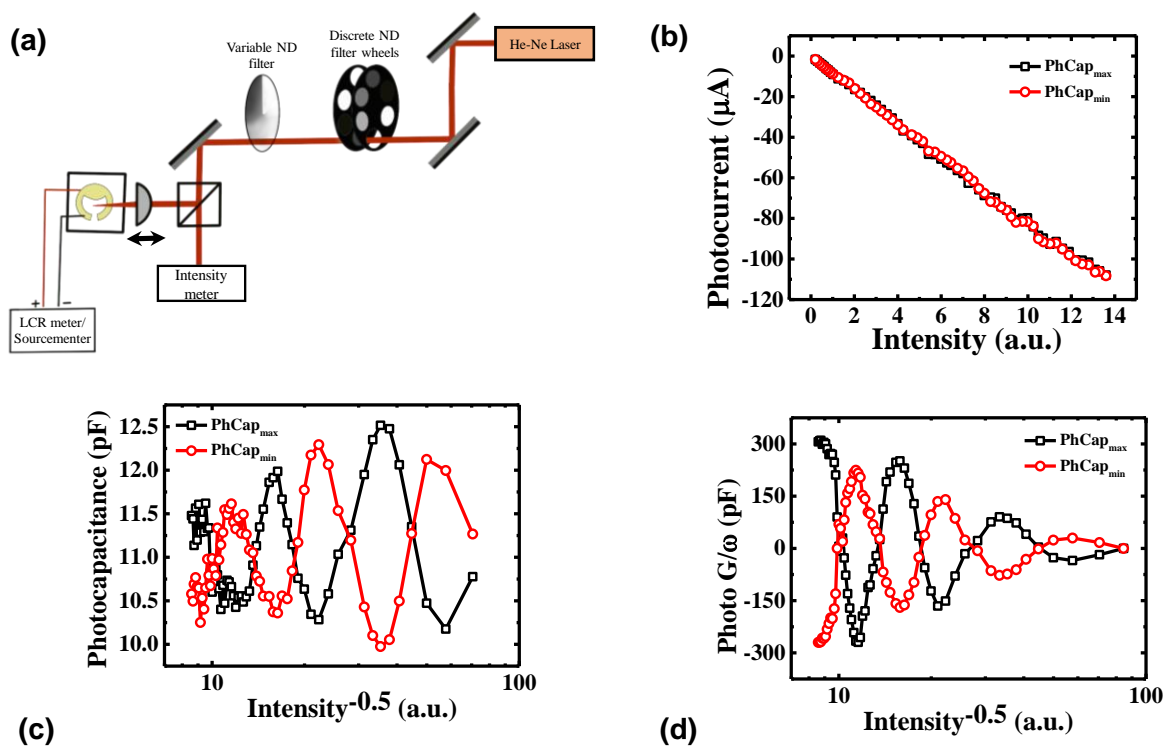


**Fig. 5.10** (a) Schematics of experimental setup. Two sets of discrete neutral density (ND) filters and one variable ND filter wheel are used to vary the intensity. (b) Photocurrent vs excitation intensity (c)  $\text{PhCap}$  vs  $(\text{Intensity})^{-0.5}$  (d)  $\text{PhG}/\omega$  vs  $(\text{Intensity})^{-0.5}$ .

tunneling and constitute two sets of excitons while being in QD and TQW. The capacitive coupling of these two excitons produces two non-degenerate entangled states of excitons. This explains the splitting at  $\text{PhCap}_{\text{max}}$  voltage. The application of bias (intensity) act as Hadamard operator and system goes into capacitive uncoupled state where QD and TQW excitons contribute independently. In conclusion, such bias controlled gate operation can be used in quantum calculations.

## 5.6 Conclusion

In conclusion, the p-i-n heterostructure, double barrier-QD system, which can generate indirect exciton of 0D-2D with direct photo-excitation, enable coherent resonant tunneling between 0D and 2D can allow a two-component excitonic BEC to sustain. The critical temperature for these BEC state in the studied sample is found to be around 100 K, below which there is a spontaneous enhancement of polarization which enhances even further when temperature is lowered. The periodic oscillation with respect to bias and photoexcitation intensity are due to the condition of coherent resonant tunneling of electron between QD and TQW, specifically, in systems where momentum conditions are imposed by direct photoexcitation and the Coulomb interaction energy for generation of indirect excitons. These conditions resulted into narrowing of momentum space, requisite for the formation of above mentioned two component BEC. The in-plane phase coherence is checked with different sets of experiments and BEC state show macroscopic phase coherent behavior of the scale of  $\sim 200$   $\mu\text{m}$ . These two component BEC show Rabi oscillation with varying photoexcitation amplitude which are only reported for single QD systems.

These optically and electrically controlled macroscopic coherent state of BEC can be utilized for those applications, specifically, requiring quantum mechanical behavior such as quantum processing and communication. The 100 K can be easily achieved by liquid nitrogen and new device can be fabricated with higher excitonic binding energy (transition metal dichalcogenides, oxides, nitrides, perovskites etc.) in the same 0D-2D design. Instead of current method of adding more qubit to a system, multiple photoexcitation can create multiple BEC states which can work as qubits. Therefore, these type of systems can bring in a paradigm shift in optoelectronics for faster and wider adaptation of quantum technologies.

As mentioned earlier, the results presented in this chapter are part of a larger study, and additional experiments which include photoluminescence and photocapacitive spectral measurements, their intensity and voltage dependence as well as detailed quantum capacitance analysis are part of other theses. With all these results, we try to argue the existence of BEC, however other possibilities cannot be denied that can explain these oscillations.

# Chapter 6

## Summary and Future direction

### 6.1 Summary and Conclusion

This thesis presented the study of two p-i-n III-V heterostructures in full device configuration and the development of a modified Michelson interferometer. New light emitting materials, their alloys, heterostructures and other molecular forms are characterized by their optical study like photoluminescence, transmission, absorption etc. However, the device level response under electrical bias and carrier injection are required to 1) understand the basic physics governing the carrier dynamics, interaction and recombination 2) provide additional manipulation through electrical parameters like applied voltage and current 3) utilize the sample for any practical application.

We studied the first sample which has  $\text{In}_{0.5}\text{Ga}_{0.5}\text{As}$  Quantum dot (QD) embedded inside  $\text{Al}_{0.3}\text{Ga}_{0.7}\text{As}/\text{GaAs}$  Quantum well (QW). This QD-QW potential configuration of heterostructure is to provide extra confinement to carriers and increase the probability of carrier capture inside QD. At low temperature and low carrier injection, we observed only QW electroluminescence (EL) with some contribution from Wetting layers (WL). When injection current is increased gradually, the QD emission rises sharply leaving QW-WL emission to saturation. These results indicated the presence of a potential barrier at the interface of QW and QD which hindered the carrier capture into QDs and only after a sufficient level of injection, the carrier could jump over the barrier and QD emission started. We argued that this potential is formed due to diffusion of electron from conduction band of GaAs to  $\text{In}_{0.5}\text{Ga}_{0.5}\text{As}$ . The knowledge of such interface barrier will benefit in fabrication of LED devices which operate under low current injection.

We further analyzed the exponentially increasing EL of QD with applied bias and compared with Shockley diode equation. An exponential empirical formula resulted where stretched exponent quantifies the contribution of the interface potential barrier. Nevertheless, rigorous experimental and theoretical studies are required to further understand the impact of this potential barrier. The study of peak energy and full width half maxima of QD indicated the presence of quantum-confined Stark effect and non-radiative Auger recombination (AR). Integrated EL of QD and QW-WL pointed towards the presence of biexcitons/trions

recombination in QD and excitonic recombination in QW-WL. Presence of trions also indicate towards the likelihood of AR.

We, then presented the study of temporal coherence on spectrally separated QD and QW-WL emission at higher current regime. With increasing carrier injection, coherence of QD emission reduced due to onset of Auger recombination because QD received higher carrier density as a result of the extra potential confinement. When temperature is increased, the coherence also increases suggesting the significant thermal escape carrier from QD to reduce the subsequent Auger recombination. Conclusively, this study reveals that heterostructure design created for additional carrier confinement also exhibit density dependent non-radiative process which negatively affects the coherence of emission. Therefore, a careful selection has to be made between degree of confinement and coherence of emission.

Basic studies of temporal coherence worked as sensitive tool to pick up the Auger recombination. Also, a lot of work is being done to exploit the quantum nature of excitonic quasi-particles in newly developed novel materials. Recently, many-body cooperative phenomena in condensed matter physics such as polariton lasing, and Bose–Einstein condensation of polaritons, excitons, and photon require the study the coherence of emitted light for rigorous experimental verifications. Therefore, we need convenient tools to measure both type of coherence. We surveyed the methods used to measure coherence and realized that two separate instruments for measurement of spatial and temporal coherence is inconvenient from the point of experimentation. Also, double slit methods offers many challenges, therefore, a single setup for dual measurement is preferred. We, tackled some of the issues with earlier methods used for dual measurement and found that coherence mixing is a problem, specially, during spatial coherence measurement mainly due to design of instrument and measuring techniques. An unwanted temporal phase adds up during spatial coherence measurement and affects the value of correlation. We adopted a method of ‘temporal filtering’ to overcome this mixing by taking a temporal coherence scan for each measurement of spatial coherence and maxima of this scan is the point where temporal phase is minimum. Thus, we developed a modified Michelson interferometer which can measure both type of coherence of a light source. Moreover, it can be used for a sample placed in compact systems like cryostats while setup is kept at room temperature. The technique of temporal filtering reduces the effect of coherence mixing one type of coherence can be studied exclusively. There this setup can help to identify the cause of individual coherence.

Apart from this, coherent systems usually undergo high coherence after some phase transition and studying the coherence during such transition can be intriguing. Therefore, we developed a method of ‘curve overlap’ where result two independent instruments, if used for coarse of fine adjustment, can be clubbed together where entire range of coarse variable can be achieved with precision of fine adjustment. We used this method for temporal delay in our setup where coarse and fine temporal delay were provided with two different instrument.

Lastly, we studied a p-i-n QD-TQW heterostructure of a single layer of InAs QD inside GaAs/AlAs barrier with impedance measurements. The selective photoexcitation from the p-side of the active layer and applied reverse bias forced the carriers to form 0D-2D spatially indirect excitons. The periodic oscillation of capacitance with applied bias indicated that these excitons go through a series of resonant conditions. A simple-minded energy level matching is insufficient; therefore, a greater analysis and experimental investigation are required. We showed two criteria for the momentum narrowing, which is required for the formation of the condensate. The photoexcitation of spatially indirect excitons and coherence resonant tunneling of electrons between QD and TQW. This momentum narrowing formed the Bose Einstein condensation of indirect excitons which also previously predicted by critical density and temperature calculations.

We then presented the experimental study showing a large spatial correlation between two photoexcited pools of BEC created by two independent sources. This spatial correlation conclusively verified the presence of a large macroscopic coherent state. The excitation intensity dependent measurement showed Rabi oscillation of large dephasing time. The advantage, we found, with such a system is the possibility of quantum processing with as many qubits as fragmented photoexcitations that can be realized as a miniaturized quantum computing device with electrical and optical manipulation.

We can summarize this thesis briefly through following points

- We learned that exclusively optical characterizations like photoluminescence are not sufficient for any light emitting sample to determine its device level performance and rather, electrical or opto-electrical studies are critical for thorough understanding in device configuration.
- Interface of two semiconductors with different bandgap produces a potential barrier effective in low injection current.

- Step-by-step extra confinement design of quantum heterostructure show density dependent Auger process which is detrimental to optical coherence.
- Instruments of coherence measurement are still need modification and improvements. Specifically, for dual coherence measurement.
- Coherence mixing can act as an offset in coherence results especially during spatial coherence and correction methods are required.
- We provided a temporal filtering method to overcome the mixing issue.
- Indirect excitons of QD-TQW can undergo a Bose-Einstein condensation (BEC) under momentum space narrowing and coherent resonant tunneling.
- The BEC condition of resonance can be manipulated optically as well electrically through external bias.
- The observed macroscopic coherence is below  $\sim 100$  K. An easily accessible temperature through liquid nitrogen.

## 6.2 Future direction

We have learned about the carrier dynamics, interaction and correlation in quantum heterostructures and developed a technique to measure both type of optical coherence. This opens up great avenues of opportunity for both, research and application based works. Some of the work is given below,

### a) Probing QD-QW heterostructure with transient spectroscopy

We investigated the temporal coherence and its relation with Auger recombination. Additionally, we need to further investigate the recombination rate of QD and QW emission through transient spectroscopy to understand the role of third excited carrier of Auger process. If the number of  $eeh$  and  $ehh$  Auger process is same, the equal number of excited electrons and holes enters the higher potential layer of QW. Their recombination with respect to injection currents will reveal about the carrier dynamics, rate of Auger with changing carrier density. The fast evolution of coherence in these transient measurement can be interesting hence we plan to make real time coherence measurement setup. This setup is elaborated in 'Instrumentation' section.

## **b) Study of optical coherence of excitons, polariton in high binding energy materials, and meta materials**

Recently some of the direct bandgap materials like Nitrides, transition metal dichalcogenide monolayers, perovskites has shown the high excitonic binding energies and excitons in these samples survive up to room temperatures. Due to their relatively low effective mass, these can make coherent condensate state. The polaritons, however require a highly quality photonic cavity, has even lower effective mass than excitons and are best candidate for room temperature quantum coherence applications. Generally coherence measurement of these systems are for verification purpose only, however, recently, in coherence measurement of polaritonic BEC, quantum vortex was reported which is expected to make a ‘quantum gyroscope’. There are many such interesting phenomena which will be intriguing to explore. With our correlation measurement setup, we can further study these systems for spatial and temporal correlation details.

## **c) Study of coherence oscillation due to optical feedback**

It has been reports that temporal coherence oscillates in LEDs due to optical feedback. This can affect the coherence of current LED devise and hamper its performance. Therefore, a detailed study of such oscillations is essential to know cause behind it to tackle the coherence variation.

## **Instrumentation:**

### **a) Quantum gate operation using 0D-2D system using photoexcitation manipulation**

Preparing an optical assembly for utilizing 0D-2D system (discussed in chapter 5) for applicable gate operation. So far, we saw the interference of two independent pools of indirect exciton BECs. We plan to demonstrate a simple gate operation using optical excitation and applied bias.

### **b) Confocal system for probing coherence of quantum structures like quantum wire and quantum dots**

The confocal system and other lithographic techniques can be used to isolate individual quantum dots and wires. The individual emission from these quantum structures can be correlated under various optical/electrical parameters. This instrument can help to study




the intra-dot correlation and can provide a deeper understanding of the carrier correlation properties.

**c) Real time analysis of coherence using state-of-art technologies**

The typical computers used in labs are sufficient for fast data transfer and processing. And, advanced CCD cameras has time temporal resolution of about  $\sim\mu\text{s}$ . With such instruments, a real time first order correlation measurement setup can be created with fast fringe analysis which can record the evolution of state of coherence. My special interest is in indirect excitons which has life time in the rage of tens of microseconds.

## References

1. Moore, G. E. Cramming more components onto integrated circuits. *Proc. IEEE* **86.1**, 82–85 (1998).
2. Lagoudakis, K. G. *et al.* Observation of half-quantum vortices in an exciton-polariton condensate. *Science* (80-. ). **326**, 974–976 (2009).
3. Kasprzak, J. *et al.* Bose-Einstein condensation of exciton polaritons. *Nature* **13**, 409–414 (2008).
4. Lagoudakis, K. G. *et al.* Quantized vortices in an exciton-polariton condensate. *Nat. Phys.* **4**, 706–710 (2008).
5. Kim, S. *et al.* Coherent polariton laser. *Phys. Rev. X* **6**, 1–9 (2016).
6. Byrnes, T., Kim, N. Y. & Yamamoto, Y. Exciton-polariton condensates. *Nat. Phys.* **10**, 803–813 (2014).
7. Roumpos, G. *et al.* Power-law decay of the spatial correlation function in exciton-polariton condensates. *Proc. Natl. Acad. Sci. U. S. A.* **109**, 6467–6472 (2012).
8. Mani, F. *et al.* Polariton condensation in a one-dimensional disordered potential. *Phys. Rev. Lett.* **106**, 1–4 (2011).
9. Roumpos, G. *et al.* Single vortex-antivortex pair in an exciton-polariton condensate. *Nat. Phys.* **7**, 129–133 (2011).
10. Singh, J. *Electronic and Optoelectronic Properties of Semiconductor Structures*. (Cambridge University Press, 2003). doi:10.1017/CBO9780511805745.

11. Grundmann Marius. *The Physics of Semiconductors*. (Springer Berlin Heidelberg, 2010). doi:10.1007/3-540-34661-9.
12. Chelikowsky, J. R. & Cohen, M. L. Nonlocal pseudopotential calculations for the electronic structure of eleven diamond and zinc-blende semiconductors. *Phys. Rev. B* **14**, 556–582 (1976).
13. Jones, E. D. Control of Semiconductor Conductivity by Doping. in *Electronic Materials* 155–171 (Springer US, 1991). doi:10.1007/978-1-4615-3818-9\_12.
14. Cheng, K. Y. *III–V Compound Semiconductors and Devices*. (Springer International Publishing, 2020). doi:10.1007/978-3-030-51903-2.
15. Cornwell, J. F. *Group theory in physics: An introduction*. (Academic press, 1997).
16. Inui, T., Tanabe, Y. & Onodera, Y. *Group theory and its applications in physics*. vol. 78 (Springer Science & Business Media, 2012).
17. Dresselhaus, M. S., Dresselhaus, G. & Jorio, A. *Group theory: application to the physics of condensed matter*. (Springer Science & Business Media, 2007).
18. Bloch, F. Uber die Quantenmechanik der Elektronen in Kristallgittern. *Zeitschrift f*  *Phys.* **52**, 555–600 (1929).
19. Yu, P. Y. & Cardona, M. *Fundamentals of Semiconductors*. (Springer Berlin Heidelberg, 2010). doi:10.1007/978-3-642-00710-1.
20. Fox Mark. *Optical Properties of Solids*. (Oxford University Press, 2001).
21. Hall, R. N. Electron-Hole Recombination in Germanium. *Phys. Rev.* **87**, 387–387 (1952).
22. Shockley, W. & Read, W. T. Statistics of the Recombinations of Holes and Electrons. *Phys. Rev.* **87**, 835–842 (1952).

23. Hader, J. *et al.* On the importance of radiative and Auger losses in GaN-based quantum wells. *Appl. Phys. Lett.* **92**, 261103 (2008).
24. Kioupakis, E., Rinke, P., Delaney, K. T. & Van de Walle, C. G. Indirect Auger recombination as a cause of efficiency droop in nitride light-emitting diodes. *Appl. Phys. Lett.* **98**, 161107 (2011).
25. Steiauf, D., Kioupakis, E. & Van de Walle, C. G. Auger Recombination in GaAs from First Principles. *ACS Photonics* **1**, 643–646 (2014).
26. Bertazzi, F., Goano, M. & Bellotti, E. A numerical study of Auger recombination in bulk InGaN. *Appl. Phys. Lett.* **97**, 231118 (2010).
27. Delaney, K. T., Rinke, P. & Van de Walle, C. G. Auger recombination rates in nitrides from first principles. *Appl. Phys. Lett.* **94**, 191109 (2009).
28. *Nitride Semiconductor Light-Emitting Diodes (LEDs)*. (Elsevier, 2018). doi:10.1016/C2016-0-01551-6.
29. Martin, A., Alibert, O., De Micheli, M. P., Ostrowsky, D. B. & Tanzilli, S. A quantum relay chip based on telecommunication integrated optics technology. *New J. Phys.* **14**, 025002 (2012).
30. Sturge, M. D. Optical Absorption of Gallium Arsenide between 0.6 and 2.75 eV. *Phys. Rev.* **127**, 768–773 (1962).
31. Bhunia, A., Singh, M. K., Galvão Gobato, Y., Henini, M. & Datta, S. Experimental evidences of quantum confined 2D indirect excitons in single barrier GaAs/AlAs/GaAs heterostructure using photocapacitance at room temperature. *J. Appl. Phys.* **123**, 044305 (2018).
32. Bhunia, A., Singh, M. K., Gobato, Y. G., Henini, M. & Datta, S. Experimental Detection and Control of Trions and Fermi-Edge Singularity in Single-Barrier GaAs/AlAs/GaAs Heterostructures Using Photocapacitance Spectroscopy. *Phys. Rev. Appl.* **10**, 044043 (2018).

33. Govind B. Nair, S. J. D. *The Fundamentals and Applications of Light-Emitting Diodes. The Fundamentals and Applications of Light-Emitting Diodes* (Elsevier, 2020). doi:10.1016/C2019-0-00273-7.
34. Matsuzaki, R. *et al.* Purely excitonic lasing in ZnO microcrystals: Temperature-induced transition between exciton-exciton and exciton-electron scattering. *Phys. Rev. B* **96**, (2017).
35. Tang, Z. K., Kawasaki, M., Ohtomo, A., Koinuma, H. & Segawa, Y. Self-assembled ZnO nano-crystals and exciton lasing at room temperature. *J. Cryst. Growth* **287**, 169–179 (2006).
36. Lai, Y. Y. *et al.* Crossover from polariton lasing to exciton lasing in a strongly coupled ZnO microcavity. *Sci. Rep.* **6**, 1–7 (2016).
37. Shih, T., Mazur, E., Richters, J. P., Gutowski, J. & Voss, T. Ultrafast exciton dynamics in ZnO: Excitonic versus electron-hole plasma lasing. *J. Appl. Phys.* **109**, (2011).
38. La Rocca, G. C. Organic photonics: Polariton lasing. *Nat. Photonics* **4**, 343–345 (2010).
39. Christopoulos, S. *et al.* Room-temperature polariton lasing in semiconductor microcavities. *Phys. Rev. Lett.* **98**, 1–4 (2007).
40. Bhattacharya, P. *et al.* Room temperature electrically injected polariton laser. *Phys. Rev. Lett.* **112**, 29–31 (2014).
41. Schneider, C. *et al.* An electrically pumped polariton laser. *Nature* **497**, 348–352 (2013).
42. Bajoni, D. *et al.* Polariton laser using single micropillar GaAs-GaAlAs semiconductor cavities. *Phys. Rev. Lett.* **100**, 1–4 (2008).
43. Kartashov, Y. V. & Skryabin, D. V. Two-Dimensional Topological Polariton Laser. *Phys. Rev. Lett.* **122**, 83902 (2019).
44. Lagoudakis, K. *The physics of exciton-polariton condensates.* (PPUR Presses

- polytechniques, 2013).
45. O'Brien, J. L. Optical Quantum Computing. *Science* (80-. ). **318**, 1567–1570 (2007).
  46. Varnava, M., Browne, D. E. & Rudolph, T. How Good Must Single Photon Sources and Detectors Be for Efficient Linear Optical Quantum Computation? *Phys. Rev. Lett.* **100**, 060502 (2008).
  47. Politi, A., Matthews, J., Thompson, M. G. & O'Brien, J. L. Integrated Quantum Photonics. *IEEE J. Sel. Top. Quantum Electron.* **15**, 1673–1684 (2009).
  48. Politi, A., Matthews, J. C. F. & O'Brien, J. L. Shor's Quantum Factoring Algorithm on a Photonic Chip. *Science* (80-. ). **325**, 1221–1221 (2009).
  49. Yang, G. *et al.* Ultrafast photophysical process of bi-exciton Auger recombination in CuInS<sub>2</sub> quantum dots studied by transient-absorption spectroscopy. *Opt. Express* **29**, 9012 (2021).
  50. Taguchi, S., Saruyama, M., Teranishi, T. & Kanemitsu, Y. Quantized Auger recombination of biexcitons in CdSe nanorods studied by time-resolved photoluminescence and transient-absorption spectroscopy. *Phys. Rev. B* **83**, 155324 (2011).
  51. Pietryga, J. M., Zhuravlev, K. K., Whitehead, M., Klimov, V. I. & Schaller, R. D. Evidence for Barrierless Auger Recombination in PbSe Nanocrystals: A Pressure-Dependent Study of Transient Optical Absorption. *Phys. Rev. Lett.* **101**, 217401 (2008).
  52. Sze, S. M. *Physics of Semiconductor Devices*. (Wiley, 2007).
  53. Fox, M. *Quantum Optics: An Introduction*. (Oxford University Press, 2006).
  54. Bach, R., Pope, D., Liou, S.-H. & Batelaan, H. Controlled double-slit electron diffraction. *New J. Phys.* **15**, 033018 (2013).
  55. Lindner, F. *et al.* Attosecond Double-Slit Experiment.

doi:10.1103/PhysRevLett.95.040401.

56. Tavabi, A. H. *et al.* The Young-Feynman controlled double-slit electron interference experiment. *Sci. Reports 2019 91* **9**, 1–8 (2019).
57. Zheludev, N. I., Prosvirnin, S. L., Papasimakis, N. & Fedotov, V. A. Lasing spaser. *Nat. Photonics* **2**, 351–354 (2008).
58. Chandrasekar, R. *et al.* Lasing Action with Gold Nanorod Hyperbolic Metamaterials. *ACS Photonics* **4**, 674–680 (2017).
59. Shadrivov, I. V., Kapitanova, P. V., Maslovski, S. I. & Kivshar, Y. S. Metamaterials Controlled with Light. *Phys. Rev. Lett.* **109**, 083902 (2012).
60. Nikitin, A., Remezani, M. & Rivas, J. G. Luminescent Metamaterials for Solid State Lighting. *ECS J. Solid State Sci. Technol.* **5**, R3164–R3169 (2016).
61. Podolskiy, V. A., Ginzburg, P., Wells, B. & Zayats, A. V. Light emission in nonlocal plasmonic metamaterials. *Faraday Discuss.* **178**, 61–70 (2015).
62. Vaskin, A., Kolkowski, R., Koenderink, A. F. & Staude, I. Light-emitting metasurfaces. *Nanophotonics* **8**, 1151–1198 (2019).
63. Le-Van, Q., Le Roux, X., Aassime, A. & Degiron, A. Electrically driven optical metamaterials. *Nat. Commun.* **7**, 12017 (2016).
64. Sudarshan, E. C. G. & Rothman, T. The two-slit interferometer reexamined. *Am. J. Phys.* **59**, 592 (1998).
65. Basano, L., Physics, P. O.-A. J. of & 2000, undefined. Interference fringes from stabilized diode lasers. *aapt.scitation.org* **68**, 245 (2000).
66. Louradour, F., Reynaud, F., Colombeau, B. & Froehly, C. Interference fringes between two separate lasers. *Am. J. Phys.* **61**, 242–245 (1993).

67. Magyar, G. & Mandel, L. Interference fringes produced by superposition of two independent maser light beams. (1963).
68. Pedrotti, F. L., Pedrotti, L. M. & Pedrotti, L. S. *Introduction to Optics*. (Cambridge University Press, 2017). doi:10.1017/9781108552493.
69. Eugene, H. *Optics*. (Addison Wesley MA, 2002).
70. Xu, N. & Li, J. Phase-shifting hiding technology for fully phase-based image using the Mach–Zehnder interferometer. *Opt. Eng.* **61**, (2022).
71. Luo, M., Chen, Y., Liu, J., Ru, S. & Gao, S. Enhancement of phase sensitivity by the additional resource in a Mach-Zehnder interferometer. *Phys. Lett. A* **424**, 127823 (2022).
72. Zhang, Q. *et al.* Full-range Fourier-domain optical coherence tomography based on Mach–Zehnder interferometer. *Opt. Lasers Eng.* **124**, 105794 (2020).
73. Menon, V. M., Deych, L. I. & Lisyansky, A. A. Nonlinear optics: Towards polaritonic logic circuits. *Nat. Photonics* **4**, 345–346 (2010).
74. D, N. D. *Optical Interferometry for Biology and Medicine*. (Springer, New York, NY, 2011).
75. Akcay, C., Parrein, P. & Rolland, J. P. Estimation of longitudinal resolution in optical coherence imaging. *Appl. Opt.* **41**, 5256 (2002).
76. Dengler, R. lab Full-field optical coherence tomography — An educational setup for an undergraduate lab. **1132**, (2020).
77. Born, M. & Wolf, E. *Principles of Optics: Electromagnetic Theory of Propagation, Interference and Diffraction of Light*. (Cambridge University Press, 2006).
78. Ryabukho, V. P., Lyakin, D. V. & Lobachev, M. I. Manifestation of longitudinal correlations in scattered coherent fields in an interference experiment. *Opt. Spectrosc. (English Transl. Opt. i Spektrosk.* **97**, 299–304 (2004).



79. Ryabukho, V. P., Lyakin, D. V. & Lobachev, M. I. The Effects of Temporal and Longitudinal Spatial Coherence in a Disbalanced-Arm Interferometer. *Tech. Phys. Lett.* **30**, 64–67 (2004).
80. Ryabukho, V. P., Lyakin, D. V. & Lychagov, V. V. What type of coherence of the optical field is observed in the Michelson interferometer. *Opt. Spectrosc. (English Transl. Opt. i Spektrosk.* **102**, 918–926 (2007).
81. Ryabukho, V. P., Lyakin, D. V. & Lychagov, V. V. Longitudinal coherence length of an optical field. *Opt. Spectrosc. (English Transl. Opt. i Spektrosk.* **107**, 282–287 (2009).
82. Ryabukho, V. P., Kal'yanov, A. L., Lyakin, D. V. & Lychagov, V. V. Influence of the frequency spectrum width on the transverse coherence of optical field. *Opt. Spectrosc. (English Transl. Opt. i Spektrosk.* **108**, 979–984 (2010).
83. Abdulhalim, I. Theory for double beam interference microscopes with coherence effects and verification using the linnik microscope. *J. Mod. Opt.* **48**, 279–302 (2001).
84. Abdulhalim, I. Competence between spatial and temporal coherence in full field optical coherence tomography and interference microscopy. *J. Opt. A Pure Appl. Opt.* **8**, 952–958 (2006).
85. Abdulhalim, I. Spatial and temporal coherence effects in interference microscopy and full-field optical coherence tomography. *Ann. Phys.* **524**, 787–804 (2012).
86. Heaney, L., Anders, J., Kaszlikowski, D. & Vedral, V. Spatial entanglement from off-diagonal long-range order in a Bose-Einstein condensate. *Phys. Rev. A* **76**, 053605 (2007).
87. Deng, Y. & Chu, D. Coherence properties of different light sources and their effect on the image sharpness and speckle of holographic displays. *Sci. Rep.* **7**, 5893 (2017).
88. Zhang, Q. *et al.* Advances in small perovskite-based lasers. *Small Methods* **1**, 1700163 (2017).

89. Stylianakis, M. M., Maksudov, T., Panagiotopoulos, A., Kakavelakis, G. & Petridis, K. Inorganic and hybrid perovskite based laser devices: a review. *Materials (Basel)*. **12**, 859 (2019).
90. Johnson, J. C. *et al.* Single gallium nitride nanowire lasers. *Nat. Mater.* 2002 *12* **1**, 106–110 (2002).
91. Huang, M. H. *et al.* Room-temperature ultraviolet nanowire nanolasers. *Science* (80-. ). **292**, 1897–1899 (2001).
92. Zavelani-Rossi, M., Lupo, M. G., Krahné, R., Manna, L. & Lanzani, G. Lasing in self-assembled microcavities of CdSe/CdS core/shell colloidal quantum rods. *Nanoscale* **2**, 931–935 (2010).
93. Demirchyan, S. S., Chestnov, I. Y., Alodjants, A. P., Glazov, M. M. & Kavokin, A. V. Qubits Based on Polariton Rabi Oscillators. *Phys. Rev. Lett.* **112**, 196403 (2014).
94. Miller, S. *Optical fiber telecommunications*. (Elsevier, 2012).
95. Gupta, S. C. *Textbook on optical fiber communication and its applications*. (PHI Learning Pvt. Ltd., 2018).
96. Ciurczak, E. W. & Igne, B. *Pharmaceutical and medical applications of near-infrared spectroscopy*. (CRC Press, 2014).
97. Ng, E. Y. K. & Etehadtavakol, M. *Application of infrared to biomedical sciences*. (Springer, 2017).
98. Diakides, M., Bronzino, J. D. & Peterson, D. R. *Medical infrared imaging: principles and practices*. (CRC press, 2012).
99. Beckman, J. E. Infrared astronomy. in *Multimessenger Astronomy* 81–115 (Springer, 2021).
100. Clements, D. L. *Infrared Astronomy—Seeing the Heat: from William Herschel to the*

*Herschel Space Observatory*. (CRC Press, 2014).

101. Budzier, H. & Gerlach, G. *Thermal infrared sensors: theory, optimisation and practice*. (John Wiley & Sons, 2011).
102. Kuenzer, C. & Dech, S. Thermal infrared remote sensing. *Remote Sens. Digit. Image Process. doi* **10**, 978–994 (2013).
103. Grundmann, M. & Bimberg, D. Gain and Threshold of Quantum Dot Lasers: Theory and Comparison to Experiments. *Jpn. J. Appl. Phys.* **36**, 4181–4187 (1997).
104. Matsuzaki, R. *et al.* Purely excitonic lasing in ZnO microcrystals: Temperature-induced transition between exciton-exciton and exciton-electron scattering. *Phys. Rev. B* **96**, (2017).
105. Mukai, K. *et al.* 1.3- $\mu\text{m}$  CW lasing characteristics of self-assembled InGaAs-GaAs quantum dots. *IEEE J. Quantum Electron.* **36**, 472–478 (2000).
106. Reithmaier, J. P. & Forchel, A. Recent advances in semiconductor quantum-dot lasers. *Comptes Rendus Phys.* **4**, 611–619 (2003).
107. Park, G., Shchekin, O. B., Huffaker, D. L. & Deppe, D. G. InGaAs quantum dot lasers with sub-milliamp thresholds and ultra-low threshold current density below room temperature. *Electron. Lett.* **36**, 1283 (2000).
108. Liu, G. T., Stintz, A., Li, H., Malloy, K. J. & Lester, L. F. Extremely low room-temperature threshold current density diode lasers using InAs dots in In<sub>0.15</sub>Ga<sub>0.85</sub>As quantum well. *Electron. Lett.* **35**, 1163 (1999).
109. Schäfer, F., Reithmaier, J. P. & Forchel, A. High-performance GaInAs/GaAs quantum-dot lasers based on a single active layer. *Appl. Phys. Lett.* **74**, 2915–2917 (1999).
110. Robinson, H. & Goldberg, B. Light-induced spectral diffusion in single self-assembled quantum dots. *Phys. Rev. B - Condens. Matter Mater. Phys.* **61**, R5086–R5089 (2000).

111. Berthelot, A. *et al.* Unconventional motional narrowing in the optical spectrum of a semiconductor quantum dot. *Nat. Phys.* **2**, 759–764 (2006).
112. Hu, X. *et al.* Photoluminescence of InAs/GaAs quantum dots under direct two-photon excitation. *Sci. Rep.* **10**, 10930 (2020).
113. Bhunia, A., Bansal, K., Henini, M., Alshammari, M. S. & Datta, S. Negative activation energy and dielectric signatures of excitons and excitonic Mott transitions in quantum confined laser structures. *J. Appl. Phys.* **120**, 144304 (2016).
114. Bansal, K. & Datta, S. Voltage modulated electro-luminescence spectroscopy to understand negative capacitance and the role of sub-bandgap states in light emitting devices. *J. Appl. Phys.* **110**, 114509 (2011).
115. Pelant, I. & Valenta, J. *Luminescence Spectroscopy of Semiconductors*. (Oxford University Press, 2012). doi:10.1093/acprof:oso/9780199588336.001.0001.
116. Popescu, D. P., Eliseev, P. G., Stintz, A. & Malloy, K. J. Temperature dependence of the photoluminescence emission from InAs quantum dots in a strained Ga<sub>0.85</sub>In<sub>0.15</sub>As quantum well. *Semicond. Sci. Technol.* **19**, 33–38 (2004).
117. Mu, X., Ding, Y. J. & Hopkinson, M. Dynamics of carriers photogenerated in a dot-in-a-well nanostructure. *Laser Phys.* **17**, 305–309 (2007).
118. Yahyaoui, M., Sellami, K., Boujdaria, K., Chamarro, M. & Testelin, C. Band parameters of InGaAs/GaAs quantum dots: electronic properties study. *Semicond. Sci. Technol.* **28**, 125018 (2013).
119. Pfeiffer, L., Schubert, E. F., West, K. W. & Magee, C. W. Si dopant migration and the AlGaAs/GaAs inverted interface. *Appl. Phys. Lett.* **58**, 2258–2260 (1991).
120. Menéndez, J., Pinczuk, A., Werder, D. J., Gossard, A. C. & English, J. H. Light scattering determination of band offsets in GaAs-Al<sub>x</sub>Ga<sub>1-x</sub>As quantum wells. *Phys. Rev. B* **33**, 8863–8866 (1986).

121. Koteles, E. S. Determining energy-band offsets in quantum wells using only spectroscopic data. *J. Appl. Phys.* **73**, 8480–8484 (1993).
122. Bimberg, D., Grundmann, M. & Ledentsov, N. N. *Quantum Dot Heterostructures*. (Wiley, 1998).
123. Chen, H.-S. *et al.* Independent variations of applied voltage and injection current for controlling the quantum-confined Stark effect in an InGaN/GaN quantum-well light-emitting diode. *Opt. Express* **22**, 8367 (2014).
124. Wang, H. *et al.* Influence of excitation power and temperature on photoluminescence in InGaN/GaN multiple quantum wells. *Opt. Express* **20**, 3932 (2012).
125. Kurzmann, A., Ludwig, A., Wieck, A. D., Lorke, A. & Geller, M. Auger Recombination in Self-Assembled Quantum Dots: Quenching and Broadening of the Charged Exciton Transition. *Nano Lett.* **16**, 3367–3372 (2016).
126. Nilsson, H. H., Zhang, J.-Z. & Galbraith, I. Homogeneous broadening in quantum dots due to Auger scattering with wetting layer carriers. in *2005 Quantum Electronics and Laser Science Conference* 504–506 (IEEE). doi:10.1109/QELS.2005.1548831.
127. Shockley, W. The Theory of *p-n* Junctions in Semiconductors and *p-n* Junction Transistors. *Bell Syst. Tech. J.* **28**, 435–489 (1949).
128. Nobrega, J. A. e *et al.* Spin polarization of carriers in resonant tunneling devices containing InAs self-assembled quantum dots. *Superlattices Microstruct.* **88**, 574–581 (2015).
129. Varshni, Y. P. Temperature dependence of the energy gap in semiconductors. *Physica* **34**, 149–154 (1967).
130. Shchekin, O. B., Park, G., Huffaker, D. L., Mo, Q. & Deppe, D. G. Low-threshold continuous-wave two-stack quantum-dot laser with reduced temperature sensitivity. *IEEE Photonics Technol. Lett.* **12**, 1120–1122 (2000).

131. Emminger, C., Abadizaman, F., Samarasingha, N. S., Tiwald, T. E. & Zollner, S. Temperature dependent dielectric function and direct bandgap of Ge. *J. Vac. Sci. Technol. B* **38**, 012202 (2020).
132. Torchynska, T. V. *et al.* Thermal activation of excitons in asymmetric InAs dots-in-a-well  $\text{In}_x\text{Ga}_{1-x}\text{As}/\text{GaAs}$  structures. *J. Appl. Phys.* **101**, 024323 (2007).
133. Maksimov, M. V. *et al.* Quantum dot injection heterolaser with ultrahigh thermal stability of the threshold current up to 50 °C. *Semiconductors* **31**, 124–126 (1997).
134. Ghosh, S. *et al.* Temperature-dependent measurement of Auger recombination in self-organized  $\text{In}_{0.4}\text{Ga}_{0.6}\text{As}/\text{GaAs}$  quantum dots. *Appl. Phys. Lett.* **79**, 722–724 (2001).
135. Narvaez, G. A., Bester, G. & Zunger, A. Carrier relaxation mechanisms in self-assembled (In,Ga) As GaAs quantum dots: Efficient P→S Auger relaxation of electrons. *Phys. Rev. B - Condens. Matter Mater. Phys.* **74**, 075403 (2006).
136. Singh, M. K. *et al.* Role of interface potential barrier, Auger recombination and temporal coherence in  $\text{In}_{0.5}\text{Ga}_{0.5}\text{As}/\text{GaAs}$  quantum dot-based p-i-n light emitting diodes. *J. Phys. D: Appl. Phys.* **52**, (2019).
137. Michelson, A. A. & Morley, E. W. On the relative motion of the Earth and the luminiferous ether. *Am. J. Sci.* **s3-34**, 333–345 (1887).
138. <https://physicsworld.com/a/double-slits-with-single-atoms/>.
139. *Holographic Interferometry*. vol. 68 (Springer Berlin Heidelberg, 1994).
140. Dionisio, R. P. Interferometry Applications in All-Optical Communications Networks. in *Interferometry Applications in All-Optical Communications Networks in Optical Interferometry* (InTech, 2017). doi:10.5772/66133.
141. Leach, R. *Optical Measurement of Surface Topography*. (Springer Berlin Heidelberg, 2011). doi:10.1007/978-3-642-12012-1.

142. Labeyrie, A., Lipson, S. G. & Nisenson, P. *An Introduction to Optical Stellar Interferometry*. (Cambridge University Press, 2006). doi:10.1017/CBO9780511617638.
143. Nolte, D. D. *Optical interferometry for biology and medicine. Optical Interferometry for Biology and Medicine* (Springer, New York, NY, 2012). doi:10.1007/978-1-4614-0890-1.
144. Imamoglu, A., Ram, R. J., Pau, S. & Yamamoto, Y. Nonequilibrium condensates and lasers without inversion: Exciton-polariton lasers. *Phys. Rev. A - At. Mol. Opt. Phys.* **53**, 4250–4253 (1996).
145. Eisenstein, J. P. & MacDonald, A. H. Bose–Einstein condensation of excitons in bilayer electron systems. *Nature* **432**, 691–694 (2004).
146. Blatt, J. M., Böer, K. W. & Brandt, W. Bose-einstein condensation of excitons. *Phys. Rev.* **126**, 1691–1692 (1962).
147. Snoke, D. W., Wolfe, J. P. & Mysyrowicz, A. Evidence for Bose-Einstein condensation of excitons in Cu<sub>2</sub>O. *Phys. Rev. B* **41**, 11171–11184 (1990).
148. Sun, Y. *et al.* Bose-Einstein Condensation of Long-Lifetime Polaritons in Thermal Equilibrium. *Phys. Rev. Lett.* **118**, 1–6 (2017).
149. Klaers, J., Schmitt, J., Vewinger, F. & Weitz, M. Bose-Einstein condensation of photons in an optical microcavity. *Nature* **468**, 545–548 (2010).
150. Kurtscheid, C. *et al.* Thermally condensing photons into a coherently split state of light. *Science* (80-. ). **366**, 894–897 (2019).
151. Ghosh, S. & Liew, T. C. H. Quantum computing with exciton-polariton condensates. *npj Quantum Inf.* **6**, 16 (2020).
152. Khanin, Y. N., Vdovin, E. E., Makarovskii, O. & Henini, M. Period of photoconductivity oscillations and charge dynamics of quantum dots in p–i–n GaAs/InAs/AlAs heterojunctions. *JETP Lett.* **102**, 720–726 (2015).

153. Khanin, Y. N. & Vdovin, E. E. Quantum Oscillations of Photoconductivity Relaxation in p-i-n GaAs/InAs/AlAs Heterodiodes. *Semiconductors* **52**, 739–744 (2018).
154. Vdovin, E. E. *et al.* Quantum oscillations in the photocurrent of GaAs/AlAs *p-i-n* diodes. *Phys. Rev. B* **89**, 205305 (2014).
155. L.L. Chang, E.E. Mendez & C. Tejedor. *Resonant Tunneling in Semiconductors*. vol. 277 (Springer US, 1991).
156. Butov, L. V., Lai, C. W., Ivanov, A. L., Gossard, A. C. & Chemla, D. S. Towards Bose–Einstein condensation of excitons in potential traps. *Nature* **417**, 47–52 (2002).
157. Bhunia, A., Singh, M. K., Huwayz, M. Al, Henini, M. & Datta, S. Experimental Control of Macroscopically Large, Schrodinger Cat like Quantum Coherent State of Bose-Einstein Condensate of Excitons as Qubits. (2021) doi:10.48550/arxiv.2107.13518.
158. Datta, S., Melloch, M. R., Bandyopadhyay, S. & Lundstrom, M. S. Proposed structure for large quantum interference effects. *Appl. Phys. Lett.* **48**, 487–489 (1986).
159. Capasso, F., Mohammed, K. & Cho, A. Resonant tunneling through double barriers, perpendicular quantum transport phenomena in superlattices, and their device applications. *IEEE J. Quantum Electron.* **22**, 1853–1869 (1986).
160. Buttiker, M. Coherent and sequential tunneling in series barriers. *IBM J. Res. Dev.* **32**, 63–75 (1988).
161. Ketterle, W. & van Druten, N. J. Bose-Einstein condensation of a finite number of particles trapped in one or three dimensions. *Phys. Rev. A* **54**, 656–660 (1996).
162. Fisher, D. S. & Hohenberg, P. C. Dilute Bose gas in two dimensions. *Phys. Rev. B* **37**, 4936–4943 (1988).
163. Combescot, M., Betbeder-Matibet, O. & Combescot, R. Bose-Einstein Condensation in Semiconductors: The Key Role of Dark Excitons. *Phys. Rev. Lett.* **99**, 176403 (2007).



164. Penrose, O. & Onsager, L. Bose-Einstein Condensation and Liquid Helium. *Phys. Rev.* **104**, 576–584 (1956).
165. Yukalov, V. I. Basics of Bose-Einstein condensation. *Phys. Part. Nucl.* **42**, 460–513 (2011).
166. Zrenner, A. *et al.* Coherent properties of a two-level system based on a quantum-dot photodiode. *Nature* **418**, 612–614 (2002).
167. Li, X. *et al.* An All-Optical Quantum Gate in a Semiconductor Quantum Dot. *Science* (80-. ). **301**, 809–811 (2003).
168. Bonadeo, N. H. *et al.* Coherent Optical Control of the Quantum State of a Single Quantum Dot. *Science* (80-. ). **282**, 1473–1476 (1998).
169. Stievater, T. H. *et al.* Rabi Oscillations of Excitons in Single Quantum Dots. *Phys. Rev. Lett.* **87**, 133603 (2001).
170. Kamada, H., Gotoh, H., Temmyo, J., Takagahara, T. & Ando, H. Exciton Rabi Oscillation in a Single Quantum Dot. *Phys. Rev. Lett.* **87**, 246401 (2001).
171. Andrews, M. R. *et al.* Observation of Interference Between Two Bose Condensates. *Science* (80-. ). **275**, 637–641 (1997).
172. Lin, Y. *et al.* Dissipative production of a maximally entangled steady state of two quantum bits. *Nature* **504**, 415–418 (2013).
173. Wang, Z., Wu, W. & Wang, J. Steady-state entanglement and coherence of two coupled qubits in equilibrium and nonequilibrium environments. *Phys. Rev. A* **99**, 042320 (2019).
174. Cirac, J. I. & Zoller, P. Quantum Computations with Cold Trapped Ions. *Phys. Rev. Lett.* **74**, 4091–4094 (1995).
175. Cirac, J. I., Lewenstein, M., Mølmer, K. & Zoller, P. Quantum superposition states of

Bose-Einstein condensates. *Phys. Rev. A* **57**, 1208–1218 (1998).